6-9-92
E 6970

NASA Technical Memorandum 105628

Composites of Low-Density Trialuminides: Particulate and Long Fiber Reinforcements

K.S. Kumar, M.S. DiPietro, and S.A. Brown
Martin Marietta Laboratories
Baltimore, Maryland

and

J.D. Whittenberger
Lewis Research Center
Cleveland, Ohio

April 1992

NASA

CONTENTS

COMPOSITES OF LOW-DENSITY TRIALUMINIDES: PARTICULATE AND LONG FIBER REINFORCEMENTS

K.S. Kumar, M.S. DiPietro, and S.A. Brown
Martin Marietta Laboratories
Baltimore, Maryland 21227

and

J.D. Whittenberger
National Aeronautics and Space Administration
Lewis Research Center
Cleveland, Ohio 44135

ABSTRACT

An examination of the ternary $L1_2$ trialuminides, $Al_{66}Ti_{25}Mn_9$, $Al_{67}Ti_{25}Cr_8$ and $Al_{22}Ti_8Fe_3$ in compression, bending and tension revealed that none of these compounds exhibited a desirable balance of strength, ductility and oxidation resistance. Thus, quaternary and quinary solid solutions of these ternary compounds may provide an optimal combination of these properties. Preliminary studies indicated that these three ternary compounds were mutually soluble in each other and further, a hardness mnimum was observed in the as-cast quaternary alloy $Al_{66}Ti_{25}Mn_{6.75}Fe_{2.25}$. Diffusion couples were also examined in the system $Al_{66}Ti_{25}Mn_9$ - $Al_{67}Ti_{25}Cr_8$ in the temperature range 1073K - 1373K and these confirmed the presence of a continuous solid solution in this system. Interdiffusion coefficient, D and activation energy, Q were obtained for various intermediate compositions.

Subsequently, specific quaternary and quinary compositions were cast, homogenized and isothermally forged. Particulate-reinforced (20 vol.% TiB_2) composites using these compositions as matrices were also produced via the XD™ process, pulverized to predetermined size distribution of powders, hot-pressed and isothermally forged to full density. Both, the monolithic material and its particulate-reinforced counterparts were examined in compression as a function of temperature and at high temperatures, as a function of strain rate. Three-point bend tests were conducted on the powder-metallurgy (P/M) processed composites to determine the ductile-to-brittle transition temperature. Likewise, bend tests were also conducted on the forged, ingot-metallurgy (I/M)

processed monolithic material at 300K - 873K. Some tensile tests were undertaken; however the results were generally disappointing, and frequently measurable ductility was observed only above 773K. The microstructure of the as-forged material was characterized by optical and transmission electron microscopy techniques and the bends and tensile fracture surfaces were exmined in a scanning electron microscope (SEM). Heat-treatment studies were undertaken on the Al-Ti-Cr-Mn quaternary composition and an Al-Ti-Fe-Cr-Mn quinary composition to obtain an appreciation for grain-growth behavior. Such heat-treated materials were examined in compression as a function of temperature and, in three-point bending at 300K and 473K and compared against their as-forged counterparts. Likewise, bend tests were conducted at 473K on the ternary $Al_{66}Ti_{25}Cr_9$ that was heat-treated to obtain various grain sizes to examine the role of grain size on plasticity and fracture stress.

An alternate approach that was examined in this program to enhance the low temperature damage tolerance of these materials (and possibly improve creep resistance simultaneously) was to incorporate long refractory metal wires (e.g. W, Nb, Ta, TZM, Ti, Fe and stainless steel) in the matrix. The matrix in this instance could be the monolithic material or its particulate-reinforced counterpart. Critical requirements include chemical compatibility and minimal thermal expansion coefficient (CTE) mismatch. Feasibility studies (single wire in a matrix) undertaken to identify a successful matrix-refractory wire combination indicated that only W wires survived after hot consolidation with no interfacial reactions and/or matrix cracking. Subsequent studies however indicated that upon increasing the number of wires to incorporate the influence of constraint stresses from adjacent wires, the matrix exhibited cracking as would be expected from the large CTE mismatch between W and these trialuminides. Up to 20 vol.% TiB_2 particles do not significantly reduce the CTE of the matrix. Thus, to date, a successful matrix-refractory metal wire combination has not been identified.

In summary, it appears that of the various matrix compositions examined, ternary $Al_{66}Ti_{25}Mn_9$ exhibits the best balance in strength, ductility and oxidation resistance. The addition of TiB_2 particulates provides limited benefits, if any. They dramatically improve strength at low temperatures, although there is no clear benefit in strength at the projected use temperatures. The addition of these particulates causes a significant loss in ductility and may even cause a deterioration in oxidation resistance (remains to be verified). The loss in ductillity may arise due to a very fine grain size, boron in solid solution and the particles themselves acting as fracture initiation sites. The refinement in grain size is also likely responsible for the observed loss in high temperature strength. Although the idea of refractory metal wire reinforcement is an attractive one, a successful combination remains to be identified and possible approaches include the incorporation of a reaction barrier coating and compliant layers for accomodating CTE mismatch stresses.

I. INTRODUCTION

The continually growing demand for lightweight, high-temperature materials for structural applications in the hypersonic transportation arena has led to a focus on such refractory materials as ordered intermetallics, ceramics, and composites thereof. Typical applications include the nose cone and leading edges of wing structures, engine components such as turbine blades, combustor and nozzle sections, and missile fins.

Ordered intermetallics are attractive high-temperature materials based on their melting point and the limited diffusion that is a consequence of the ordered structure. They have advantages over ceramics in that they are electrically conducting (and can thus be machined into shapes by techniques such as electrodischarge machining), are likely to be more amenable to conventional joining techniques, and can be nondestructively evaluated by techniques used for metals. However, they suffer from several drawbacks: they are frequently brittle at low temperatures, have little damage tolerance, are not always as creep resistant as expected, and are often susceptible to environmental embrittlement. Attempts to improve the ambient temperature damage tolerance of brittle materials (e.g., ceramics) have usually involved the incorporation of another brittle or ductile second phase in the form of particulates, whiskers or long fibers. Such reinforcements are frequently expected to produce enhanced creep resistance also in the resulting composites. Alternately, metallurgical concepts such as transformation-induced plasticity which enhance ambient temperature toughness in such materials, have also been tried. All these approaches have also been examined for intermetallic materials, although with not as much success as in ceramic matrix composites.

A key element in designing an intermetallic matrix composite for a particular application is tailoring the reinforcement and matrix to achieve both, chemical compatibility and an acceptable coefficient of thermal expansion (CTE) mismatch. These issues are critical in the case of high-temperature materials because, at the projected use temperatures, the kinetics of possible reactions are extremely fast and can lead to severe reinforcement degradation. Similarly, the temperature range over which the materials are likely to be cycled is so large that differences in the thermal expansion coefficient between the reinforcement and matrix can lead to very large stresses, which often cause cracking.

Thus, to obtain a desirable working system that meets the goals of the intended applications, it is necessary to optimize the matrix behavior, select the appropriate reinforcement, and then optimize the composite response. Intermetallics at the aluminum-rich end of phase diagrams, which are attractive as candidate matrix materials because of their potentially low density, reasonably high melting point, and good oxidation resistance, are extremely brittle at ambient temperatures. The reason for this lack of ductility may be that these intermetallics have complex crystal structures with large Burger's vectors; therefore, they do not have sufficient operative slip systems and frequently deform by twinning.

The recent discovery of ternary $L1_2$ trialuminides, obtained by alloying binary Al_3Ti with ~9 at.% of a ternary element such as Cu, Ni, Fe, Cr or Mn, created a lot of excitement in the research community because they were expected to have sufficient slip systems to confer the much-needed ambient ductility. Over the past two years, under the auspices of two NRA HITEMP programs, we have shown that while some of these compounds display significant compressive ductility, only the Mn-based ternary compound exhibits any sign of tensile ductility at room temperature -- and that in a limited amount. Possible reasons for the lack of tensile ductility are 1) an intrinsically low cleavage strength, 2) a very small critical flaw size, and/or 3) an inability to transfer dislocations effectively from one grain to an adjacent one.

In the first year, we used XD™ Technology to reinforce the $L1_2$ intermetallics $Al_{22}Fe_3Ti_8$, $Al_{66}Mn_9Ti_{25}$, and $Al_{67}Cr_8Ti_{25}$ (tau) with TiB_2 particulates, and conducted a 1-year feasibility effort to identify the range of use temperatures for various reinforcement volume fractions. Particulate (TiB_2) reinforcement significantly enhances the room-temperature strength of these $L1_2$ trialuminides and this strength enhancement is retained up to ~1000K. At higher temperatures, a loss in strength occurs and the particulate composite is weaker than its monolithic counterpart at conventional strain rates (~$10^{-4}s^{-1}$), although at slow strain rates (~$10^{-7}s^{-1}$), the trends are reversed and the composite exhibits marginal superiority. Clearly, a fine distribution of up to 20 vol.% of a discontinuous reinforcement alone is insufficient to provide the desired high-temperature properties.

In the second year, in an attempt to obtain a balance of strength and ductility, and to a lesser extent, oxidation resistance, solid solutions of these ternary $L1_2$

compounds were examined as matrix material. Particulate reinforcement in these matrices were incorporated using the XD™ process. Further, continuous metal wires were also examined as potential reinforcements because 1) they are more readily available and more economical than ceramic fibers and 2) they may, in this particular matrix (300K-1300K) serve the dual purpose of providing low-temperature damage tolerance and high-temperature strength. The disadvantage is that they are likely to be more reactive than ceramic reinforcements and also exhibit a significant mismatch in CTE with respect to the matrix. The results of the second-year effort are discussed in this report and future directions are recommended.

II. LITERATURE REVIEW

A. $L1_2$ TRIALUMINIDES

The $L1_2$ trialuminides based on Al_3Ti and obtained by selectively alloying with Fe, Cr or Mn have been of recent research interest. Progress to date in this field was recently reviewed by George et al (1). Experimental and theoretical work to date have been reviewed and various possible reasons for the brittleness of these alloys are discussed. Other topics covered in this review include alloying element effects on phase stability, dislocation structures, mechanical properties, cleavage fracture behavior, and first-principle calculations of elastic constants, fault energies, and ideal cleavage strengths.

Compression studies (2) on these materials revealed that the compound $Al_{22}Ti_8Fe_3$ is stronger than either the Cr- or Mn- based counterparts. For similar grain sizes, $Al_{67}Ti_{25}Cr_8$ and $Al_{66}Ti_{25}Mn_9$ exhibited similar strength levels in the temperature range 77K - 1273K, although at slow strain rates at elevated temperatures, the Cr-based compound exhibited marginal strength superiority over $Al_{66}Ti_{25}Mn_9$. Three-point bend tests (2) and limited uniaxial tensile tests (3) revealed limited ambient ductility at room temperature for $Al_{66}Ti_{25}Mn_9$, whereas tensile ductility was observed for $Al_{67}Ti_{25}Cr_8$ only at 623K (2, 4). Although tensile tests were not conducted on the Fe-based $L1_2$ compound, three-point bend tests revealed a ductile to brittle transition temperature (DBTT) of ~973K (2). A limited number of oxidation studies have also been performed on the $L1_2$ trialuminides (5, 6) and results from these studies reveal that the isothermal oxidation response of these compounds in general is superior to that of binary TiAl; however, the nature of the third element in the ternary $L1_2$ compounds appears to influence the oxidation response to some degree (5). Cyclic oxidation studies (6) at 1473K revealed the Cr-based compound to be superior to the Mn-containing counterpart although at lower temperatures, the difference is less dramatic. It is pertinent to recognize that at least in the monolithic form, these compounds are unlikely to be considered for use above 1200K. From these studies, it becomes apparent that to obtain a balance of strength and ductility, and to a lesser extent, oxidation resistance, it is necessary to examine solid solutions of these ternary compounds. Other systems (e.g. FeAl, CoAl, NiAl) have been examined (7) with similar intents and unexpected high temperature strength maxima were recorded. Since scientific guidelines are not currently available to predict such properties, most alloying studies to date have relied on trial and error approaches.

Limited studies have been performed to characterize the dislocations and faults in these ternary compounds. Intrinsic stacking faults on {001} planes have been reported in the $L1_2$ compound $Al_{67}Ni_8Ti_{25}$, resulting from the dissociation of <001> {001} dislocations (8). The authors claim that these faults do not participate directly in the deformation processes (8). Turner et al. (9) reported compressive plastic deformation in polycrystalline $Al_{67}Ni_8Ti_{25}$ due to <110> {111} slip. They indicated that these dislocations were not dissociated by more than 2 nm. The observed brittle failure in tension at room temperature was attributed to an activation barrier for dislocation emission from crack tips. Vasudevan et al., (10) examining the dislocation structures in $Al_{67}Ni_8Ti_{25}$ after compressive deformation at 573K and 873K, found that a major fraction of the <110> dislocations on the {111} planes existed as dipoles. These were speculated to cause rapid work hardening (11), thus accounting for limited ductility and brittle failure. After the deformation at 573K, Vasudevan et al. discerned no dissociation of the dipole dislocations into 1/2<110> pairs, although a few <110> dislocations lying on the {001} planes dissociated into superpartial pairs. After the deformation at 873K, the dislocation structure was essentially the same, except that the density of dissociated <110> dislocations on {001} planes was higher. Many of the <110> dislocations on the {111} planes were still present as dipoles.

Single-crystal studies on the Fe-based compound (12) suggest a temperature dependence of yield strength similar to that for the Pt_3Al-type alloy, whereas the operating slip systems in the alloy vary with orientation and temperature, similar to the Ni_3Al-type alloys. This combination of behaviors has not been previously reported for an $L1_2$ material. For example, in an early study of polycrystalline $Al_{22}Ti_8Fe_3$, the temperature-strength profile was reported to be similar to that for Co_3Ti, rather than Ni_3Al or Pt_3Al, which would reflect a Pt_3Al-type behavior at low temperatures and an Ni_3Al-type behavior at the higher temperatures (13). Such a response implies a material where superdislocations are separated by superlattice intrinsic stacking faults (SISF) at low temperatures to provide the non-planar core structure, and separated by antiphase boundaries (APB) at high temperatures to provide the positive temperature dependence of strength. Inui et al. (14) have shown that this is in fact the case; specifically, in specimens deformed at room temperature, a/3 <112> superpartials were separated by SISF on {111} planes, whereas in specimens deformed at 873K, dislocations dissociated into a/2 <110> superpartials separated by APB on the {001} planes. More recently, Hu Gengxiang et al. (15) examined room-temperature deformation characteristics of $Al_{66}Ti_{24}Fe_9$ and essentially confirmed the dislocation separation scheme proposed by Inui et al. (14). Liu et al. (16,17) reported similar dislocation characteristics in $(Co,Ni)_3Ti$ deformed at room temperature and 873K. Recently, Liu et al. (18) used in-situ straining experiments to show that such a transition can occur for Co_3Ti at room temperature under an applied stress: an external stress caused superpartials separated by SISF to transition to a situation where they were separated by an APB; upon removal of the stress, they reverted to SISF separation.

The nature of dislocation dissociation in $L1_2$ Al_3Ti doped with Fe and deformed at room temperature is, however, controversial at present. Specifically, while the results of Inui et al. (14) and of Hu Gengxiang et al (15) indicate the presence of a/3 <112> superpartials separated by SISF on {111} planes, Morris and Lerf (19,20) contend that after 1% plastic deformation in compression at room temperature, the <110> superdislocations are undissociated, being mobile on {111} planes. At higher strains however (~4%), several of the superdislocations appeared dissociated, with a burger's vector of 1/2 <110>, being separated by an APB on the {111} plane. Likewise, in an earlier study, George et al (21) reported APB separation of superpartial dislocations in a specimen of $Al_{22}Ti_8Fe_3$ doped with vanadium and compression tested at room temperature.

While these $L1_2$ trialuminides are frequently viewed as a family of materials with similar characteristics, it is important to recognize that there are significant differences in their phsical properties such as shear and bulk modulii, poisson's ratio (1, 22) and in the variation in electrical resistivity with temperature (23). Thus caution must be exercised in inferring the deformation characteristics of one $L1_2$ trialuminide (e.g. $Al_{66}Ti_{25}Mn_9$) based on the observations of another (e.g. $Al_{22}Ti_8Fe_3$); moreover, even for one particular compound, it would not be unreasonable to expect deformation characteristics to vary with alloy composition within the single-phase field. An indirect evidence of this feature was recently reported by Lerf and Morris (24) where they reported a change in APB energy in $Al_{22}Ti_8Fe_3$ and argued it to be likely a consequence of precipitation during deformation and hence a change in matrix composition.

All these compounds exhibit serrated flow in the intermediate-temperature regime (~650K - 950K) in compression, in bend, and in tension when plasticity is sufficient. The occurance of these serrations is accompanied by audible clicks and the amplitude of these serrations is frequently as large as 20 MPa in the 1-2% plastic strain regime. The origin of the serrated flow in these compounds is unknown, but it could arise from interstitials or, alternately, from the presence of the third element (substitutional), which must necessarily occupy one or both sublattice sites (25,26). Local clustering or even redistribution of the three atomic species at the dislocation cores may then be responsible for the serrated flow. The influence of serrated flow on intermediate-temperature mechanical properties, particularly ductility, remains to be determined. Lerf and Morris (24) argue that these serrations may be a consequence of thermally activated dissociation of <110> dislocations into superpartials which have a higher intrinsic mobility than the undissociated dislocations at lower temperatures and therefore produce a rapid strain increment before encountering obstacles and coming to a halt. The validity of this argument remains open to debate for $Al_{66}Ti_{25}Mn_9$ and $Al_{67}Ti_{25}Cr_8$ since superdislocation dissociation has been reported even at 298K and yet serrations are only observed at intermediate temperatures.

Finally, George and Liu (27) reviewed the failure mode in these trialuminides. In spite of being soft, these compounds cleaved in an extremely brittle manner. All the commonly cited reasons for the brittleness of metals were ruled out and, by elimination, it was deduced that their brittleness was due to intrinsically poor cleavage strength. Consistent with this conclusion, first-principles quantum mechanical calculations (28) show that the cleavage strength of trialuminides is, in fact, significantly lower than that of a ductile $L1_2$ material like Ni_3Al.

B. PARTICULATE-REINFORCED INTERMETALLIC MATRIX COMPOSITES

Reinforcements in materials can be either continuous or discontinuous. Continuous reinforcements are typically fibers and occasionally laminates. Discontinuous reinforcements include particulates, short fibers, and whiskers. Discontinuous reinforcements are advantageous in that the composites are relatively easy to fabricate by P/M and I/M techniques and the resulting products exhibit isotropic behavior unless special efforts are made to align the reinforcement. Continuous reinforcement composites are more difficult to fabricate and exhibit anisotropic behavior; however, it is possible to obtain quasitropic materials by orientation of the various laminates in predetermined directions. Continuous reinforcements are usually more effective for reducing creep, as well as for enhancing ambient toughness, but the relative advantages of the two types of reinforcements are system and application dependent.

In intermetallic matrix composites, another major consideration is the mismatch in coefficient of thermal expansion (CTE) between the matrix and the reinforcing phase. Since these matrices are typically brittle, their ability to withstand the stresses generated during thermal cycling from CTE mismatch is not very high. In continuously reinforced composites, these stresses can lead to macroscopic cracking; in particulate composites, this may be less of a problem.

Reinforcements in intermetallics have been used for creep resistance improvement and/or ambient toughness enhancement. Although intermetallics are reported to be strong at high temperatures, this is not often the case (e.g., NiAl), particularly at slow strain rates that are representative of creep conditions. In such instances, reinforcing the intermetallic may enhance its high-temperature performance. Alternately, continuous and discontinuous ductile reinforcements have been used to enhance the toughness of intermetallics at low temperatures (300K). However, interfacial reactions during thermal cycling lead to the formation of brittle intermetallics at the interface, causing the crack to propagate along the interface rather than allowing it to be blunted by the reinforcing phase. Another approach that has been used to enhance toughness (and deter macroscopic failure) is reinforcing the intermetallic matrix with discontinuous fibers or continuous fibers that form "weak bonds" at the interface, leading to fiber pull-out during failure. Clearly, the selection of a matrix-reinforcement combination is dependent on the end use, because the characteristics required for enhancing creep resistance are not necessarily the same as those needed to improve toughness. In either event, matrix-reinforcement reactions, the thermal and metallurgical stability of the reinforcement, and the CTE mismatch must all be considered.

Several approaches have been documented to date to produce discontinuously reinforced intermetallic matrix composites. These range from traditional methods such as melt spinning (29) and mechanical alloying (30) to more novel techniques such as reaction sintering (31) and XD™ synthesis (32). In the latter two processes, the exothermic reaction that accompanies the formation of an intermetallic compound is used to produce the composite. Since the focus of our research was particulate composites produced via the XD™ process, we present here recent results on $L1_2$-trialuminides-based intermetallic composites produced by this approach. The XD™ process can be used to produce a P/M product or an I/M product. The I/M route limits the reinforcement volume fraction to <10% due to melt viscosity problems, but the P/M process places no such limitation. However, P/M incorporates higher levels of impurities, such as oxides, compared to the casting route. Two reviews, one on discontinuously reinforced intermetallic composites (33) and the second, on such composites produced specifically by the XD™ process (34) were recently published and essentially summarize the status to date in the field.

The role of TiB_2 particulate reinforcement in such $L1_2$ trialuminides in affecting the compressive strength as a function of temperature and as a function of strain rate at high temperature was recently examined (35). An alloy of composition Al-27.0 at.%Ti - 8.75 at.%Fe was shown to consist substantially of the $L1_2$ phase $Al_{22}Fe_3Ti_8$ and small amounts of a second phase which precipitated on the cube planes of the $L1_2$ phase. This material was produced in the monolithic form and with 20 vol.% TiB_2 by the XD™ process. The variation in compressive yield strength of these two materials as a function of test temperature revealed that the particulates significantly enhanced room- and warm-temperature strength but did not improve high-temperature strength or extend the useful range of the monolithic material. In fact, above ~1000K, the composite was weaker than the monolithic material. The drop in strength observed in both materials between 900-1100K was attributed to the dissolution of the second phase.

The effects of strain rate on the flow stress of the monolithic material and the particulate composites in the temperature range 1000K-1200K were examined. A very interesting observation is that the composites are weaker than the monolithic material at fast strain rates at both 1100K and 1200K, but are stronger at slow strain rates. This observed "dispersion-weakening" effect was previously reported (36) in a composite system of Zn containing 5 to 30 vol.% of <1 mm Al_2O_3 or W particles. They postulated that above a certain threshold stress, macroscopic flow stress is dominated by mobile dislocations, which are generated at particle-matrix interfaces by local stresses arising from incompatibilities between the matrix and the reinforcements. A similar argument is used to explain the present observations. In addition, the reversal in behavior at the slower strain rates is argued on the basis that the strength level is low and the threshold stress is not reached; thus, the composite is stronger.

Likewise, the effect of TiB_2 particulate reinforcement on compressive yield stress at various temperatures of $Al_{66}Ti_{25}Mn_9$ and $Al_{67}Ti_{25}Cr_8$ was examined. Below 900K, the composite materials are much stronger than the monolithic materials (Fig. 1a). The high yield strength observed for the powder metallurgy-processed monolithic material relative to its ingot metallurgy counterpart (Fig. 1b) can be fully explained on the basis of grain refinement. This explanation was confirmed by producing a P/M monolithic material with a grain size similar to its I/M counterpart; the strength of the two products were comparable (Fig. 1b). For the high strength, P/M monolithic material, strength is temperature insensitive in the range 400K-1000K. Beyond 1000K, strength decreases with increasing temperature, reaching 32 MPa at 1273K. The composites, unlike the monolithic materials, exhibit a mild positive temperature dependence between 400K and 700K, which is believed to be due to second-phase precipitation from a supersaturated matrix. (The supersaturation of the matrix in the hot-pressed material is believed to be a consequence of fairly rapid cooling over the intermediate temperature range (~700K) at the end of the hot-pressing cycle). Above 700K, a drop in strength is observed and is associated with the dissolution of the second phase. At even higher temperatures (>1000K), the composite is weaker than the monolithic material for reasons similar to those previously discussed for the Fe-based $L1_2$ trialuminide system.

Thus, for the various systems examined to date, particulate reinforcement appears to impart little or no high-temperature strength advantage over the monolithic materials. Further, low-temperature ductility is adversely affected by the very high ambient temperature strength obtained in these composites. Alternate approaches to increase damage tolerance at low temperatures and creep resistance at high temperatures are deemed necessary.

III. EXPERIMENTAL TASKS

TASK I - Preliminary evaluation of quaternary Tau-based solid solution alloys.

1. Ingot metallurgy shall be used for the production of small quantities (~25 g) of Tau-based intermetallics; a total of 9 different compositions shall be fabricated with 3 alloys each from the Al-Ti-Fe-Mn, Al-Ti-Fe-Cr and Al-Ti-Cr-Mn systems in the following ratios:

   (a) $Al_{66}Ti_{25}(X_{0.25}Y_{0.75})_9$
   (b) $Al_{66}Ti_{25}(X_{0.50}Y_{0.50})_9$
   (c) $Al_{66}Ti_{25}(X_{0.75}Y_{0.25})_9$

2. The 9 compositions shall be homogenized by annealing at high temperature. After cooling the microstructure shall be metallurgically characterized by X-ray diffraction, optical microscopy, scanning electron microscopy in combination with energy dispersive x-ray analysis and differential thermal analysis.

3. One composition from each of the three quaternary systems shall be chosen for further study with the basis of selection being made on melting point, the absence of deleterious second phases, a mainly (or totally) cubic crystal structure matrix, and minimum in hardness, if one exists.

TASK II - Production of tau-based materials by the ingot metallurgy process.

1. Ingot metallurgy shall be used for the production of approximately 2.5 kg heats of each of five Tau-based intermetallics of the following compositions:

   (a) One from each of the three quaternary systems per Task I (3) .
   (b) $Al_{67}Ti_{25}Cr_8$
   (c) $Al_{66}Ti_{25}Mn_9$

2. Each of the above five ingots shall be homogenized and isothermally forged into pancakes.

TASK III - Production of materials by the powder metallurgy XD™ process.

1. Powder metallurgy XD™ synthesis shall be used for the production of Tau-based intermetallics composites; a total of 5 different powder compositions shall be fabricated as follows:

    (a) Same matrix compositions as Task II(1) where each matrix contains 20 vol. pct. TiB_2 particles.
    (b) $Al_{67}Ti_{25}Cr_8$ + 20 vol. pct. TiB_2 particles.
    (c) $Al_{66}Ti_{25}Mn_9$ + 20 vol. pct. TiB_2 particles.

TASK IV - Heat treament studies.

1. As forged Tau-based alloys from Task II shall be subjected to a series of heat treatments to determine grain growth, second phase formation and morphology, etc. to determine the range of microstructures available in each system. The response of the 5 alloys from Task II shall be examined.

TASK V - Long fiber composite study and fabrication.

1. Submit at least 500 g of at least 3 different Tau-based alloy powders to the Lewis Research Center for the fabrication of long fiber composites containing fibers of different composition.

2. The Lewis Research Center will produce Tau-based composites containing fibers of different composition from each of the powders supplied under Task V (1) and will conduct various experiments (compatibility as a function of heat treatment, thermal coefficient of expansion, etc.) to determine the most suitable combination

3. The Lewis Research Center shall choose the most favorable matrix-fiber combination and will produce several composite plates containing a fixed volume fraction of the fiber with

   (a) Pure Tau-based matrix(s),
   (b) Same Tau-based matrix(s) as Task V (3) + 20 vol. pct. TiB_2 particles.

4. Attempts shall be under taken by the contractor to produce composite plates similar to those of Task V (3) utilizing the contractor's in house hot pressing facility in combination with graphite and/or alumina tooling.

TASK VI - Mechanical property testing.

1. The following mechanical property testing shall be undertaken on the 5 alloys from Task II and five particulate reinforced composites from Task III:

   (a) Compressive yield strength as function of temperature between room temperature and 1200K.
   (b) Three point bend testing as a function of temperature between room temperature and 900K.
   (c) Tensile testing as a function of temperature between room temperature and 1200K.
   (d) Ambient temperature short-rod fracture toughness testing.

   In addition compressive strength of these Tau-based materials as functions of temperature and strain rate between 900 and 1100K will be determined at the Lewis Research Center.

2. The following Mechanical property testing shall be undertaken on long fiber composites from Tasks V(3) and V(4) where possible.

   (a) Three point bend testing as a function of temperature between room temperature and 900K on specimens taken parallel and normal to the fiber axis.

(b) Tensile testing as a function of temperature between room temperature and 1200K on specimens taken parallel and normal to the fiber axis.

(c) Ambient temperature fracture toughness testing on specimens taken parallel, normal and at 45 degrees to the fiber axis.

IV. EXPERIMENTAL PROCEDURE

A. MATERIAL PREPARATION

Discontinuously reinforced composites of ternary and quaternary $L1_2$ trialuminides containing 20 vol. % TiB_2 particulates ≤ 1 μm in size, were produced by the P/M-XD™ process to overcome the high melt viscosity problems that prohibit the use of conventional casting processes. The monolithic forms were processed by ingot metallurgy.

1. I/M Approach

Preliminary studies were undertaken to evaluate the feasibility of producing single phase, solid solution, quaternary $L1_2$ compounds. For this, small ingots (~50g) were cast in alumina crucibles in an induction furnace and allowed to solidify in the crucible. These ingots were then homogenized in flowing argon and then characterized. Subsequently, two-kilogram ingots of select quaternary compositions were prepared by induction melting high-purity binary master alloys under an argon atmosphere. The alloys were melted in zirconia crucibles and poured into graphite molds. Cylinders (60 mm in diameter x 64 mm high) were electrodischarge-machined from the as-cast materials and were homogenized in slowly flowing argon first at 1323K for a day, followed by 4 days at 1473K. The homogenized material was examined optically to ensure a substantially single-phase microstructure. The cylindrical sections were isothermally forged to approximately 18-mm-thick "pancakes" at Pratt & Whitney in Florida. Wet chemical analysis was performed on these castings and C,N,O, and H levels in the alloys were also measured.

2. P/M Approach

In the previous program (37) elemental powders in the -150 μm to +44 μm size range were blended to obtain the ternary and quaternary compositions. Excess Ti and submicron boron powders were added to obtain composites containing 5, 10, and 20 vol.% TiB_2 particulates. In all cases, the powders were cold isostatically pressed and processed by XD™ synthesis. The resulting product was crushed, milled to ≤ 63 μm size, vacuum hot-pressed at 1473K for 2 h under a load of 20 MPa, and subsequently hot isostatically pressed (HIPed) to full density at 1473K for 4 h in argon at a pressure of 200 MPa.

In an effort to reduce the amount of oxides which occur at prior particle boundaries in the powder processed alloys, in the present effort, instead of using the ≤63 μm size, the following size distribution was used:

50% in the 150μm to 90μm size range
10% in the 90μm to 44μm size range
40% in the ≤44 μm size range

The inclusion of larger particles up to 150 μm in diameter and the use of a trimodal distribution rather than a Gaussian distribution required a higher hot pressing temperature of 1498K to attempt achieving the desired densification. In spite of using the higher temperature, full densification was not achieved during hot pressing and subsequent HIPing was unsuccessful in rectifying the problem. So all the hot pressed and HIPed material were forged to eliminate porosity. An added advantage of the forging step is that it introduces some flow in the material that may aid in breaking up prior particle boundaries as well as oxide and TiB_2 clusters. It was hoped that such deformation would enhance the ductility of the P/M processed materials which, both in the monolithic and composite forms exhibited ductile-to-brittle transition at temperatures above 873K (final report of the previous program) whereas the monolithic ingot metallurgy counterpart exhibits some tensile plasticity even at room temperature. These P/M forgings were then homogenized to ensure that an equilibrium microstructure was present prior to mechanical testing.

B. HEAT TREATMENT

SInce the monolithic materials were intended to be single phase solid solution alloys, the only major role of heat treatment would be to influence the grain size. If however the quaternary alloys turned out to be multiphase in nature, then various heat treatments can be used to influence the size, amount and distribution of the second phase and by default, influence the matrix composition. The as-forged monolithic forgings were heat treated and the change in grain size was monitored. Mechanical properties including bend ductility and compressive yield strength were measured for the coarse grained material and compared to the data obtained for the as-forged counterpart.

C. MECHANICAL TESTING

1. Compression Tests

Compression specimens (5.1 mm diameter x 10.9 mm high) were electrodischarge-machined from the HIPed material and the forgings and tested at a strain rate of ~10^{-4} s^{-1} at temperatures ranging from 300K to 1373K. In some instances, compression tests were performed at 77K in liquid nitrogen (77K) and at 205K in a methanol/dry ice solution. Load-displacement curves were generated and from these, the 0.2% offset yield strength was calculated as a function of temperature.

In addition, slow-strain-rate compression studies were done at NASA Lewis Research Center at constant crosshead speeds. Strain rates ranged from 2 x 10^{-4} s^{-1} to 2 x 10^{-7} s^{-1}, and temperatures from 900K to 1200K. Samples were deformed in air to ~8 percent strain. True compressive stresses, strains, and strain rates were calculated from the autographically recorded load-time charts by the offset method (38), under the assumption of constant volume.

2. Bend Tests

Three-point bend tests were performed on ground and polished specimens (32 mm x 7.9 mm x 3.1 mm) cut from the quaternary forgings, and load-displacement curves were generated. For tests at room temperature and 473K, resistance strain gages were glued onto the tensile side of the bend specimens. Bend tests at higher temperatures (up to 873K) were performed without strain gages, due to their temperature limitations. Load-strain curves were generated from the output of the resistance strain gages used for the tests at room temperature and at 473K.

The composites produced via the P/M-XD™ route were also tested in three point bending. Since the conventional bend-test jig uses tool steel pins, which limit the test temperatures to ~873K, a ceramic jig was fabricated to handle temperatures up to 1100K. The ductile-to-brittle transition temperature was defined as the minimum temperature where the load-displacement curve deviated from linearity.

3. Tensile Tests

Cylindrical "buttonhead" tensile specimens were electrodischarge-machined with the gage length lying in the radial plane of the monolithic forgings, finish-ground with 10-μm grit silicon carbide paper, and tested at a strain rate of ~10^{-4} s^{-1} from ambient to 1073K. The 0.2% offset yield strength and plastic elongation were determined from the resulting load-displacement curves.

D. MICROSTRUCTURAL CHARACTERIZATION

X-ray diffraction (XRD), differential scanning calorimetry (DSC), optical microscopy, scanning electron microscopy (SEM) with fully quantitative energy-dispersive X-ray (EDX) analysis capabilities, and transmission electron microscopy (TEM) were used to characterize the materials produced in this program. Microstructure was characterized after hot processing, casting, homogenizing, and forging. Post-deformation microstructures were also examined. Fracture surfaces obtained from the bend and tensile tests were characterized by SEM. TEM samples were prepared by electrolytic jet polishing of 3-mm circular sections electrodischarge-machined from thin sections. Jet polishing was performed in a 25% HNO_3-methanol solution at 243K at 12-15 V.

V. RESULTS AND DISCUSSION

A. UNIAXIAL TENSION TESTING OF FORGED $Al_{67}Ti_{25}Cr_8$

In this section the results of tensile tests conducted on forged $Al_{67}Ti_{25}Cr_8$ between 293K and 1073K at a strain rate of $\sim 5\times10^{-5}$ s^{-1} are reported. Cylindrical "buttonhead" tensile specimens (Fig. 2) were electrodischarge-machined with the gage length (12.7 mm) lying in the forging plane and tested in air. Due to limitations in material availability and difficulties in machining tensile specimens, only one test was conducted at each temperature. The 0.2% offset yield strength and ductility were measured. The resulting fracture surfaces were examined in a scanning electron microscope (SEM) and thin foils from the as-forged material and from the gage section of the tensile specimen that was deformed at 1073K were examined in a JEOL 100CX transmission electron microscope (TEM).

The as-forged material was shown by X-ray diffraction to be substantially single-phase with an $L1_2$ structure. Results of chemical analysis on the casting and forging are shown together with the target composition in Table I. The microstructure appeared recrystallized, with a grain size of ~40 μm (Fig. 3a) and no significant differences between the radial and through-thickness orientations. The presence of subgrains was confirmed, as seen in the representative micrograph of Fig. 3b, as well

Table I: Target and Measured Compositions of the Ternary $L1_2$ Compound $Al_{67}Ti_{25}Cr_8$ (wt. %)

	Al	Ti	Cr	O	N	C	H
Target	52.8	35.0	12.2	-	-	-	-
Casting (measured)	52.4	35.0	12.5	-	-	-	-
Forging (measured)	51.7	35.9	12.3	0.15	0.03	0.02	0.003

as a small amount of second phase with rod or platelet morphology. These platelets were observed in the as-cast condition and remained after homogenization. They were optically resolvable, and were determined by SEM/EDX (energy-dispersive X-ray) analysis to correspond to a "Ti_2Al" composition. However, SEM/WDX (wavelength-dispersive analysis) indicated a higher carbon content than in the matrix, leading to a tentative identification of these precipitates as Ti_2AlC.

The variation in the 0.2% offset yield strength with test temperature (Fig. 4) is similar to that previously observed for $Al_{66}Ti_{25}Mn_9$ (3), although the strengths shown in Fig. 4 are about 20% higher over the entire temperature range tested. Specifically, there is a discontinuous drop in yield strength -- from ~370 MPa at 623K to ~250 MPa at 773K -- and further increases in temperature up to 1073K result in a gradual decrease in yield strength. Below 623K, the specimens fail prior to reaching yield, consistent with the behavior previously observed in three-point bend tests (2). At 1073K, where the yield strength was 230 MPa, the ultimate tensile strength was 304 MPa, and localized necking was observed.

The observed discontinuous drop in strength between 623K and 773K is not likely due to precipitate dissolution since differential scanning calorimetry studies revealed no reaction in this temperature range. Likewise, TEM studies of the forged material prior to testing (Fig. 3b) indicated no obvious precipitation either in the matrix or at grain or subgrain boundaries; moreover, such a discontinuous drop in strength was not previously observed in compression (2). The dimensions of the "pancake" forgings required tensile specimens used in the present study to be machined with the tensile axis normal to the forging direction whereas the compression studies were performed in the previous study (2) with the compression axis parallel to the forging axis. It was thus previously suggested (3) that the observed differences in the yield strength - temperature profiles in tension and compression may be related to texture effects. Texture measurements were made on $Al_{67}Ti_{25}Cr_8$ at the University of Virginia in Charlottesville. Two specimens were examined. One was obtained in the forging plane and the second was machined nomal to the forging plane. Texture measurements were made for {111} and {200} preferred orientations. Representative pole figures are shown in Figures 5a-d. The contours are plotted in increments of 0.5. A significant texture is not observed in either specimen with the strongest peak being 5 times random. Thus, the observed anisotropy in compression and tension is not a consequence of texture. Further, in the present study, compression tests were additionally performed on specimens whose loading axis was normal to the forging axis (i.e. same orientation as the tensile specimens). Compressive yield strength appears independent of specimen orientation (Fig. 6) suggesting that the observed difference in strength between tension and compression is not a consequence of differences in specimen orientation with respect to the forging axis. At present, we are unable to offer a reasonable metallurgical explanation for this behavior. If this behavior is a consequence of the mechanical test procedure adopted, both in this study and in the previous report (3), we are unaware of the source of such an error.

The effect of test temperature on ductility is shown in Fig. 7: no ductility below 623K, a permanent elongation of 0.2% at 623K, and a reproducible decrease to zero at 773K, again similar to the response observed for $Al_{66}Ti_{25}Mn_9$ (3). A specimen with a thin film of gold sputtered on the gage section prior to testing at 773K plastically elongates to 1% strain rather than failing in the brittle fashion of the uncoated specimens at this temperature. Nevertheless, there is no appreciable difference between the fracture stress of the uncoated specimen and the yield stress of the gold-coated specimen. At the higher temperature of 923K, even without the gold film, ductility is restored to ~1.3%, and at 1073K, up to 18.7% plastic elongation is obtainable.

Representative micrographs of the fracture surfaces of specimens tested at 623K and 773K show transgranular cleavage to be the predominant failure mode (Fig. 8a,b). At 923K, where some tensile ductility was observed (~1.3%), fracture propagates by both transgranular cleavage (Fig. 8c) and intergranularly (Fig. 8d). Approximately half of the fracture surface appears intergranular. Thus, in $Al_{67}Ti_{25}Cr_8$, intergranular failure was observed only above 773K in uniaxial tension, whereas in the $Al_{66}Ti_{25}Mn_9$ (3), some intergranular failure occurred even at 473K. In $Al_{67}Ti_{25}Cr_8$ deformed in three-point bending, intergranular failure occurred at 723K but only on the compressive side of the specimen; at 873K, intergranular fracture was mixed with transgranular cleavage over the entire section (2). The fracture surface of the Au film-protected specimen tested at 773K is shown in Fig. 9a,b. Fracture occurs predominantly by transgranular cleavage (Fig. 9a). Some intergranular failure is observed (Fig. 9b), although such instances were very few.

The features on the fracture surface of the 1073K specimen which exhibited 18.7% elongation are unusual; although it appears to have failed by cleavage, the delineation of grain boundaries suggests an intergranular failure mode (Fig. 10a). In addition, this fracture surface is interrupted by delaminated regions (indicated by arrows in Fig. 10a and shown at a higher magnification in Fig. 10b) which appear to be at or in the vicinity of grain boundaries. The gage surface in the necked region adjacent to the fracture surface (Fig. 10c) has a rumpled appearance with frequent grain boundary separation. A higher magnification micrograph (Fig. 10d) of one such secondary crack shows the grain boundary planes with a wavy structure resembling the delamination features in Fig. 10b. The nodule-like features lying along the grain boundary in Fig. 10d (indicated by an arrow) may represent fine recrystallized grains adjacent to an original boundary.

Optical micrographs of the deformed gage section (parallel to the stress axis) of the 1073K specimen with 18.7% ductility reveal two interesting features: (a) the presence of serrated grain boundaries (Fig. 11a), and (b) fracture of the small amounts of "fibrous" precipitates present in this material, which suggests that they are unable to accommodate the matrix deformation (Fig. 11b). For purposes of comparison, the "buttonhead" sections of the same specimens were also examined, since this region experienced the same thermal history as the gage section but not the same stresses and strains. The grain boundaries in the "buttonhead" region are not serrated (Fig. 11c) and the precipitates are not fractured by prior processing (Fig. 11d).

Representative TEM micrographs of a thin foil from the necked region of the extensively deformed specimen (1073K, 18.7% elongation) are shown in Figs. 12a,b. In general, there is a high dislocation density, and the serrated grain boundaries observed optically are clearly seen (Fig. 12a). Frequently, the serrated peaks are associated with sub-boundaries. Fine recrystallized grains substantially free of dislocations were frequently observed and one such instance is shown in Figure 12b. It is likely that recrystallization is dynamic although at present there is not enough evidence that they did not form statically during cooling after the test.

The observed delamination in the 1073K specimen that was deformed to ~19% elongation (Figure 10b) is believed to be simply a manifestation of intergranular cracks propagating along serrated boundaries. Mullendore and Grant (39) reported that grain boundary serrations occurred only in conjunction with grain boundary sliding and migration, forming after an elongation sufficient to produce a substructure adjacent to the boundary. They contended that the peaks of the serration represented the intersection of subgrains with the grain boundary and were, thus, similar to a grain boundary triple point in acting as a crack-nucleation source. Lytton et al. (40) rationalized the formation of serrated grain boundaries in creep as a sequence of events that included the formation of shear faults along a grain boundary and, thereby, lattice bending stresses. Edge dislocations would then accumulate and polygonize at such shear faults so as to form tilt boundaries that relieved the bending stresses. The grain boundary migrates towards these tilt boundaries to equalize the interfacial tension, causing the boundary to assume a serrated morphology.

Figure 13a-c shows a region in the same specimen in the vicinity of a crack induced by damage during handling at room temperature. The crack has a "saw-tooth" appearance, propagating transgranularly in the foil and being deflected at regular intervals. At the point where the crack transitions from one system to another (i.e., at the "saw tooth"), there is a deformation band in which closely spaced dislocations lie on the slip plane (Fig. 13b,c). Slip initiated by the stress ahead of the crack tip makes these deformation bands thinner than the surrounding region, so that the crack propagates along them preferentially. In some instances, even with such deformation bands ahead of the crack tip, the crack does not deflect if it is energetically feasible for it to continue on the same slip system. As a consequence, such deformation bands can run at an angle to the crack (far left, Fig. 13a).

In the present study, $Al_{67}Ti_{25}Cr_8$ appeared to dynamically recrystallize to some degree during deformation at 1073K. Dynamic recrystallization has been observed in several $L1_2$ alloys, including Ni_3Al (41,42) and Zr_3Al (43) and the occurrance has been rationalized on the basis of a low SISF energy. However, fault energy values for $Al_{67}Ti_{25}Cr_8$ are not available at present although SISF energy data for other similar compounds, (260 mJ/m2 for Al_3Sc and 100 mJ/m2 for $Al_{67}Ti_{25}Fe_8$) have been reported (1, 44). It is argued that the SISF energy for $Al_{67}Ti_{25}Cr_8$ is not likely to be very low since recovery and recrstallization are observed in the present study.

B. FURTHER CHARACTERIZATION OF P/M-PROCESSED MONOLITHIC $Al_{66}Ti_{25}Mn_9$ AND $Al_{67}Ti_{25}Cr_8$ AND THEIR TiB_2-CONTAINING COUNTERPARTS

The compression behavior of these materials as a function of temperature (Fig. 1a) and at high temperatures as a function of strain rate was examined and the observed results were previously reported (44). In this section, TEM characterization of the hot pressed material, and after testing, are described. Based on these observations, intermediate temperature heat treatments were selected and specimens subjected to these heat treatments were compression tested. The results of these tests are also included.

a. Hot-pressed microstructure:

Representative micrographs of the hot pressed monolithic material reveal a fairly high oxide content, frequently at prior particle boundaries (Fig. 14a), a very fine mean grain size and some oxides in the interior of such grains (Fig. 14b). In the composite materials, it was difficult to differentiate between the oxides and TiB_2 particles optically, although using TEM, the difference in morphology between these could be recognized (compare Fig. 14b and 15a); it can be seen from Fig. 15b that the TiB_2 particles are typically 0.5 µm in size. For the most part, these TiB_2 particles were uniformly distributed, although some regions devoid of these particles could be found. In these regions, the grain size was similar to that observed in the monolithic material (Fig. 14b). In regions containing TiB_2 particles, distinct grain boundaries were not easily discernible. It is noted that the grain size in these P/M processed monolithic and TiB_2 -containing materials are significantly finer than the grain size previously reported for forged ingot metallurgy material by Brown et al.(45).

b. Deformed microstructure:

The microstructure of the monolithic $Al_{66}Ti_{25}Mn_9$, deformed at 1000K at strain rates of 2×10^{-4} s^{-1} and 2×10^{-7} s^{-1} was examined in a transmission electron microscope. At the fast strain rate, dislocation tangles were present in the matrix (Fig. 16a) with little evidence of subgrain formation. Weak beam examination showed the dislocations to be separated into superpartials (Fig. 16b), and using **-g** and **+g** conditions, these were confirmed not to be dipoles. Deformation at the slow strain rate caused subgrain formation and in addition, dislocations were present in the grains and subgrains (Fig. 16c,d).

The deformed microstructure of $Al_{66}Ti_{25}Mn_9$ containing 20 vol.% TiB_2 particulates was also examined after 1000K deformation at strain rates 2×10^{-4} s^{-1} to 2×10^{-7} s^{-1}. Representative micrographs of a specimen deformed at the fast strain rate are shown in Fig. 17a,b. Several interesting features are evident in these micrographs. First, the TiB_2 particles are stable 1000K, even under an applied stress.

The particles do not appear to have coarsened and they retain their sharp edges and corners suggesting negligible dissolution. Second phase precipitation with a "tweed" morphology is evident in the matrix. Grain boundary pinning by the TiB_2 particles can also be seen in Fig. 17a. Finally, the effectiveness of these particles in pinning dislocations (or alternately, generating them at the interface due to elastic discontinuity) is noted in Fig. 17b. The presence of precipitates in the deformed specimen and their absence in the hot pressed condition suggest that the matrix of the composite material could be a supersaturated $L1_2$ metastable single phase in the hot pressed condition. Likewise, the composite specimen deformed at 1000K at the slow strain rate also exhibits second phase precipitation in the matrix, Fig. 18a. A selected area diffraction pattern using a $[001]_m$ zone axis (Fig. 18b) confirms the precipitates to lie on the cube planes of the matrix and their lath morpholgy and thinness give rise to the observed streaks and maxima in the diffraction pattern. These precipitates are thought to be Al_2Ti based on the recent work of Potez et al. (46).

c. Effect of an intermediate temperature heat treatment

The precipitation of a second phase in the composite material during deformation at 1000K implies a supersaturated matrix in the hot pressed condition. Thus, the observed mild positive dependence of strength on temperature in Fig. 1a for the composite material may be a consequence of precipitation during the test and/or a simultaneous change in matrix composition. Thus it would be interesting and informative to precipitate the second phase before testing using an intermediate temperature heat treatment and then testing the two-phase matrix containing the TiB_2 particulates in compression at various temperatures. The role of solid solution strengthening versus precipitation hardening can also be elucidated. Care must be however exercised in interpreting the observations since the matrix composition changes simultaneously and it is known that the matrix chemistry can influence the shape of the compressive yield strength-temperature profile for $L1_2$ compounds (47).

Three heat treatments were selected and compression specimens machined from the hot pressed compacts were heat treated according to those schedules and then tested in compression in the temperature range 77K - 873K. The first heat treatment involved annealing the specimens at 973K for 48h. The second heat treatment was based on a two-step process where a set of forged specimens were first annealed at 973K for two days as before but then in addition, a second anneal at 773K for 360h was included. The third heat treatment included the two steps in the previous schedule together with a further exposure at 573K for 400h (i.e. 973K/2 days + 773K/360h + 573K/400h).

Representative TEM micrographs of the specimens heat treated at 973K for a day, shown in Fig. 19a,b confirm the precipitation of a second phase with a lath morphology and the $[001]_m$ zone axis diffraction pattern is similar to that previously observed in the 1000K deformed specimen (Fig. 18b). Compressive yield strength-temperature profiles obtained by testing specimens subjected to the various aforementioned heat treatments are compared to the profile generated for the as-hot-pressed specimens in Fig. 20. Clearly, the intermediate temperature heat treatment of 973K/2days increases the strength relative to the hot pressed condition for all temperatures in the range 77K - 873K except at the high temperature end, where the strengths converge, likely a consequence of precipitate redissolution in the heat treated specimens. It is also noted that the positive temperature dependence of strength is not as evident as in the hot pressed condition which may reflect the change in matrix composition or the absence of significant precipitation during the test. Finally, the location of the strength peak is shifted to lower temperatures by the single step heat treatment.

Based on the strength-temperature profiles, it is recognized that the heat treatment temperature of 973K is likely on the high end of the precipitation regime for this material. Thus, inspite of the intermediate temperature heat treatment, the matrix is likely still supersaturated. Thus, the previously described two-stage heat treatment was used to further relieve the supersaturation. Strength-temperature profile following the two-stage heat treatment is include in Fig. 20. A further enhancement in strength is noted at most temperatures relative to the one-step anneal except at 873K, where the strength drops precipitously. Of interest is the fact that a pronounced positive temperature dependence of strength is observed suggesting that this is more likely a matrix composition effect than precipitation during the test. The position of the peak has not shifted relative to the curve obtained for the specimens subjected to the single stage heat treatment. Three specimens were tested following the triple cycle heat treatment and tested at 473K, 573K and 673K. The measured strengths are similar to those obtained for the previous set of specimens (973K/2days + 773K/360h) at the corresponding temperatures.

C. PRELIMINARY CHARACTERIZATION OF THE QUATERNARY SOLID SOLUTION ALLOYS

It was indicated earlier that to obtain a balance of strength and ductility, and to a lesser extent, oxidation resistance, it is necessary to examine solid solutions of the ternary $L1_2$ compounds. In this section, results from preliminary studies, undertaken to evaluate the existence of single phase $L1_2$ solid solutions between pairs of ternary $L1_2$ trialuminides are presented. Based on the findings, four quaternary compositions were selected for further evaluation. These were cast as two-kilogram ingots, homogenized and then isothermally forged into pancakes. In a subsequent section, results from compression, bend and a limited number of tensile tests on these forgings are reported.

For the preliminary studies, small ingots (~50 g) of 9 different quaternary compositions in the Al-Ti-Mn-Cr, Al-Ti-Cr-Fe and Al-Ti-Mn-Fe systems were cast, homogenized and examined. Three compositions were produced in each quaternary system of the type $Al_{66}Ti_{25}(X0.75Y0.25)_9$, $Al_{66}Ti_{25}(X0.5Y0.5)_9$, $Al_{66}Ti_{25}(X0.25Y0.75)_9$. These were characterized using optical microscopy, x-ray diffraction and hardness.

Chemical analysis of the nine quaternary compositions that were produced in the form of 50 g ingots revealed good agreement between measured and target values (Table II). In all cases, optical microscopy as well as x-ray diffraction confirmed the presence of a substantially single phase microstructure in the cast and homogenized condition. Since these ingots were slow-cooled, they exhibited fairly large grains (2-5 mm) and therefore, depending on the orientation, a range of hardness values were obtained. In addition, these homogenized ingots exhibited porosity and it is possible that subsurface pores influenced the hardness measurements. The variation in hardness with composition is shown in Fig. 21 for the three quaternary systems. In the Al-Ti-Cr-Mn system, the hardness is essentially insensitive to composition (i.e. ratio of third and fourth element) although it is tempting to suggest a minimum at $Al_{66}Ti_{25}Cr_{4.5}Mn_{4.5}$. In the Al-Ti-Fe-Cr system, the hardness of the ternary $Al_{66}Ti_{25}Cr_9$ and all the quaternary compositions examined are similar, although the ternary Fe-based compound is significantly harder. Of the three quaternary systems examined, perhaps the Al-Ti-Mn-Fe system is most interesting in that a distinct hardness minimum was observed at the composition

Table II. Target and Measured Compositions (wt.%) for the Preliminary (50g) Quaternary $L1_2$ Trialuminide Castings.

Alloy	Al	Ti	Cr	Mn	Fe
$Al_{66}Ti_{25}Cr_{6.75}Mn_{2.25}$	48.7(51.6)*	37.3(34.7)	10.3(10.2)	3.6(3.58)	--
$Al_{66}Ti_{25}Cr_{4.5}Mn_{4.5}$	49.4(51.5)	35.7(34.6)	7.44(6.76)	7.46(7.15)	--
$Al_{66}Ti_{25}Cr_{2.25}Mn_{6.75}$	50.1(51.4)	35.3(34.6)	3.47(3.38)	11.1(10.7)	--
$Al_{66}Ti_{25}Cr_{6.75}Fe_{2.25}$	48.2(51.5)	37.2(34.7)	10.6(10.2)	--	4.0(3.64)
$Al_{66}Ti_{25}Cr_{4.5}Fe_{4.5}$	49.5(51.4)	35.3(34.6)	7.32(6.76)	--	7.86(7.26)
$Al_{66}Ti_{25}Cr_{2.25}Fe_{6.75}$	48.7(51.3)	35.6(34.5)	3.55(3.37)	--	12.2(10.9)
$Al_{66}Ti_{25}Mn_{6.75}Fe_{2.25}$	48.6(51.3)	35.8(34.5)	--	11.5(10.7)	4.1(3.61)
$Al_{66}Ti_{25}Mn_{4.5}Fe_{4.5}$	47.9(51.2)	36.5(34.4)	--	7.54(7.11)	8.1(7.23)
$Al_{66}Ti_{25}Mn_{2.25}Fe_{6.75}$	48.0(51.2)	36.4(34.4)	--	4.0(3.55)	11.7(10.8)

* Target compositions are provided within parentheses

corresponding to $Al_{66}Ti_{25}(Mn0.75Fe0.25)_9$. This composition may therefore favor a higher ductility than the other compositions in this system. Based on these findings, four quaternary compositions were selected for further investigation: $Al_{66}Ti_{25}Cr_{4.5}Mn_{4.5}$, $Al_{66}Ti_{25}Cr_{4.5}Fe_{4.5}$, $Al_{66}Ti_{25}Fe_{4.5}Mn_{4.5}$, and $Al_{66}Ti_{25}Mn_{6.75}Fe_{2.25}$. In addition, the 4.5Cr in the compound $Al_{66}Ti_{25}Cr_{4.5}Mn_{4.5}$ was replaced by 3.0 Cr and 1.5 Fe to yield a quinary composition $Al_{66}Ti_{25}Mn_{4.5}Cr_{3.0}Fe_{1.5}$.

Results of chemical analysis on forgings of these compositions are provided in Table III. Good agreement is observed between target and measured values. Interstitial levels in the forgings were also measured and are shown in Table IV. X-ray diffraction studies indicated a substantially single phase $L1_2$ structure in all cases and this was verified by optical microscopy and TEM. Representative optical micrographs of two quaternary compositions and the quinary alloy are shown in Fig. 22a-c. In general, a single phase microstructure is present with an approximate grain size of 15-20 μm in all cases. This is in contrast to the 30-40 μm grain size previously reported (45) for the ternary alloys. This difference in grain size is likely a consequence of the slightly larger reduction ratio used in the present study. Transmission electron microscopy studies revealed the presence of a small amount of coarse, rod-shaped or globular precipitates in some of the quaternary alloys (Fig. 23a), although selected area diffraction patterns (Fig. 23b) did not reveal any extraneous spots characteristic of extensive matrix precipitation. In both the quaternary and quinary alloys subgrain boundaries were observed (Fig. 23c) and, occasionally, in the quinary alloy precipitates were present at the grain and subgrain boundaries (Fig. 23d).

Table III. Target and Measured Compositions (wt.%) for the large Quaternary $L1_2$ Trialuminide Castings that were Forged

	Al	Ti	Mn	Cr	Fe
$Al_{66}Ti_{25}Mn_{4.5}Cr_{4.5}$	53.3 (51.5)*	32.3 (34.6)	7.40 (7.15)	6.97 (6.76)	0.10 (0.0)
$Al_{66}Ti_{25}Fe_{4.5}Cr_{4.5}$	51.4 (51.4)	34.0 (34.6)	<0.10 (0.0)	7.30 (6.76)	7.30 (7.26)
$Al_{66}Ti_{25}Mn_{4.5}Fe_{4.5}$	52.1 (51.2)	33.4 (34.4)	7.14 (7.11)	0.47 (0.0)	6.91 (7.23)
$Al_{66}Ti_{25}Mn_{6.75}Fe_{2.25}$	51.7 (51.3)	33.2 (34.5)	10.8 (10.7)	0.24 (0.0)	3.96 (3.62)
$Al_{66}Ti_{25}Mn_{4.5}Cr_3Fe_{1.5}$	50.8 (51.4)	34.1 (34.6)	7.55 (7.13)	4.77 (4.5)	2.74 (2.42)

* values in parentheses are target compositions

Table IV: Measured Interstitial levels in some of the Quaternary Forgings (wt. %).

Compound	Oxygen	Nitrogen	Hydrogen	Carbon
$Al_{66}Ti_{25}Mn_{4.5}Cr_{4.5}$	0.189	0.190	0.0007	0.061
$Al_{66}Ti_{25}Mn_{6.75}Fe_{2.25}$	0.088	0.164	0.0003	0.240
$Al_{66}Ti_{25}Mn_{4.5}Cr_{3.0}Fe_{1.5}$	0.075	0.076	0.0004	0.034

D MECHANICAL BEHAVIOR OF THE QUATERNARY COMPOUNDS

The variation in compressive yield stress with test temperature for the various quaternary alloys are compared against their ternary counterparts in Fig. 24a,b. It can be seen that $Al_{66}Ti_{25}Cr_{4.5}Mn_{4.5}$ is marginally stronger than either of its ternary counterparts (Fig. 24a) although this strength enhancement is thought to be an effect of grain size rather than composition. Replacing a part of the Cr with Fe to yield the quinary composition causes an improvement in strength, particularly at the higher temperatures; thus at 1000K, the yield strength of the quinary composition corresponds to ~300 MPa as compared to ~220 MPa for the ternary alloys (Fig. 24a). The grain sizes in the quaternary and quinary compounds in Fig. 24a were similar. Likewise, in Fig. 24b, increasing substitution of Fe for Mn increases the strength, although the ternary Fe-based compound is not very strong at high temperatures. Finally, a comparison is also drawn between the compressive yield strength-temperature profiles for $Al_{67}Ti_{25}Cr_8$ and $Al_{66}Ti_{25}Cr_9$. These two forgings exhibit similar behavior and minor differences in strength can be explained on the basis of grain size differences.

The effect of strain rate on compressive flow stress in the temperature range 900K-1100K for the various quaternary and quinary compositions are compared to the ternary compounds in Fig. 25a-c. From Fig. 25a, it is seen that the quaternary alloy $Al_{66}Ti_{25}Cr_{4.5}Mn_{4.5}$ responds similar to the ternary $Al_{67}Ti_{25}Cr_8$ and $Al_{66}Ti_{25}Mn_9$. In Fig. 25b, the quinary alloy is compared against the response obtained from the quaternary composition $Al_{66}Ti_{25}Mn_{6.75}Fe_{2.25}$. At 900K, both compositions are insensitive to strain rate, in the range examined, although the quinary compound is stronger. At 1000K, the quinary alloy still maintains strain rate insensitivity whereas, for the quaternary alloy, flow stress decreases upon decreasing the strain rate from ~$2x10^{-6}s^{-1}$ to ~$2x10^{-7}s^{-1}$. At 1100K, both compounds exhibit strain rate sensitivity, although the stress exponent for the quinary appears to be higher than for the quaternary compound. Likewise in Fig. 25c, the quaternary compound is stronger than the ternary $Al_{66}Ti_{25}Cr_9$ although the difference diminishes with increasing temperature and decreasing strain rate.

Three point bend tests were conducted on the quaternary and quinary forgings to investigate the potential for low temperature ductility. A few tests were also conducted on the quaternary $Al_{66}Ti_{25}Mn_{6.75}Fe_{2.25}$ at higher temperatures. Specimens tested at 300K and 473K had strain gages glued to their tensile side to enable direct strain measurements. The results of this study are summarized in Table V below. None of the compounds exhibited significant plasticity at 300K and 473K.

Table V Three Point Bend Data at 300K and 473K for the Ingot Metallurgy Processed Quaternary and Quinary Forgings.

Composition	Test Temp. (K)	Propor. Stress (MPa)	Fracture Stress (MPa)	Plastic Strain (%)
4.5Cr-4.5Mn	300	372	449	0.02
	300	---	369	0
	473	321	~450	0.20
6.75Mn-2.25Fe	300	449	543	0.06
	473	307	~417	0.24
4.5Mn-3.0Cr-1.5Fe	300	---	247	0
	300	---	168	0
	473	398	511	0.01
4.5Cr-4.5Fe*	300	---	248	0
4.5Mn-4.5Fe*	300	---	165	0

* Forgings of these materials contained microcracks

Tension tests were performed on the quaternary compositions and the quinary alloys. In general, these compositions were disappointing in that they were brittle relative to the Cr- or Mn-based ternary alloys. For the quaternary compositions $Al_{66}Ti_{25}Cr_{4.5}Mn_{4.5}$ and $Al_{66}Ti_{25}Mn_{6.75}Fe_{2.25}$, tension tests were also performed at several temperatures whereas the quinary alloy was only tested at 1073K and 923K. The quaternary compositions containing 4.5 at.% Fe (i.e. $Al_{66}Ti_{25}Fe_{4.5}Cr_{4.5}$ and $Al_{66}Ti_{25}Mn_{4.5}Fe_{4.5}$) exhibited what appeared to be fine hairline cracks in the forging and thus, were not tested in tension (tension specimens are expensive to machine and therefore are only made after microstructural features and compression/bend tests are performed). Tensile results for the alloy containing Mn and Fe in the ration 3:1 (i.e. $Al_{66}Ti_{25}Mn_{6.75}Fe_{2.25}$) and for the quinary alloy ($Al_{66}Ti_{25}Mn_{4.5}Cr_{3.0}Fe_{1.5}$) are provided in Table VI. In the quaternary alloy, no

Table VI: Tensile Properties for the Quaternary and Quinary I/M-Processed Monolithic Forgings.

Compound	Test Temp. (K)	$\sigma_{0.2}$ (MPa)	$\sigma_{frac.}$ (MPa)	Elong. (%)
$Al_{66}Ti_{25}Mn_{6.75}Fe_{2.25}$	1073(#1)	--	216	--
	1073(#2)	--	231	<0.1
	923	--	93	--
	623	--	147	--
$Al_{66}Ti_{25}Mn_{4.5}Cr_{3.0}Fe_{1.5}$	1073	294	303	0.56
	923	--	139	--

ductility was obtained, even at 1073K, and fracture frequently occurred outside the gage section. Two specimens were tested at 1073K and both exhibited similar fracture stresses (216, 231MPa). These stresses are similar to yield stress values obtained for the ternary $Al_{66}Ti_{25}Mn_9$ at 1073K. At lower temperatures, the fracture stresses were very low. The quinary alloy exhibited ~0.5% plastic elongation at 1073K with a yield strength of ~300 MPa. At 923K however, the alloy was brittle. In both cases fracture occurred within the gage section. Variations in yield strength and ductility with test temperature are shown in Fig. 26a,b for $Al_{66}Ti_{25}Mn_{4.5}Cr_{4.5}$. Below 923K, the specimens fail at very low strength levels with no accompanying ductility. At 923K, the yield strength is approximately equal to that obtained for $Al_{67}Ti_{25}Cr_8$ although the ductility is low. Likewise at 1073K, 1.5% ductility was obtained for the quaternary composition for a yield strength of ~250 MPa. For a similar yield strength, the ternary $Al_{67}Ti_{25}Cr_8$ exhibited ~19% ductility.

The fracture surfaces of the tensile specimens of the quaternary composition, $Al_{66}Ti_{25}Cr_{4.5}Mn_{4.5}$ were similar in appearance to the ternary $Al_{66}Ti_{25}Mn_9$ in that at low temperatures, transgranular cleavage predominates (Fig. 27a) whereas with increasing test temperatures, fracture transitions to intergranular failure (Fig. 27b,c). At test temperatures where fracture occurred at low stresses (473K-773K, Fig. 26a), the fracture surfaces appeared to contain a single fracture initiation site (Fig. 27d), although the source of crack initiation was not obvious. The 1073K fracture surface of the quinary alloy ($Al_{66}Ti_{25}Mn_{4.5}Cr_{3.0}Fe_{1.5}$) (which showed the highest strength in tension and compression at the high temperatures) was rather interesting. At this temperature, fracture occurred intergranularly (Fig.28a). It is possible that the nodule on the grain boundary is a recrystallized grain or alternately, a precipitate. On the same boundary adjacent to the nodule, is a feature suggesting precipitate pull-out. Some of the grain boundaries exhibited fine dimples (Figure 28b) suggestive of micropores or precipitate pull-out. On another grain boundary (Figure 28c), fine precipitate-like features were observed that are of about the same size as the "dimples" in Figure 28b. The nature of these precipitates is unknown at present.

E. MECHANICAL BEHAVIOR OF THE PARTICULATE-REINFORCED QUATERNARY ALLOYS

Representative optical micrographs of the forged composites are shown in Fig. 29a-c before and after etching. A layered structure, typical of a forged material is evident. Regions containing a low volume fraction of TiB_2 particulates are evident in Fig. 29b implying a microscopically non-uniform distribution of these particles. A high magnification SEM micrograph (Fig. 29c) emphasizes the clustering of these particles into colonies.

Compression behavior of the particulate composites were examined as a function of temperature and the results are summarized in Fig. 30 in the form of compressive yield strength-temperature profiles. In addition, the variations in yield strength with temperature for monolithic P/M-processed $Al_{67}Ti_{25}Cr_8$ with a fine grain size of 3-5μm and for P/M-processed $Al_{66}Ti_{25}Cr_9$ with a grain size of ~25μm are also included (Note: for similar grain sizes, $Al_{66}Ti_{25}Cr_9$ and $Al_{67}Ti_{25}Cr_8$ exhibit similar strength levels). Irrespective of the matrix composition, the particulate composites exhibit yield strengths in the range 1000-1200 MPa up to ~900K. At higher temperatures a dramatic decrease in strength occurs reaching ~300 MPa at 1173K. This decrease in strength is attributed to the fine grain size in the composite as well as to the dissolution of the fine second phase that precipitates on the $[100]_m$ planes in these materials. The effect of the fine grain size on strength variations with temperature is also seen by comparing the two ternary monolithic materials (Fig. 30).

The effect of strain rate at 900K-1100K on the flow strength of such particulates-reinforced composites can be appreciated by examining the data in Fig. 31.

Independent of matrix composition, at all temperatures examined, flow stress decreases with decreasing strain rate. Thus, for example, for the two composites in Fig. 31, at 1000K and a strain rate of ~$2x10^{-4}s^{-1}$, compressive flow stress at 1% strain corresponds to ~600 MPa; at ~ $2x10^{-7}s^{-1}$, the corresponding value is ~300-350 MPa.

Three-point bend tests were conducted as a function of temperature on the P/M-processed monolithic and composite materials to obtain the ductile-to-brittle transition temperature (DBTT) for these materials. Results of these tests are provided in Table VII. These results show that the DBTT for these composites is fairly independent of matrix composition, is around 950K-1000K, and is likely governed by the microstructure rather than the intrinsic matrix composition. It can also be seen from Table VII that the P/M-processed, coarse grained $Al_{66}Ti_{25}Cr_9$ is ductile in bending at 473K, which is similar to the I/M-processed and heat-treated material. At room temperature, however, the P/M-processed ternary $Al_{66}Ti_{25}Cr_9$ is brittle.

Table VII: Results of Three-Point Bend Tests on the P/M-Processed Materials

System	Test Temperature	Comments
$Al_{66}Ti_{25}Mn_{6.75}Fe_{2.25}$ + 20% TiB_2	973 K	Brittle
	1000K	Ductile
$Al_{66}Ti_{25}Mn_{4.5}Cr_{4.5}$ + 20% TiB_2	950K	Brittle
	973K	Brittle-Just started to yield
	1023K	Ductile
$Al_{66}Ti_{25}Mn_{4.5}Fe_{4.5}$ + 20% TiB_2	973 K	Brittle
	1023K	Ductile
$Al_{66}Ti_{25}Cr_{4.5}Fe_{4.5}$ + 20% TiB_2	1000K	Brittle
	1023K	Brittle
	1050K	Ductile
Monolithic $Al_{66}Ti_{25}Cr_9$ (coarse grained)	473K	Ductile
	623K	Ductile
	873K	Ductile

F. EFFECT OF HEAT TREATMENT ON COMPRESSION AND BEND PROPERTIES OF $L1_2$ TRIALUMINIDES

Preliminary studies were conducted on some of the ternary and quaternary monolithic forgings to elucidate the role of grain size in influencing compression strength and bend ductility. The as-forged grain size in the monolithic forgings (Fig. 22a-c) is typically in the range 15-20 µm. Two quaternary and one quinary alloy were heat treated at 1473K for 45h in an argon atmosphere. This heat treatment produced grain growth, but to various extents in the three compositions. The maximum growth occurred in the alloy $Al_{66}Ti_{25}Mn_{6.75}Fe_{2.25}$, where the average grain size was ~150µm. This was followed by $Al_{66}Ti_{25}Cr_{4.5}Mn_{4.5}$ where the average grain size was ~100µm whereas the quinary composition exhibited the slowest grain growth with an average grain size of ~70µm. Representative micrographs are shown in Fig. 32a-c.

The grain growth response of the quinary alloy $Al_{66}Ti_{25}Mn_{4.5}Cr_{3.0}Fe_{1.5}$ at 1473K was investigated. After 1 hour at temperature the grain size increases rapidly to ~80µm, but grew slowly for further times at temperature. The variation in grain size with exposure time ($t^{1/2}$) is shown in Fig. 33, and for exposure times varying between 4h and 300h, the grain size remains between 90 and 110µm.

Next, the compressive yield strength-temperature profiles of the heat-treated ternary Mn-based monolithic material and the quinary composition are compared against their as-forged counterparts (Fig. 34). Heat-treatment schedules were selected to increase the grain size of the ternary composition from ~30µm in the as-forged condition to ~200µm following heat treatment. In the case of the quinary composition, grain size increased from ~15-20µm to about 75µm following heat treatment. The heat-treated ternary composition with a grain size of 200µm shows a decrease in strength of ~50 MPa at room temperature and this difference is more or less maintained up to 1100K beyond which, the strength levels begin to converge; a crossover in strength is observed at ~1250K, and above that temperature the coarse grained material is marginally stronger. The effect of grain size on the strength of the quinary alloy is more dramatic. The strength loss by increasing the grain size from 15-20µm to ~75µm is about 100 MPa at 300K, which increases to ~150MPa at 900K before converging at 1273K. It is worth noting that the strengths of the ternary alloy before converging at 1273K. It is worth noting that the strengths of the ternary alloy with a grain size of 200 μm and those of the quinary alloy with a grain size of 75 μm are almost identical in the temperature range 300K - 1100K.

The compound $Al_{66}Ti_{25}Cr_9$ in the as-forged condition is brittle at 300K and 473K in three point bending. Upon heat-treating the bend specimen at ~973K for 24h before testing, limited bend ductility was observed at 473K, although it was still brittle at 300K. Heat-treating at higher temperatures (e.g., 1473K) for 24h lowers the yield strength without an increase in bend ductility. The decrease in yield strength is attributed to grain growth. The effect of grain size on bend ductility, fracture stress and yield stress in such a quasi-brittle condition was evaluated. To this end, a series of heat treatments were identified to obtain a range of grain sizes. The variation of grain size with exposure temperature and time is shown in Fig. 35. Bend specimens were machined from forged $Al_{66}Ti_{25}Cr_9$ and first heat-treated for 24h at 973K. Specimens were then heat-treated appropriately to obtain a range of grain sizes.

The load-versus strain curves from three-point bend tests for the various specimens are provided in Fig. 36. The specimen that was heat-treated at 973K for 1 day failed elastically at a fracture load of 59 kg. In contrast, an additional heat treatment of 10 min at 1373K allowed the specimen to deform plastically (plastic strain of 0.38%), fracturing at a load of 73 kg. A third specimen that was subjected to a heat-treatment of 973K / 24h + 1473K / 10 min deformed plastically to 0.6% strain, fracturing at a load of 73 kg. A similar plastic strain of 0.56% was obtained for a specimen that saw 973K / 1 day + 1473K / 10 min; fracture load was 75 kg. Finally a specimen that experienced a more extensive heat treatment of 973K / 1 day + 1500K / 1 day failed at 79 kg load, although the fracture strain was only 0.24%. It thus becomes clear that in all cases the fracture load is constant (~75 kg) although the plastic strain varies from 0 - 0.6%. This variation in plastic strain with heat treatment may arise due to any or all of the following factors:

(a) grain size effect.
(b) complex environmental-grain boundary interactions.
(c) residual stress effects.
(c) residual high temperature dislocation configurations blocking dislocations generated at low temperatures (i.e. during the test).

The fracture surfaces of these bend specimens were examined in a scanning electron microscope and representative micrographs are included. A low magnification photograph (Fig. 37a) compares the bend fracture surface of the specimen that was heat treated at 973K / 1 day with that of the specimen that saw an additional heat treatment of 1500K / 1 day. From this photograph it is seen that the fracture surface of the latter is more faceted (i.e. coarser) than the former, likely reflecting the effect of a coarse grain size deflecting the crack front at grain boundaries. Higher magnification fracture micrographs are shown in Figures 37b-d. In all cases, fracture propagates by transgranular cleavage. For the coarse-grained material, the fracture surface shows signs of crack deflection at grain boundaries (Fig. 37d).

Optical micrographs of the bend specimens revealed grain sizes which are in reasonable agreement with earlier heat treatment studies. Thus, in Figures 38a-c, grain size changes from ~20µm in the forged + 973K / 1 day heat-treated specimen (Fig. 38a) to ~80µm in the forged + 973K / 1 day + 1423K / 10 min specimen (Fig. 38b) and increases even further in the specimen heat treated at 973K / 1 day + 1500K / 1 day (Fig. 38c).

G. INTERDIFFUSION STUDIES IN THE Al-Ti-Cr/Al-Ti-Mn SYSTEM

Recent studies (35, 48) of the elevated temperature mechanical properties of these $L1_2$ compounds have indicated the occurrence of thermally activated deformation processes. In order to ascribe this behavior to a particular diffusive process, some independent measure of the diffusion rates in these materials is needed. Hence, diffusion couples were set up between two ternary trialuminides $Al_{66}Ti_{25}Mn_9$ and $Al_{67}Ti_{25}Cr_8$ and exposed for extended periods of time in the temperature range 1373K - 1073K. Concentration-distance profiles were obtained and an interdiffusion coefficient, $\tilde{D}$, was calculated for each temperature. Using these $\tilde{D}$ values, activation energies for diffusion were computed and compared against some existing data for activation energy for creep of $Al_{22}Ti_8Fe_3$.

To this end, small cylinders (10mm dia. x 5mm high) of $Al_{66}Ti_{25}Mn_9$ and $Al_{67}Ti_{25}Cr_8$ were machined from an isothermally forged pancake of each composition. The as-forged grain size was ~30µm in each alloy. The specimens were ground and polished and then loaded as a pair (one of each composition) at room temperature in compression to about half the compressive yield strength. The couple was then heated under load to ~1273K, the load being continuously monitored to retain it at approximately half the yield strength at temperature. After an hour at temperature, the furnace was turned off, the couple allowed to cool to room temperature and the load then released. Four such couples were made. These were then exposed to temperatures of 1373K, 1273K, 1173K and 1073K for 384h, 514h, 618h and 1000h respectively. After the high temperature exposure, each couple was electrodischarge machined into a semi-cylinder. The resulting cross section was ground, polished and examined optically and in a scanning electron microscope. Fully quantitative energy dispersive X-ray analysis (EDX) was used to establish the respective concentration-diffusion profiles, an example of which is shown in Figure 39. This figure illustrates the typical behavior, where the Al and Ti levels are essentially constant while a continuous steady interchange between Cr and Mn is observed along the profile. A similar response was observed in each of the remaining three couples confirming that these two compounds formed a continuous solid solution between 1073K and 1373K.

Even though four elements are involved in the diffusion couples, the near absence of concentration gradients for Al and Ti and the steady replacement of Mn for Cr along the profiles (Fig. 39) indicate that diffusion between $Al_{66}Ti_{25}Mn_9$ and $Al_{67}Ti_{25}Cr_8$ can be treated as a pseudobinary system. Hence the Matano analysis (49) was used in conjunction with the normalized Mn concentration - distance profiles (Fig. 40) to determine the chemical diffusion coefficient, $\tilde{D}$, for each temperature as a function of composition. Since the Matano analysis requires measurements of the area under the portion of the curve under consideration and the slope at the specific composition of interest, the errors in calculating $\tilde{D}$ are a maximum where the concentration, C/C_0, approaches either 0 or 1. The variation in $\tilde{D}$ with composition at each of the four temperatures is shown in Figure 41. At the two intermediate temperatures (1173K and 1273K), a minimum in $\tilde{D}$ is observed at $C/C_0 = 0.5$.

The variation in $\tilde{D}$ with temperature for $C/C_0 = 0.3$, 0.5 and 0.7 is shown in Figure 42. Presumably, the 1373K to 1173K data are indicative of a volume controlled diffusion and the deviation from linearity at 1073K is the result of a different process such as grain boundary diffusion. Alternatively, this deviation might, at least in part be due to the welding procedure that was used to construct the couple. With an average diffusion coefficient of ~5×10^{-12} cm^2/s (Figure 41), an anneal at 1273K for an hour would result in an approximately 10 µm wide concentration zone which is about 25 % of the width found after the 1000h exposure at 1073K (Figure 40).

The interdiffusion data between 1373K and 1173K for each normalized Mn concentration shown in Figure 42 were fitted to $\tilde{D} = \tilde{D}_0 \exp(-\tilde{Q})/RT$ where $\tilde{D}_0$ is a constant, $\tilde{Q}$ is the activation energy for diffusion, R is the universal gas constant and T is the absolute temperature. The results of these fits are given in Table VIII. While the rates of diffusion are essentially equal at 1373K (Figure 42), the 1173K values are strong functions of composition. This behavior is reflected in the activation energies (Table VIII) where a spread of 90 kJ/mol can be seen.

A direct comparison of the activation energies for diffusion and elevated temperature deformation is not presently possible since activation energy for creep for either $Al_{66}Ti_{25}Mn_9$ or $Al_{67}Ti_{25}Cr_8$ is not available; creep data are however available for $Al_{22}Ti_8Fe_3$-based systems (35, 48). The Fe-based compound forms a continuous solid solution with both the Cr- and Mn-based compounds and it is likely that diffusion in $Al_{22}Ti_8Fe_3$ is similar to that in either $Al_{66}Ti_{25}Mn_9$ or $Al_{67}Ti_{25}Cr_8$. In the Fe-based compounds, the activation energies for 1100K-1200K deformation ranged from 310 kJ/mol to 360 kJ/mol which are in general agreement with those obtained for interdiffusion in this study. Therefore, it appears that volume diffusion controls creep in these $L1_2$ compounds at the temperatures of interest.

Table VIII: Activation Energy and the Pre-exponent ($\tilde{D}_0$) for Mn (Cr) Interdiffusion between $Al_{66}Ti_{25}Mn_9$ and $Al_{67}Ti_{25}Cr_8$ from 1373K - 1173K.

Relative Mn concentration	$\tilde{D}_0$ (cm^2/s)	$\tilde{Q}$ (kJ/mol)
0.3	0.307	260
0.5	589.1	348
0.7	13.51	305

H. CONTINUOUS METAL WIRE REINFORCEMENT - FEASIBILITY STUDIES

A possible means of simultaneously enhancing creep resistance and ambient temperature damage tolerance involves the incorporation of long refractory metal wires in these trialuminides. Potential fiber/matrix combinations must exhibit minimal CTE mismatch and good chemical compatibility (i.e. minimal interfacial reaction and chemical stability). To identify such systems, typical CTE values as a function of temperature are shown for the matrix trialuminides and for potential reinforcements (Table IX).

Table IX: A Comparison of the CTE of the $L1_2$ Trialuminides with those of Potential Metallic Reinforcements (Wire form).

Material		Temperature (K)				
a)	Matrix	300	573	773	973	1200
	$Al_{66}Ti_{25}Mn_9$	13.8	14.9	16.5	17.1	17.1
	$Al_{22}Ti_8Fe_3$ + 2at.%Nb	11.5	13.1	13.9	14.7	17.0
	$Al_{22}Ti_8Fe_3$ + 2at.%Nb + 20 vol.% TiB_2	9.8	11.4	12.3	13.5	14.3
b)	Reinforcements					
	W	4.5	-----	4.6	----	4.6
	Nb	7.2	-----	7.5	----	7.8
	Ta	6.5	-----	6.6	----	----
	TZM	5.2	-----	5.7	----	5.8
	Ti	8.8	-----	9.4	----	9.9
	Fe	12.2	-----	14.0	----	14.8
	S. S. (304)	16	-----	17.0	----	18.0

A preliminary screening study was undertaken and included three matrix compositions ($Al_{66}Ti_{25}Mn_9$, $Al_{67}Ti_{25}Cr_8$ and $Al_{67}Ti_{25}Cr_8$ + 20 vol.% TiB_2). Compacts containing the wires listed in Table IX were hot pressed (~1360K; 125 MPa) at the NASA Lewis Research Center and examined for interfacial reactions and cracking from CTE mismatch.In all cases, except for the TZM/$Al_{67}Ti_{25}Cr_8$ and W/$Al_{67}Ti_{25}Cr_8$ combinations radial matrix cracking or circumferential cracking at the interface was observed. These findings are unusual because both TZM and W exhibit a large CTE mismatch relative to these trialuminides. In addition, a significant reaction zone was observed for the Nb, Ta, Fe, Stainless steel and Ti wires when these were incorporated in any of the three matrices whereas the W and TZM wires exhibit little or no reaction with monolithic $Al_{67}Ti_{25}Cr_8$. Representative micrographs of monolithic $Al_{67}Ti_{25}Cr_8$ containing Nb, Ta, W and stainless steel wires are shown in Figs. 43a-d

To confirm these findings, these experiments were repeated at Martin Marietta Laboratories. Two different diameter 'W' wires were studied (0.1016 mm and 0.2032 mm) and TZM was also examined. In each hot-press run, an assembly of 9 wires was used, the spacing between the nine segments being sufficiently large that there was no overlapping stress effects. Hot-pressing was performed in a graphite die using 21 MPa pressure and at a temperature of 1473 K. A cross section of each of the three hot-pressed compact was examined optically for possible interfacial reaction and/or cracking due to CTE mismatch.

In the case of the $Al_{66}Ti_{25}Cr_9$/TZM composite, for all the 9 fibers examined, a significant reaction zone was present and radial cracks were observed. The significantly larger reaction zone observed in the present study relative to the observations on the specimen pressed at NASA Lewis Research Center is likely a consequence of the higher hot pressing temperature used in the present study. In the case of the W reinforced trialuminide, a total of 18 fibers were examined, 9 in each of two compacts. Not a single case was identified where a reaction zone or an interfacial crack was present, thus reproducing earlier observations. Representative micrographs are shown in Figs. 44 and 45. Subsequently, a gold film was sputtered on the surface where the fiber cross sections were exposed and both these compacts were thermally cycled between 1123 K and room temperature in an argon atmosphere. The compacts were held at 1123 K for 15 minutes, withdrawn to the cold zone of the tube furnace and held for 15 minutes and then reintroduced to the hot zone for another 15 minutes. This cycle was repeated 10 times. The gold coated section was then polished and the cross section was optically examined for any cracks that may have formed due to thermal cycling. Representative micrographs are shown in Fig. 46 and clearly there appears to be no crack at the interface. Explanation for this unexpected behavior is speculative at present. One possible reason is that the fiber volume fraction is sufficiently low that the matrix does not experience significant constraint from adjacent fibers and is in this condition, able to absorb the thermal mismatch stresses without cracking. Subsequently, a compact of $Al_{66}Ti_{25}Cr_9$ was hot-pressed which contained a local region within it where a fiber array of 5 x 5 was assembled with inter-fiber spacing respresentative of ~8-10 vol%. During hot-pressing this assembly underwent some distortion but nevertheless, sufficiently small fiber spacings were obtained. A representative micrograph of the hot pressed material is shown in Fig. 47. Fine cracks are present that connect from one fiber to another, although in regions of the compact away from the fiber array, such cracks were not observed. This suggests that when the fibers are spaced sufficiently close, then the mismatch stresses cannot be absorbed by the matrix without cracking.

Thus, $Al_{67}Ti_{25}Cr_8$ is compatible with a low volume fraction of tungsten wires, but when larger volume fractions are incorporated, matrix cracking between closely spaced fibers is observed. A fine powder size (≤44μm) was used in these studies along with 0.2 mm diameter tungsten wires. It was earlier shown for $Al_{66}Ti_{25}Cr_9$ that using ≤63μm powder size and a good vacuum during hot pressing it is possible to produce a larger grain size material than was typically obtained by P/M processing. This in turn implies yield strengths comparable to the ingot metallurgy processed counterpart and hence possibly some low temperature ductility (this was confirmed by bend tests -- see Table VII). Thus by using a larger powder size and a finer diameter W wire (0.1 mm), there may be a better chance of producing a crack-free composite, particularly at low volume fractions of reinforcements. An ingot of the Cr-based matrix was cast, homogenized and pulverized in an attrition mill. Tungsten wires were obtained and cut into segments 5-10 mm in length. and blended with the powder and hot pressed to produce a compact cotaining 5 vol.% reinforcement. The object of this experiment was to verify that a crack-free composite can be produced with such metal fiber reinforcement and that it can provide enhanced damage tolerance relative to its monolithic counterpart. Representative optical micrographs of the hot-pressed composite are provided in Figures 48a,b. Although no interfacial reactions are apparent, fine interconnected cracks arising from CTE mismatch between the W wires and the matrix are seen across the entire compact, rendering it vitually useless. No further work was done in this area.

Other fibers examined include stainless steel wires, with and without a preoxidized coating, two different Ni-base superalloys and chromel and alumel wires. In all cases, significant reaction occurred between the matrix and the fibers. Attempts to incorporate W fibers in $Al_{63}Ti_{28}Fe_{8.75}$ and its 20 vol.% TiB_2 containing counterpart were unsuccessful. Extensive cracking of the hot pressed compact precluded even microstructural characterization.

I. NEAR-NET SHAPE FORGING DEMONSTRATION

In order to evaluate the fabricability of such compounds, a first attempt was made to forge a net-shape part from a cast and homogenized billet of ternary $Al_{66}Ti_{25}Mn_9$. This part was forged at the Ladish Co., Inc. in Wisconsin. The top and bottom views of the resulting forging are shown in Figs. 49a,b. Forging temperature was 1450K, and this may have been too high and likely caused the edge cracking observed in Figure 49a. Press tonnage capacity precluded using a lower temperature. The cracks observed in the hub section (Fig. 49b) occurred due to CTE mismatch during cooling the part from the forging temperature because of the inability to eject the Mo punch from the hub. It must be emphasized however, that for a first attempt, the observed response to hot forging is encouraging

VI. SUMMARY OF RESULTS

1. Uniaxial tensile deformation of forged $Al_{67}Ti_{25}Cr_8$.

- At room temperature, failure occurred by transgranular cleavage with no accompanying ductility.

- At 623K, ductility was small -- 0.2% -- but finite, and the associated tensile yield strength was ~375 MPa. Fracture still occurred by transgranular cleavage.

- At 773K, ductility fell to zero, although fracture strength was much lower than that obtained at 623K. Fracture mode remained transgranular cleavage.

- Covering the gage section of a specimen with a protective gold film and testing at 773K resulted in 1% ductility, although the yield strength was similar to the fracture stress obtained for the specimen without the protective coating. The specimen with the protective gold film exhibited predominantly transgranular cleavage, although isolated events of intergranular failure were observed.

- At 923K, the strength was similar to that obtained at 773K, although ductility increased to ~1.3% in air. Fracture propagated by cleavage and intergranularly.

- At 1073K, a mild decrease in strength was accompanied by a dramatic increase in ductility to ~19%, with fracture propagating intergranularly. Serrated grain boundaries were present and recovery and recrystallization (likely dynamic) were observed.

2. Ingot metallurgy processed quaternary and quinary alloys.

- The ternary $L1_2$ trialuminides, $Al_{66}Ti_{25}Mn_9$, $Al_{67}Ti_{25}Cr_8$ and $Al_{22}Ti_8Fe_3$ exhibit continuous solubility in each other.

- A hardness minimum is observed at quaternary compositions corresponding to $Al_{66}Ti_{25}Mn_{6.75}Fe_{2.25}$ and $Al_{66}Ti_{25}Cr_{4.5}Mn_{4.5}$ in the respective quaternary systems although subsequent tensile studies of these quaternary compositions did not reveal any ductility improvement over the ternary $Al_{66}Ti_{25}Mn_9$; in fact the quaternary compounds were worse--this is an example that shows hardness indentations are not reliable indicators of tensile ductility in these materials.

- The quaternary Cr-Mn composition does not indicate any strength advantage (in compression) over its ternary counterparts.

- The continuous replacement of Mn with Fe enhances the compressive strength of the quaternary compound over the ternary $Al_{66}Ti_{25}Mn_9$.

- The superior strength of the quinary alloy appears to be derived from the fine grain size in the forging, because after a heat-treatment which coarsens the grains, the strength drops significantly and is similar to the ternary $Al_{66}Ti_{25}Mn_9$.

- In uniaxial tension, all the quaternary and the quinary compositions were disappointing; at low and intermediate (< 800 K) temperatures they failed elastically at low stresses and exhibited only limited plasticity even at 1073K. Whether this response is intrinsic to these compositions or is a consequence of the presence of undesirable second phases/forging defects/residual stresses remains to be determined.

- Interdiffusion studies using $Al_{67}Ti_{25}Cr_8$/$Al_{66}Ti_{25}Mn_9$ diffusion couples confirmed the existence of a continuous solid solution and provided diffusion coefficients as a function of composition and temperature.

- These diffusion studies also provided activation energy values which are in reasonable agreement with previously obtained activation energy for compressive creep of $Al_{22}Ti_8Fe_3$, suggesting that volume diffusion controls creep response in these materials.

3. Powder metallurgy processed ternary, quaternary and quinary trialuminides-based particulate composites.

- It was not possible to obtain a single phase ternary $L1_2$ trialuminide matrix using the P/M XD process; rather a supersaturated single phase matrix containing TiB_2 particles is obtained in the hot pressed condition and during elevated temperature mechanical testing, the matrix decomposes into the $L1_2$ structure and Al_2Ti.

- The addition of the TiB_2 particles appears to have no obvious advantage for elevated temperature strength and will likely worsen oxidation resistance.

- The ductile to brittle transition temperature is significantly higher for the TiB_2-containing composite relative to the monolithic material; whether this is due to the particles themselves, due to grain refinement, due to shift in matrix composition or due to some boron in solid solution is not clear.

4. Feasibility studies for metal wire reinforcements.

- Most of the refractory metal wires examined exhibit an interfacial reaction with the Cr- and Mn-based trialuminides. They also exhibit interfacial cracking as a consequence of CTE mismatch. Whether a radial crack occurs in the matrix or a circumferential crack is present depends on the CTE of the fiber being lower or higher than that of the matrix.

- Although a large CTE mismatch exists between W and $Al_{67}Ti_{25}Cr_8$, no interfacial cracks were observed after hot pressing and after 10 thermal cycles between 1123 K and room temperature provided that the volume fraction of fibers were sufficiently low that interactive stresses from adjacent fibers were low; however, when the volume fraction was increased to 7-8%, matrix cracks were observed in the hot pressed material. No interfacial reaction was observed for this matrix/refractory metal wire combination.

VII. REFERENCES

1. E.P. George, D.P. Pope, C.L. Fu and J.H. Schneibel, ISIJ International, 31, 1063, (1991).

2. K.S. Kumar, S.A. Brown, K.A. Montoya, J.D. Whittenberger and M.S. DiPietro, in Intermetallic Compounds. Proceedings of the sixth JIM international symposium on intermetallics, (ed: O. Izumi), Sendai, Japan, p. 667, (1991).

3. K.S. Kumar and S.A. Brown, Philos. Mag., accepted for publication.

4. K.S. Kumar and S.A. Brown, Acta Metall. et Mater., submitted for publication.

5. K. Hirukawa, H. Mabuchi and Y. Nakayama, Scripta Metall. et Mater.,25, 727, (1991).

6. L.J. Parfitt, J.L. Smialek, J.P. Nic and D.E. Mikkola, Scripta Metall. et Mater., 25, 1211, (1991).

7. I. Jung, M. Rudy and G. Sauthoff, in High Temperature Ordered Intermetallic Alloys II, vol. 81, (ed: N.S. Stoloff, C.C. Koch, C.T. Liu and O. Izumi), MRS, Pittsburgh, PA., 263, (1987).

8. W.O. Powers, J.A. Wert, and C.D. Turner, Philos. Mag. A., 60, 227, (1989).

9. C.D. Turner, W.O. Powers, and J.A. West, Acta Metall., 37, 2635, (1989).

10. V.K. Vasudevan, R. Wheeler, and H.L. Fraser, in High Temperature Ordered Intermetallic Alloys III (editors: C.T. Liu, A.I. Taub, N.S. Stoloff and C.C. Koch), Vol. 133, Materials Research Society, Pittsburgh, PA, 705 (1989).

11. M.J. Marcinkowski, Phys. Stat. Sol. (a), 90, 621, (1985).

12. Z.L. Wu, D.P. Pope and V. Vitek, Scripta Metall. et Mater., 24, 2191 (1990).

13. K.S. Kumar and R.A. Herring, Scripta Metall. et Mater., 24, 1713 (1990).

14. H. Inui, D.E. Luzzi, W.D. Porter, D.P. Pope, V. Vitek, and M. Yamaguchi, Philos. Mag. A, accepted for publication.

15. Hu Gengxiang, Chen Shipu, Wu Xiaohua and Chen Xiaofu, J. Mater. Res., 6, 957 (1991).

16. Y. Liu, T. Takasugi, O. Izumi and T. Takahashi, Acta Metall., 36, 2959 (1988).

17. Y. Liu, T. Takasugi, O. Izumi and T. Takahashi, Philos. Mag. A, 59, 437 (1989).

18. Y. Liu, T. Takasugi, O. Izumi and T. Takahashi, Philos. Mag. A, 59, 423 (1989).

19. D.G. Morris and R. Lerf, in Proc. of Int. Symp. on Intermetallic Compounds-Structure and Mechanical Properties-(JIMIS-6), June 17-20, 1991, Sendai, Japan (ed: Osamu Izumi) Japan Institute of Metals, Sendai, Japan, 1991, p. 45.

20. D.G. Morris, Scripa Metall. et Mater., 25, 713(1991).

21. E.P. George, J.A. Horton, W.D. Porter and J.H. Schneibel, J. Mater. Res., 5, 1639 (1990).

22. D.E. Mikkola, J.P. Nic, S. Zhang and W.W. Milligan, ISIJ International, 31, 1076 (1991).

23. S.R. Nishitani, K. Masaki, Y. Shirai and M. Yamaguchi, Scripta Metall. et Mater., 25, 1921 (1991).

24. R. Lerf and D.G. Morris, Acta Metall. et Mater., 39, 2419 (1991).

25. W.D. Porter, K. Hisatsune, C.J. Sparks, W.C. Oliver, and A. Dhere, in High Temperature Ordered Intermetallic Alloys III, vol. 133, (ed: C.T. Liu, A.I. Taub, N.S. Stoloff and C.C. Koch), MRS, Pittsburgh, PA, 1989, p. 657.

26. P.R. Munroe and I. Baker, J. Mater. Res., 6, 943 (1991).

27. E.P. George and C.T. Liu in Alloy Phase Stability and Design (editors: G.M. Stocks, D.P. Pope and A.F. Giamei), Vol. 186, Materials Research Society, Pittsburgh, PA, 1990.

28. C.L. Fu, J. Mater. Res., 5, 1990, p. 971.

32. A.R.C. Westwood, Metall. Trans. A, 19A, 749, (1988).

33. K. Sharvan Kumar, ISIJ International, 31, 1249, (1991)

34. K.S. Kumar and J.D. Whittenberger, Matls. Sci. and Tech., -- accepted for publication.

35. M.S. DiPietro, K.S. Kumar and J.D. Whittenberger, J. Mater. Res., 6, 530 (1991).

36. G.R. Edwards, T.R. McNelley, and O.D. Sherby, Philos. Mag., 32, 1245, (1975).

37. K.S. Kumar, M.S. DiPietro, S.A. Brown and J.D. Whittenberger, "Low-Density, High-Strength Intermetallic Matrix Composites by XD™ Synthesis, NASA Technical Memorandum 103724, January 1991.

38. J.D. Whittenberger, Mater. Sci. Eng., 57, 77, (1983).

39. A.W. Mullendore and N.J. Grant, in Structural Processes in Creep, Special Report No. 70, The Iron and Steel Institute, London, 44, (1961).

40. J.L. Lytton, C.R. Barrett and O.D. Sherby, Trans. TMS-AIME, 233, 1399, (1965).

41. I. Baker, D.V. Viens and E.M. Schulson, Scripta Metall., 18, 237, (1984).

42. G. Gottstein and W. Kim, in High Temperature Ordered Intermetallic Alloys III, vol. 133 (ed: C.T. Liu, A.I. Taub, N.S. Stoloff and C.C. Koch), MRS, Pittsburgh, PA, 511, (1989).

43. E.M. Schulson, Metall. Trans. A, 9, 527 (1978).

44. M.H. Yoo and C.L. Fu, ISIJ International, 31, 1049 (1991).

45. S.A. Brown, K.S. Kumar and J.D. Whittenberger, Scripta Metall. et Mater., 24, 2001, (1990).

46. L. Potez, A. Loiseau, S. Naka and G. Lapasset, J. of Matls. Res., submitted for publication.

47. T. Suzuki, Y. Oya and D.M. Wee, Acta Metall. 28, 301, (1980).

48. J.D. Whittenberger, K.S. Kumar, S. Brown, M.S. DiPietro and S.C. Farmer, in Lightweight Alloys for Aerospace II, (eds: E.W. Lee and N.J. Kim) TMS, Warrendale PA, 1991, p. 327.

49. P.G. Shewmon, in Diffusion in Solids, McGraw-Hill Series in Materials Science and Engineering, 29 (1963).

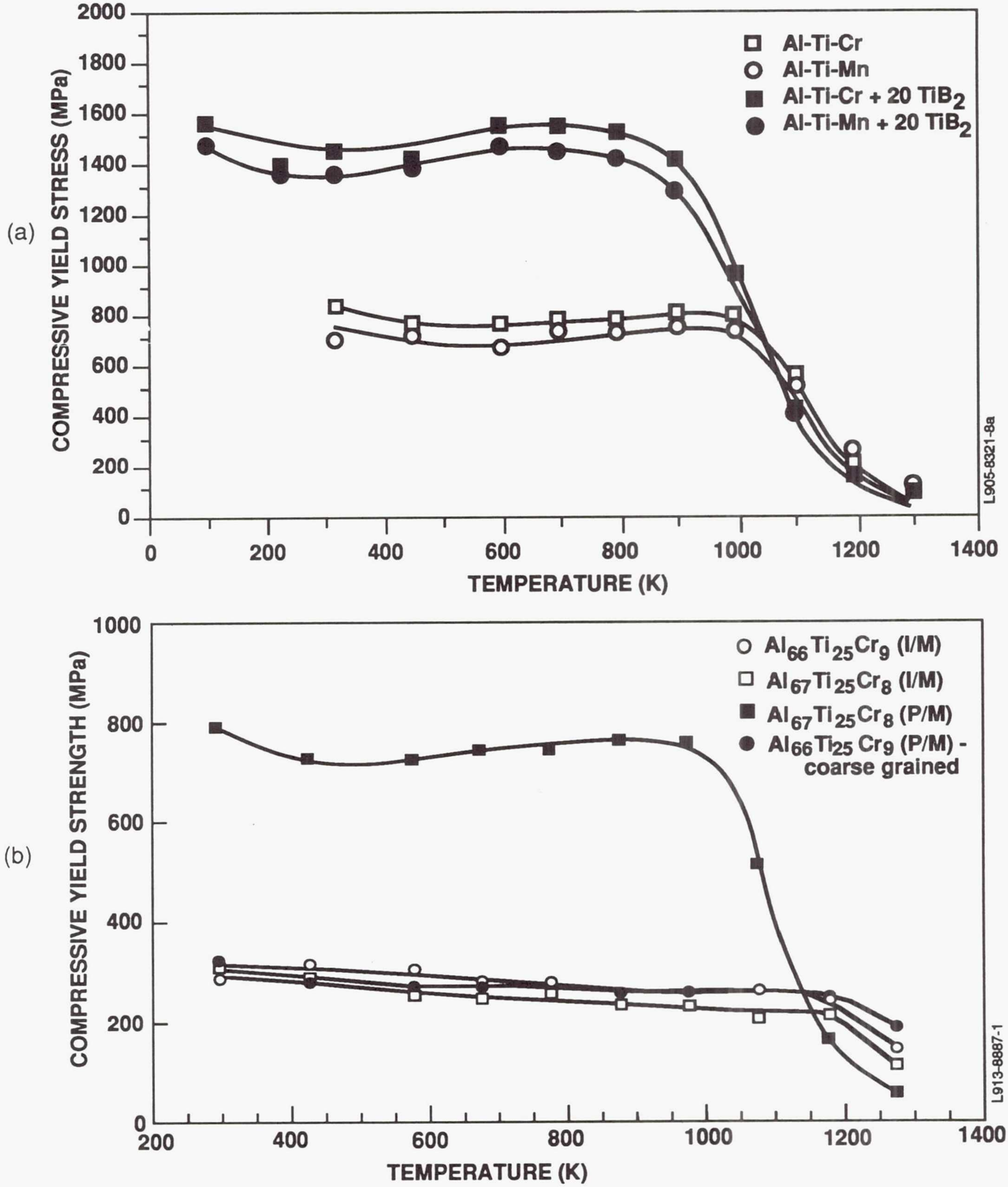

Figure 1. Compressive yield strength versus temperature for (a) hot-pressed and HIPed $Al_{67}Ti_{25}Cr_8$ and $Al_{66}Ti_{25}Mn_9$ with and without 20 vol.% TiB_2 and (b) I/M processed Cr-based monolithic trialuminides compared against both a fine grained and a coarse grained P/M counterpart.

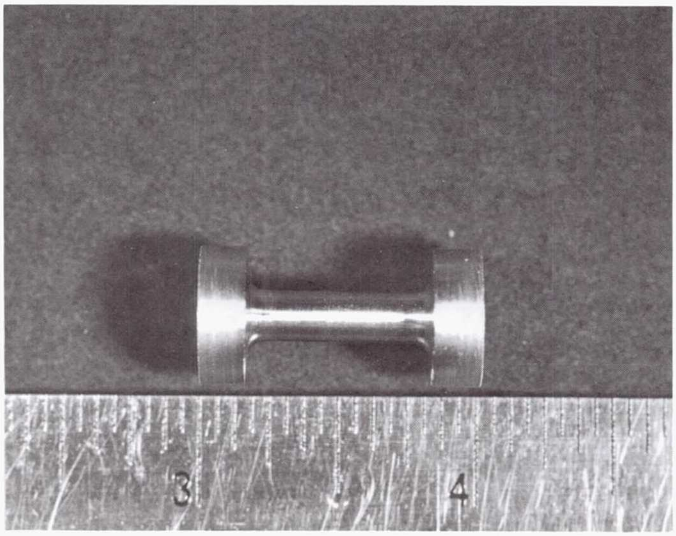

Figure 2. Low-magnification photograph of the buttonhead tensile specimen.

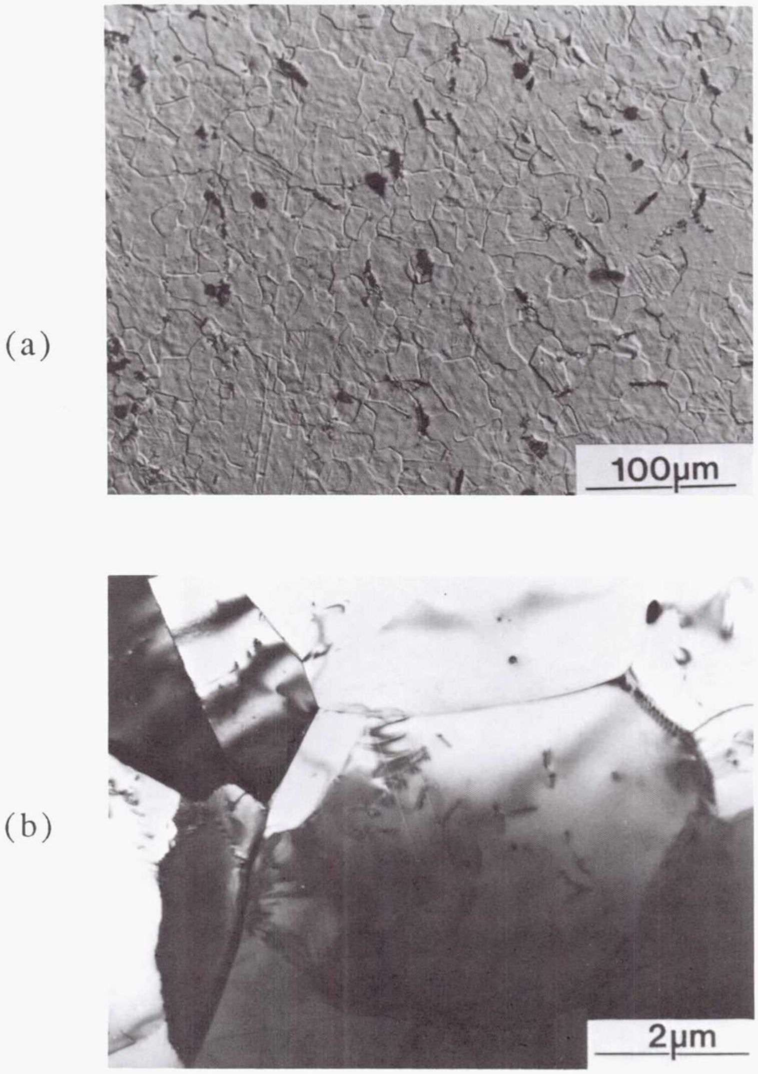

Figure 3. Microstructure of $Al_{67}Ti_{25}Cr_8$ in the forged condition: (a) grain size and (b) subgrain structure.

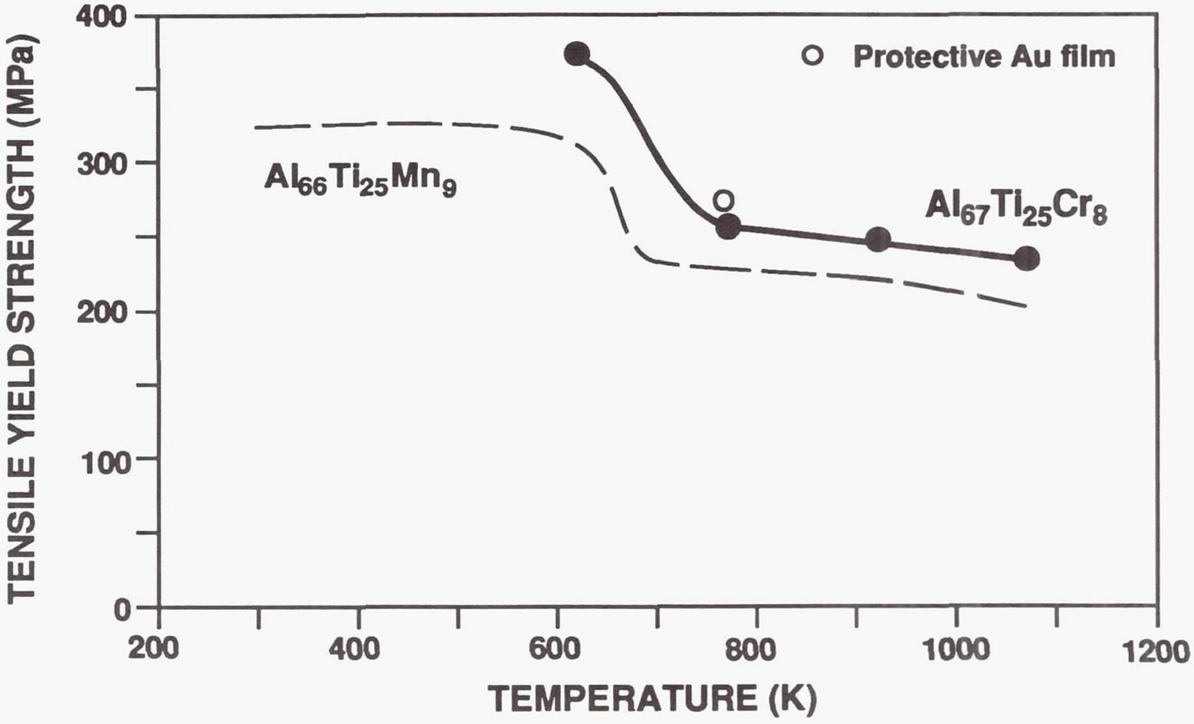

Figure 4. Variation in the tensile yield strength of $Al_{67}Ti_{25}Cr_8$ with test temperature.

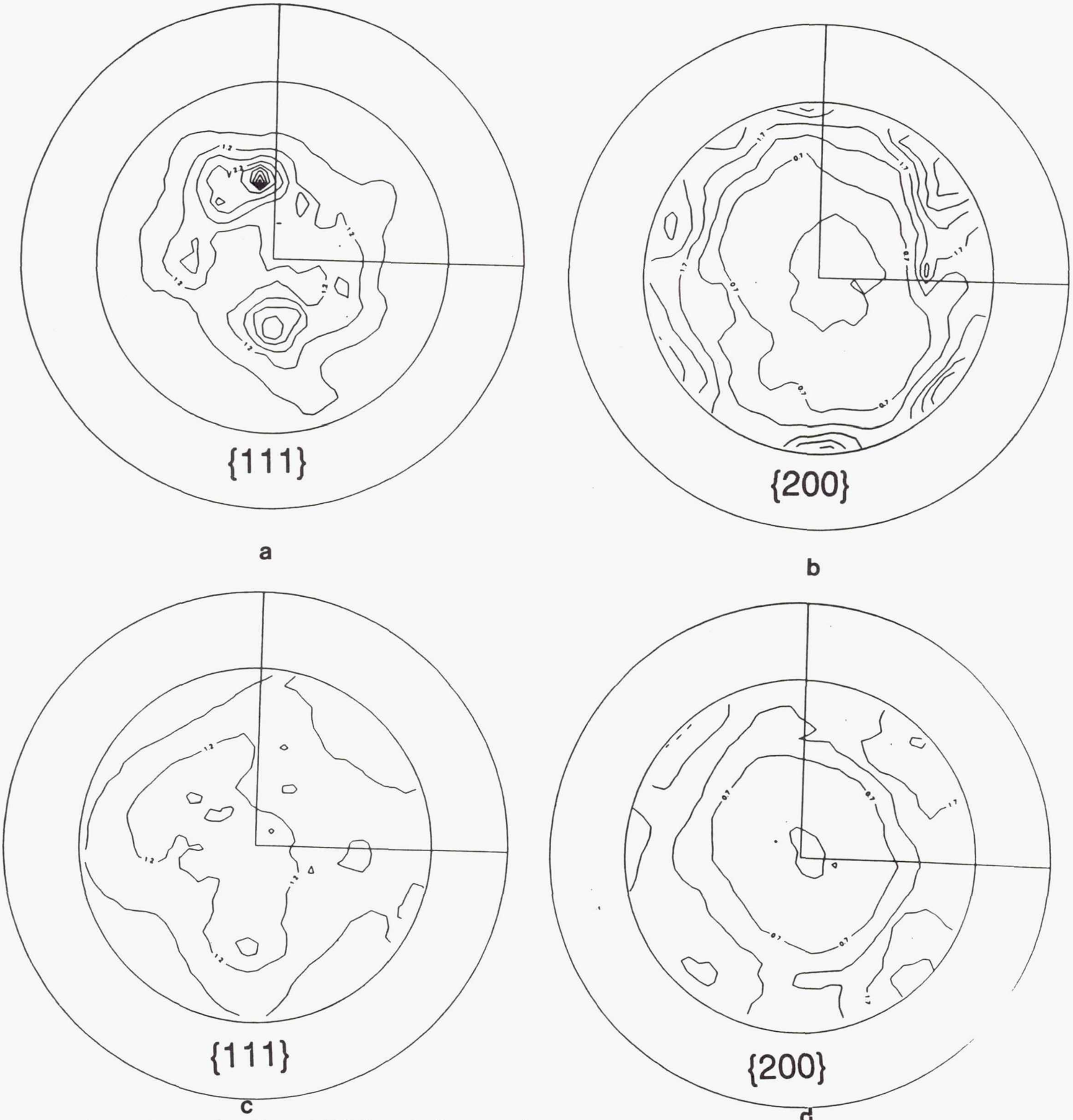

Figure 5. {111} and {200} pole figures showing the absence of strong texture in $Al_{67}Ti_{25}Cr_8$ in (a,b) specimen in the forging plane and (c,d) specimen perpendicular to the forging plane.

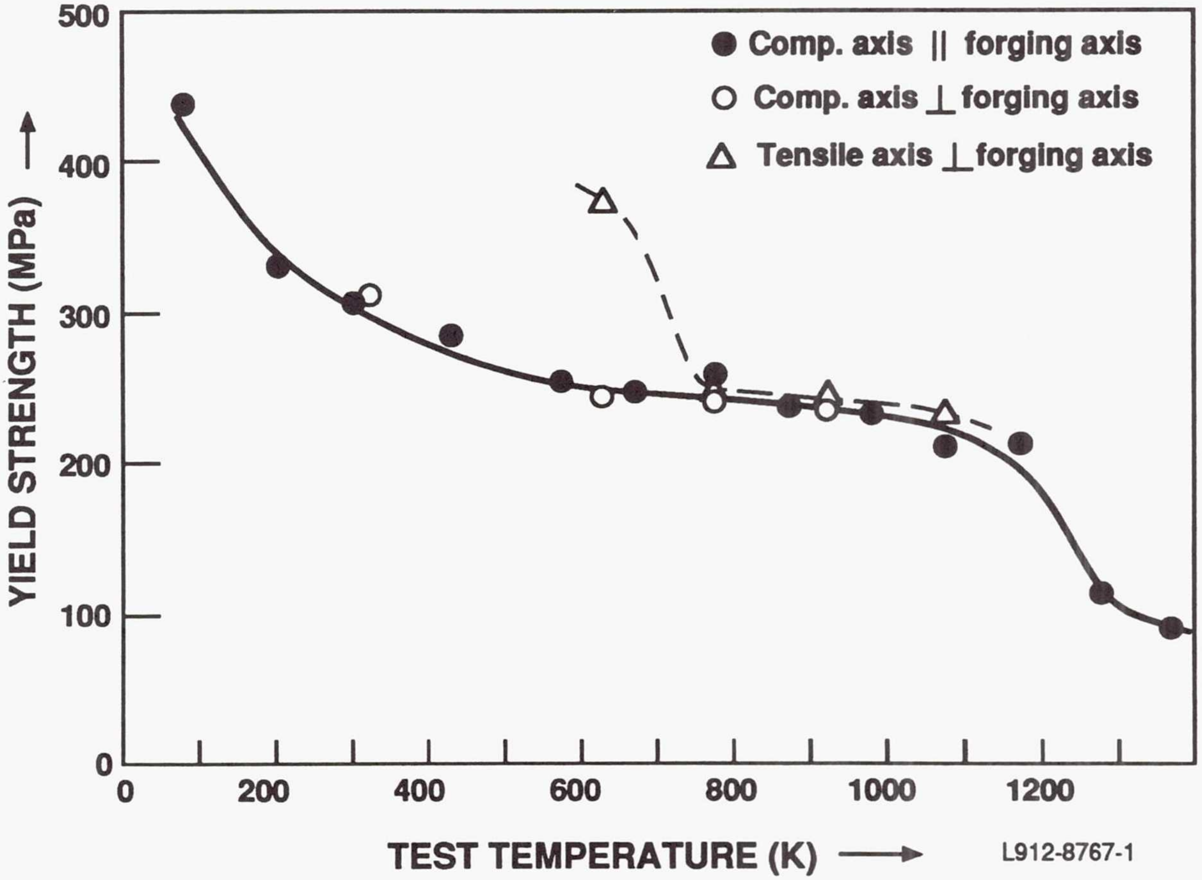

Figure 6. A comparison of tensile and compressive yield strengths of $Al_{67}Ti_{25}Cr_8$ with test temperature.

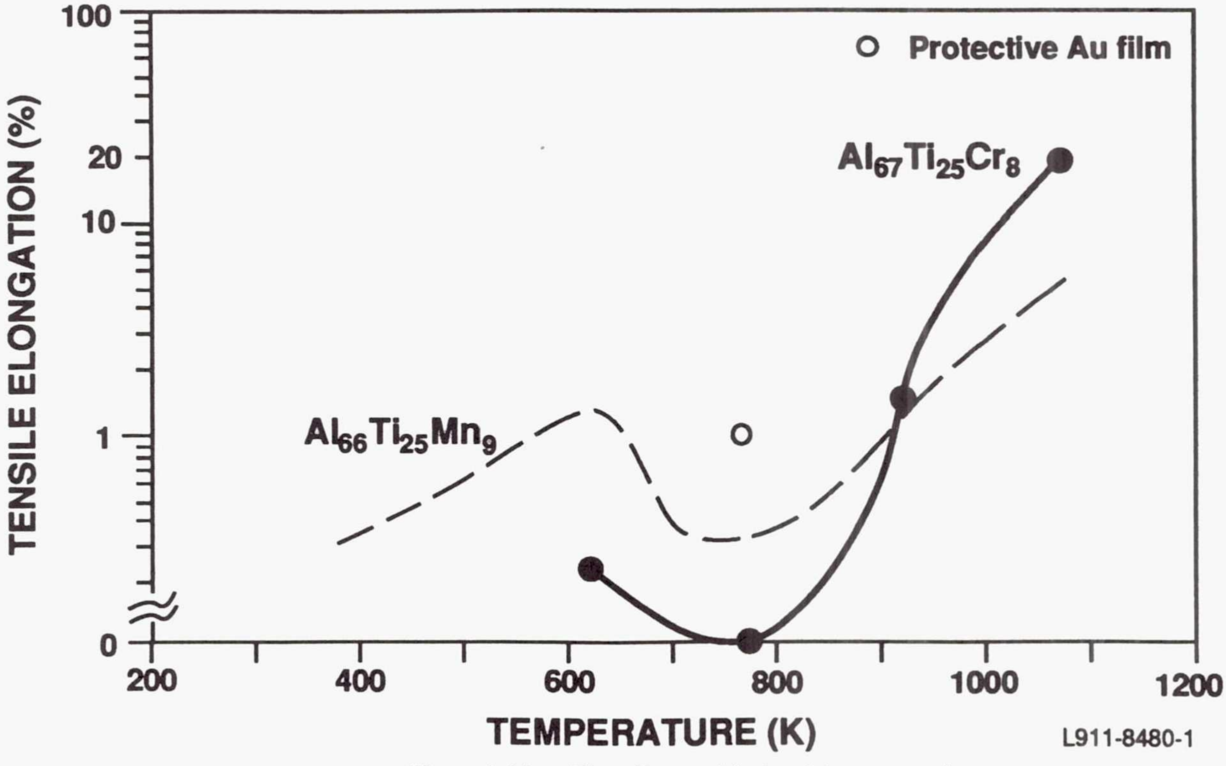

Figure 7. Variation in the ductility of $Al_{67}Ti_{25}Cr_8$ with test temperature.

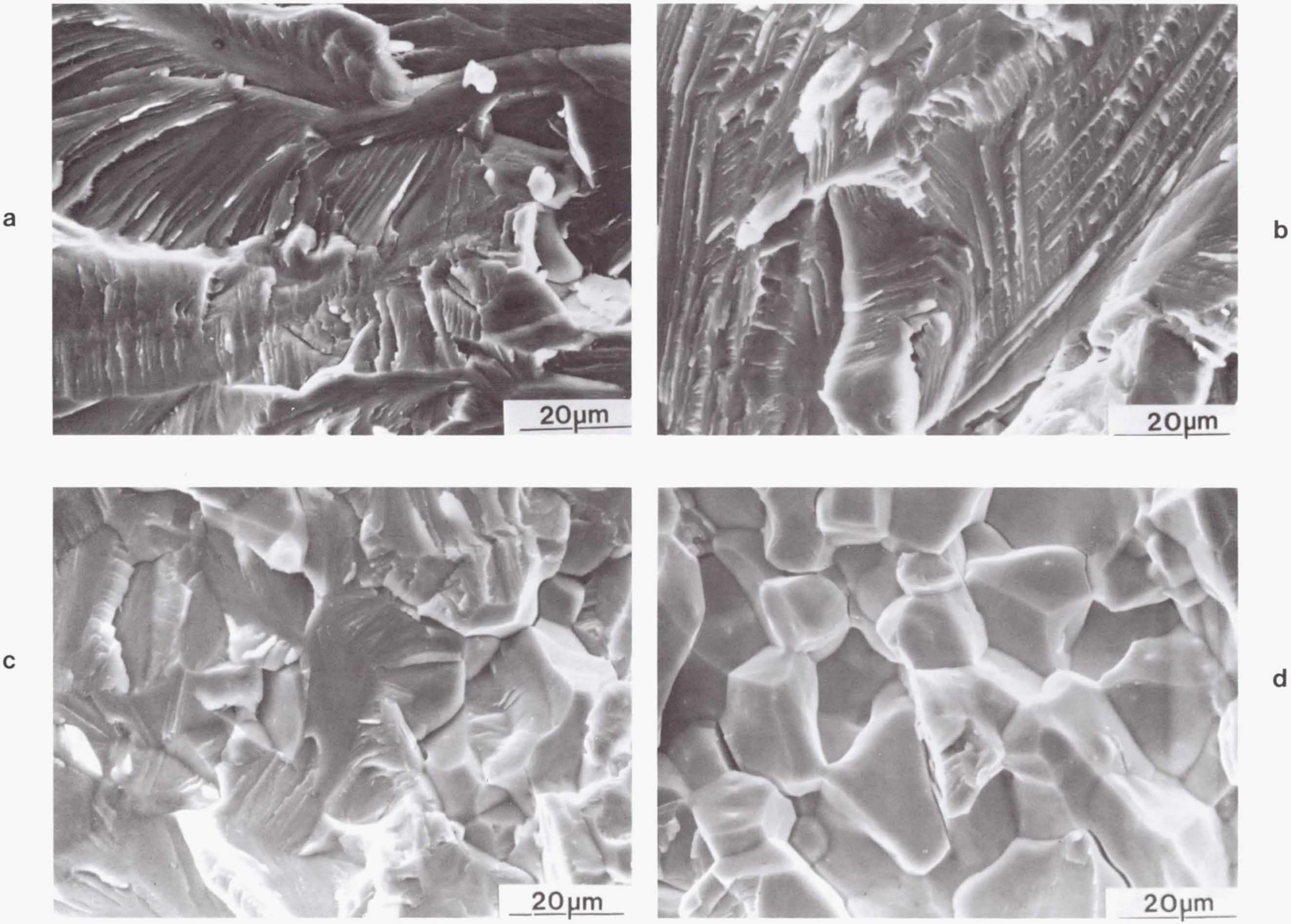

Figure 8. Representative micrographs of tensile specimen fracture surfaces: (a) transgranular cleavage at 623K, (b) transgranular cleavage at 773K, and a mixture of (c) transgranular cleavage and (d) intergranular failure in a specimen tested at 923K.

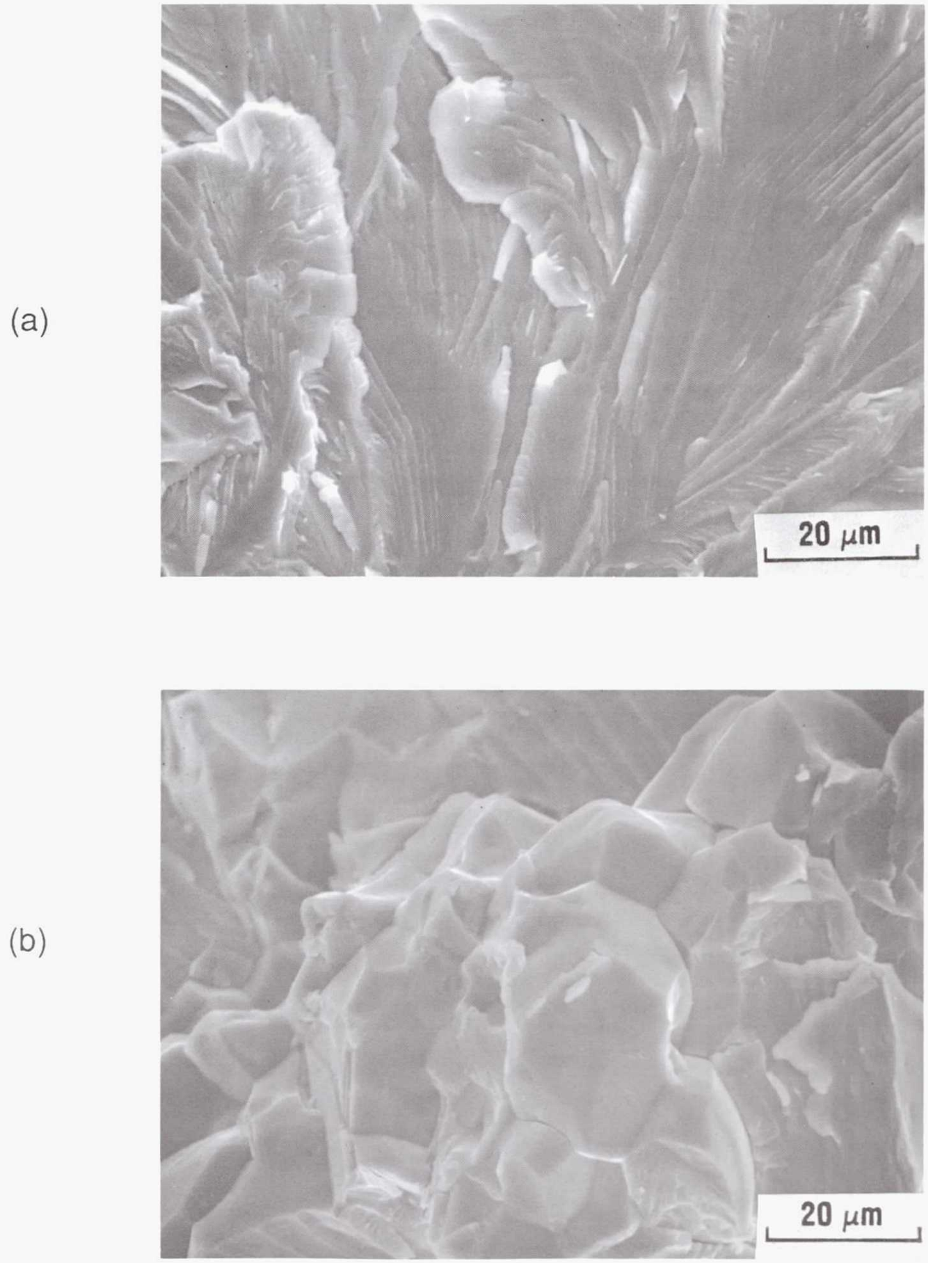

Figure 9. Fracture surface of the specimen tested at 773K with a Au film on the gage section: (a) predominantly transgranular cleavage and (b) occasional intergranular failure.

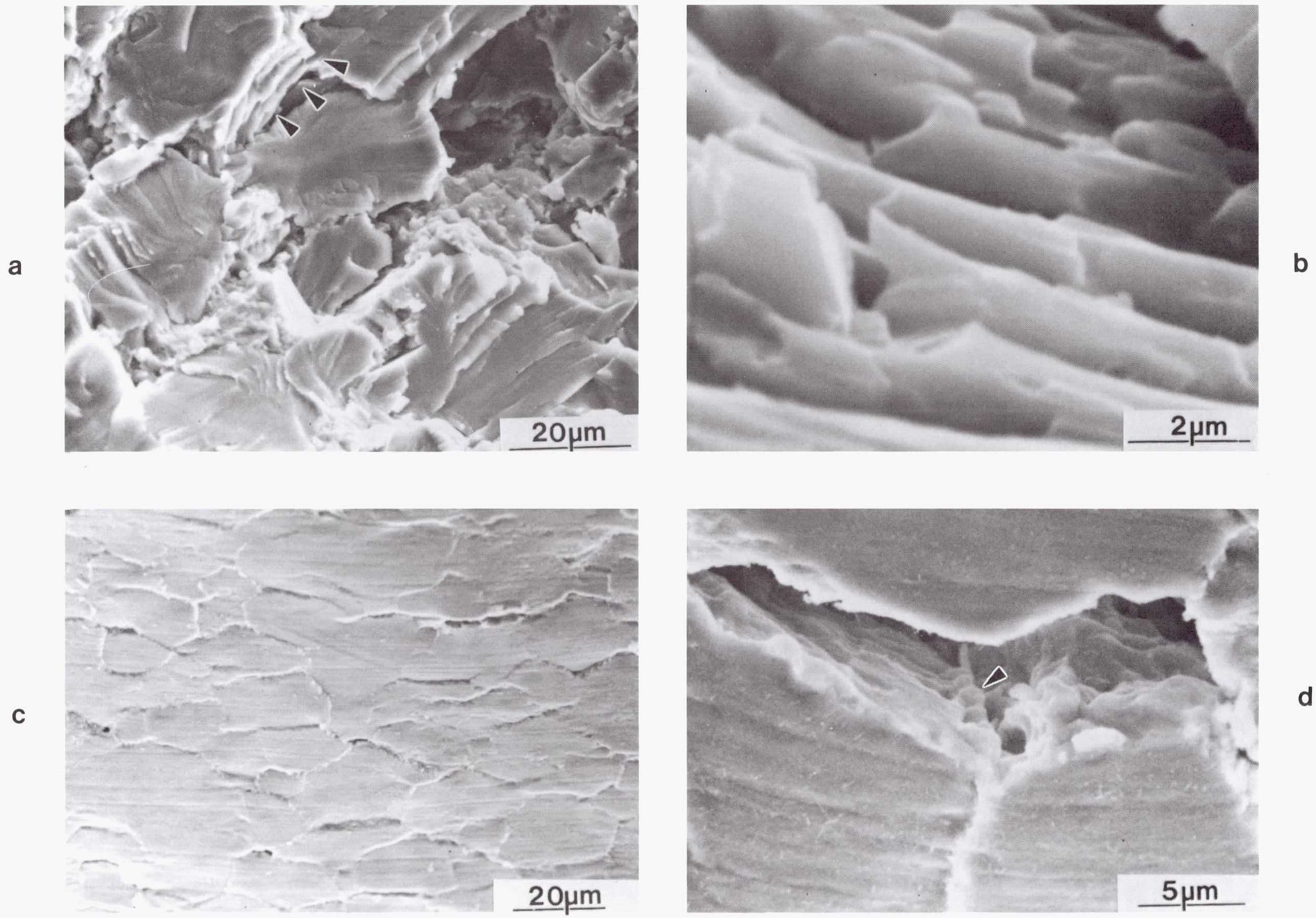

Figure 10. Representative micrographs of the fracture surface and gage section of a tensile specimen tested at 1073K: (a) intergranular failure mixed with cleavage, (b) "delamination" at grain boundaries, (c) intergranular cracking on gage surface and (d) grain boundary triple-point cracking.

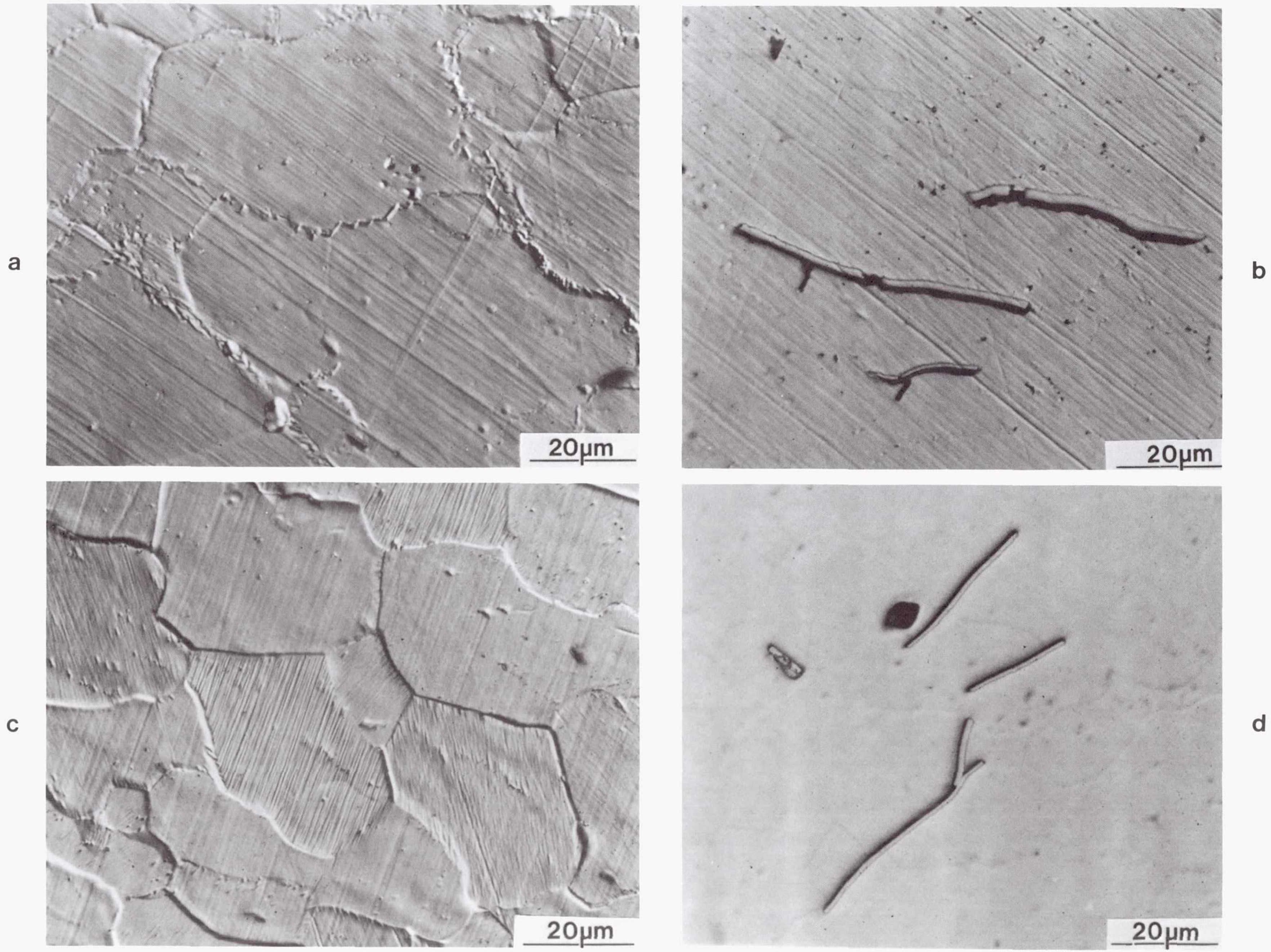

Figure 11. Optical micrographs of polished and etched cross sections obtained from the gage section (a,b) and the buttonhead grip section (c,d) of the tensile specimen deformed to 18.7% elongation at 1073K: (a) serrated grain boundaries, (b) precipitate failure, (c) undeformed grain boundaries and (d) absence of precipitate cracking.

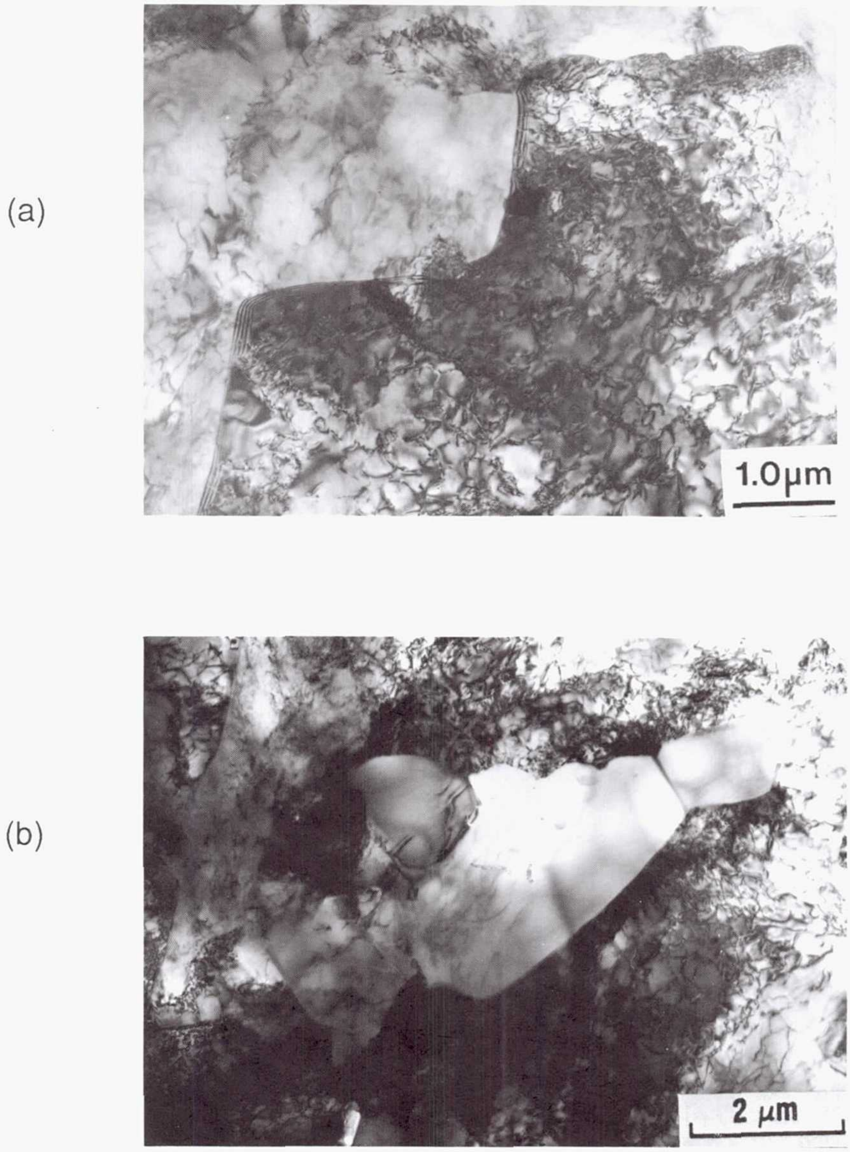

Figure 12. Transmission electron micrographs from the gage section of the specimen deformed to 18.7% at 1073K: (a) serrated grain boundary and (b) fine recrystallized grains (possibly dynamically).

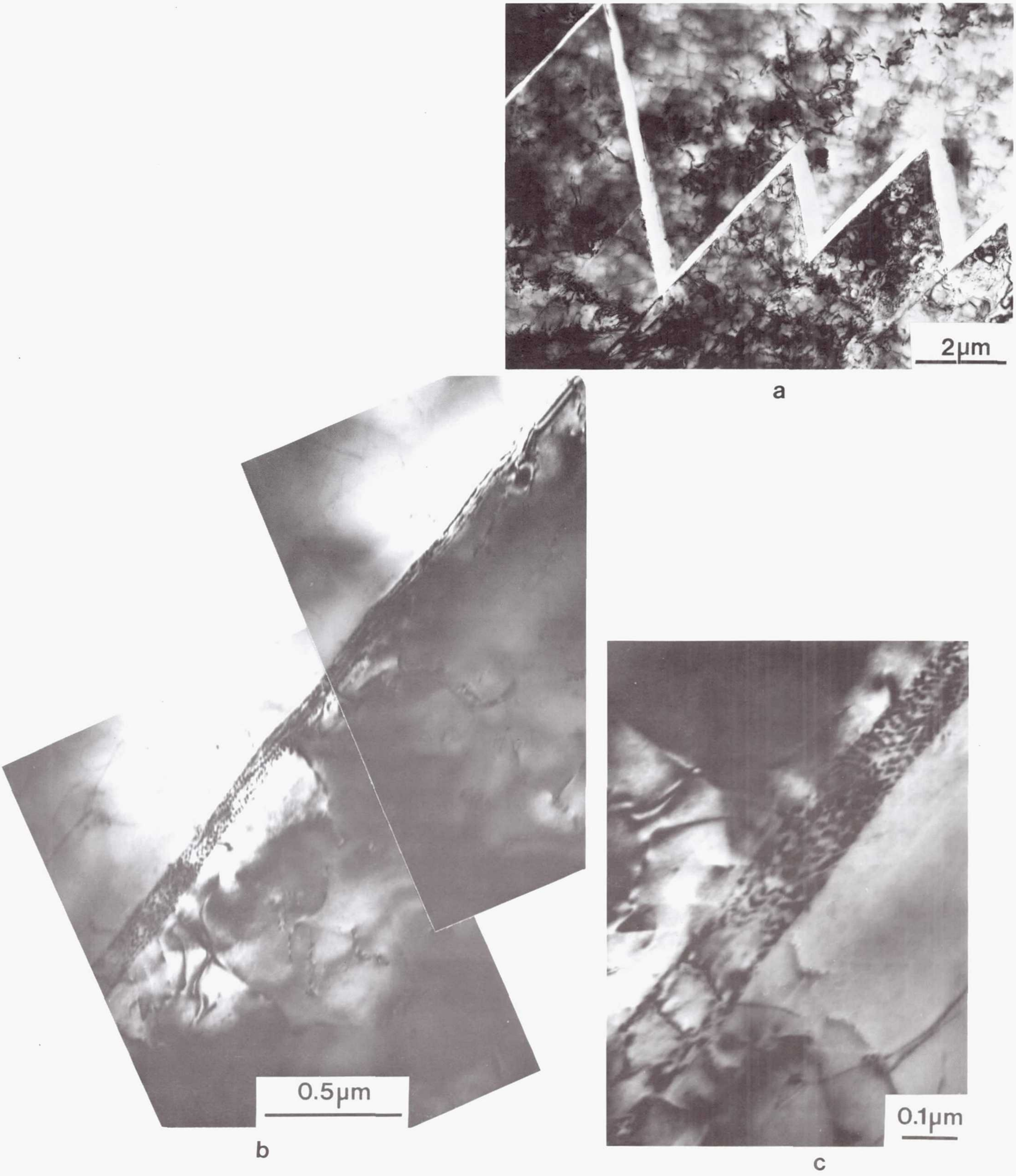

Figure 13. A crack induced at room temperature in a thin foil of the tensile specimen deformed to 18.7% at 1073K: (a) saw-tooth appearance associated with slip band formation ahead of the crack, (b,c) closely spaced dislocations lying in the slip band.

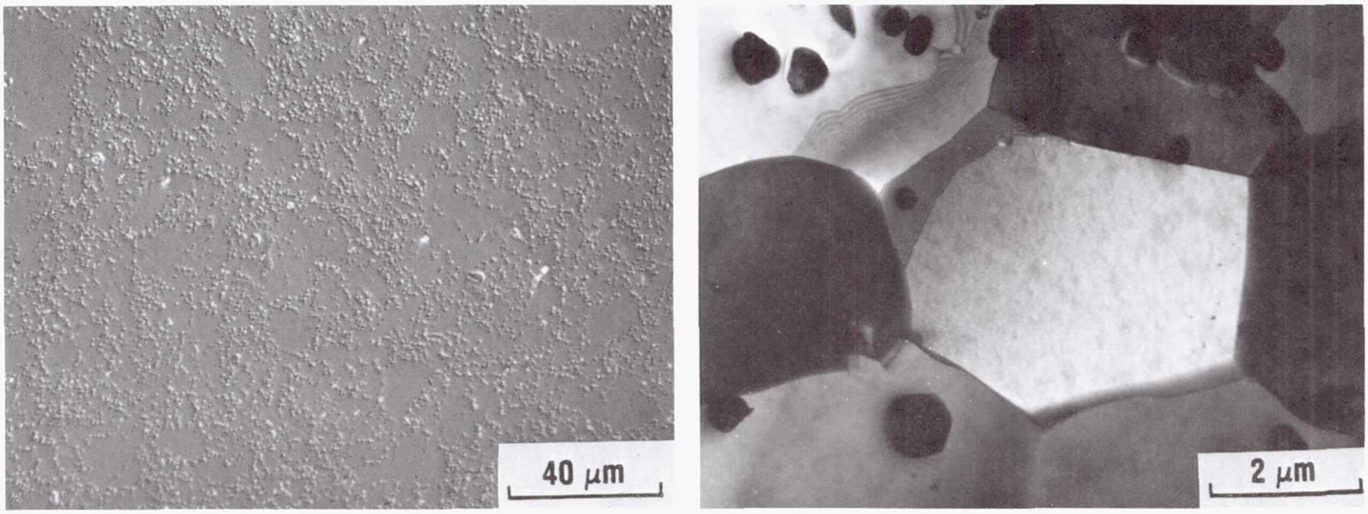

(a) (b)

Figure 14. Representative micrographs of the hot pressed monolithic $Al_{67}Ti_{25}Cr_8$: (a) optical micrograph and (b) TEM micrograph confirming both, the presence of oxides and a fine grain size.

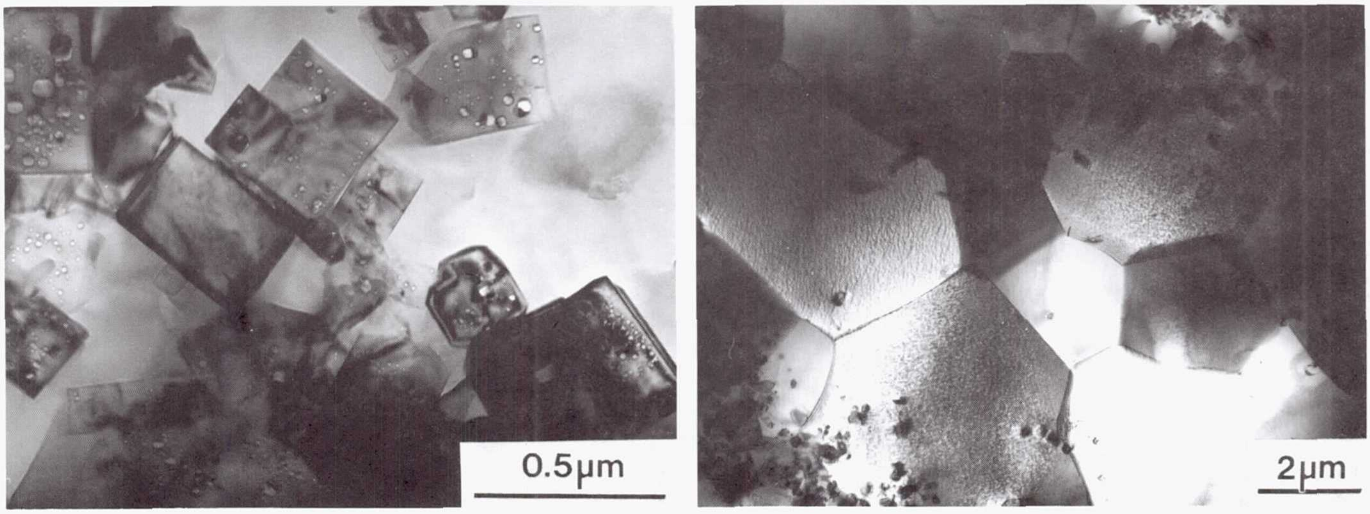

(a) (b)

Figure 15. Representative micrographs of the hot pressed monolithic $Al_{67}Ti_{25}Cr_8$ + 20 vol.% TiB_2 showing (a) the TiB_2 particle size and distribution and (b) the grain size in the TiB_2-free region.

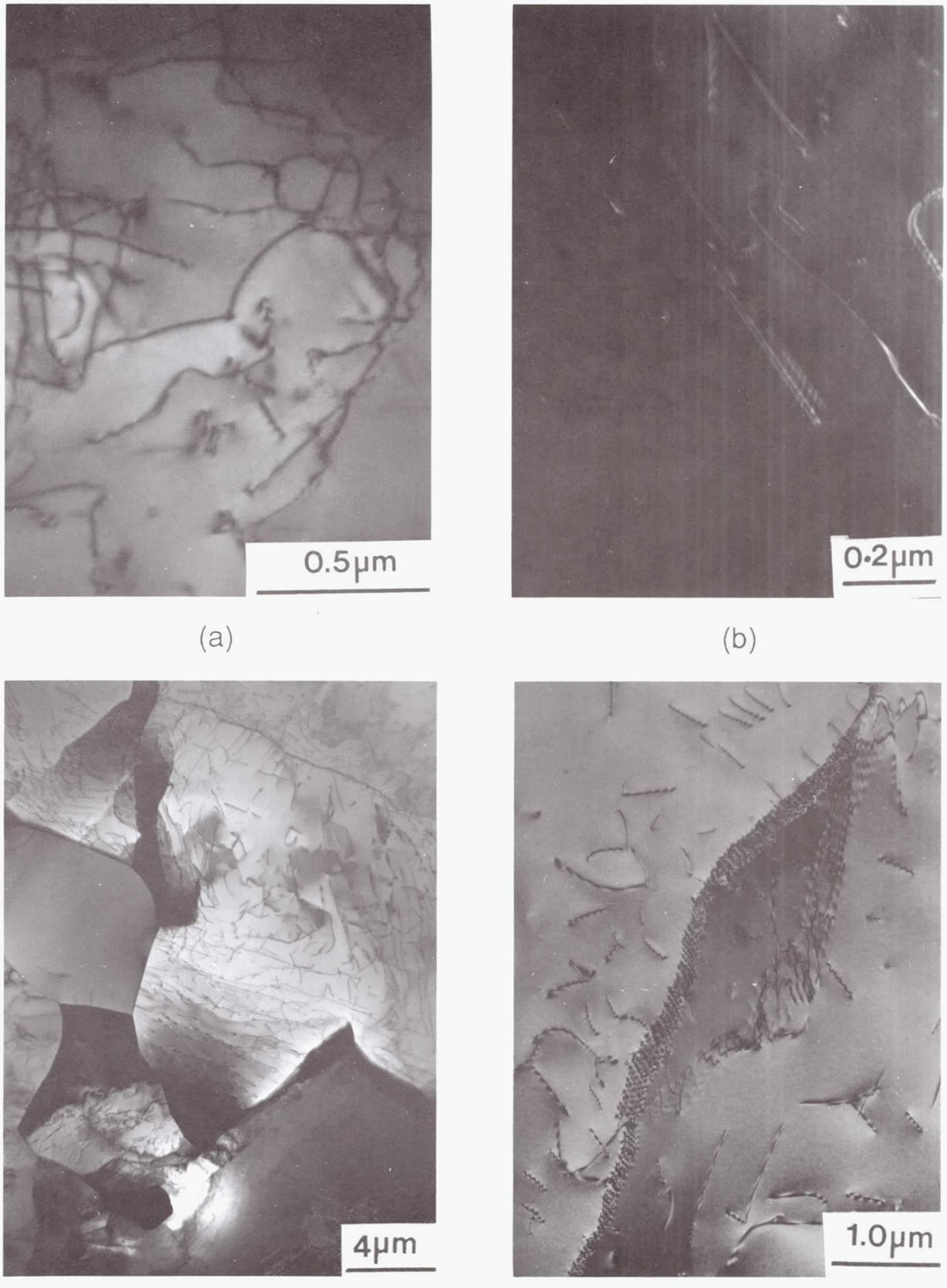

(a) (b) (c) (d)

Figure 16. Micrographs of $Al_{66}Ti_{25}Mn_9$ deformed at 1000K: (a,b) brightfield and weak beam images following deformation at a strain rate of ~2 x $10^{-4}s^{-1}$ and (c,d) strain rate of ~2 x $10^{-7}s^{-1}$.

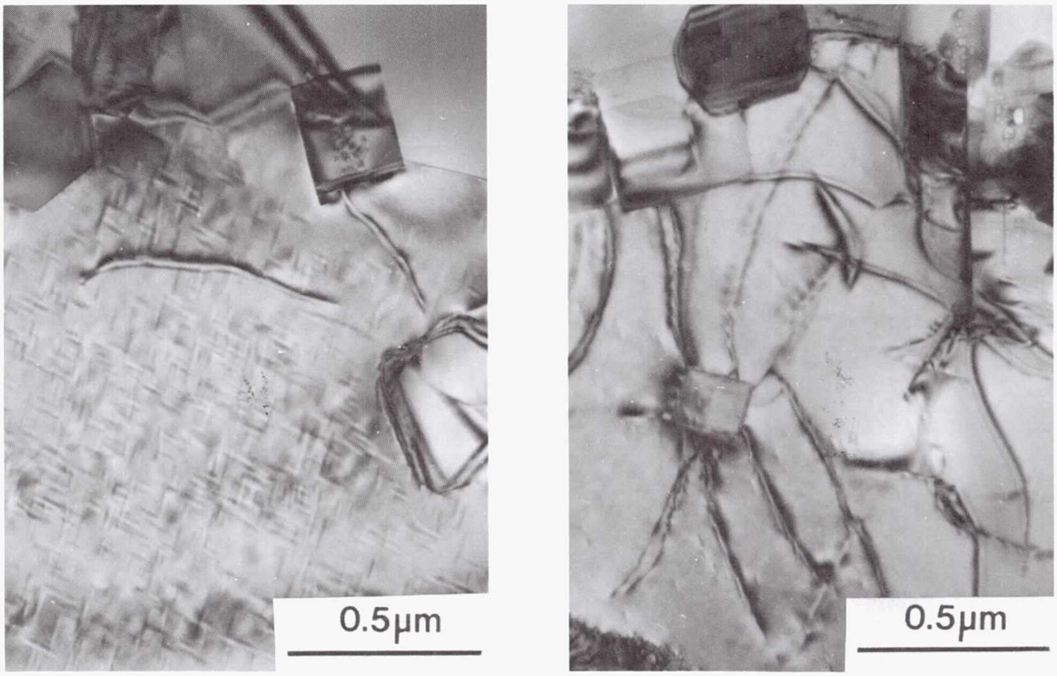

(a) (b)

Figure 17. Micrographs of $Al_{66}Ti_{25}Mn_9$ + 20 vol.% TiB_2 deformed at 1000K at a strain rate of ~2 x $10^{-4}s^{-1}$: (a) two-phase matrix and (b) TiB_2-dislocations interaction.

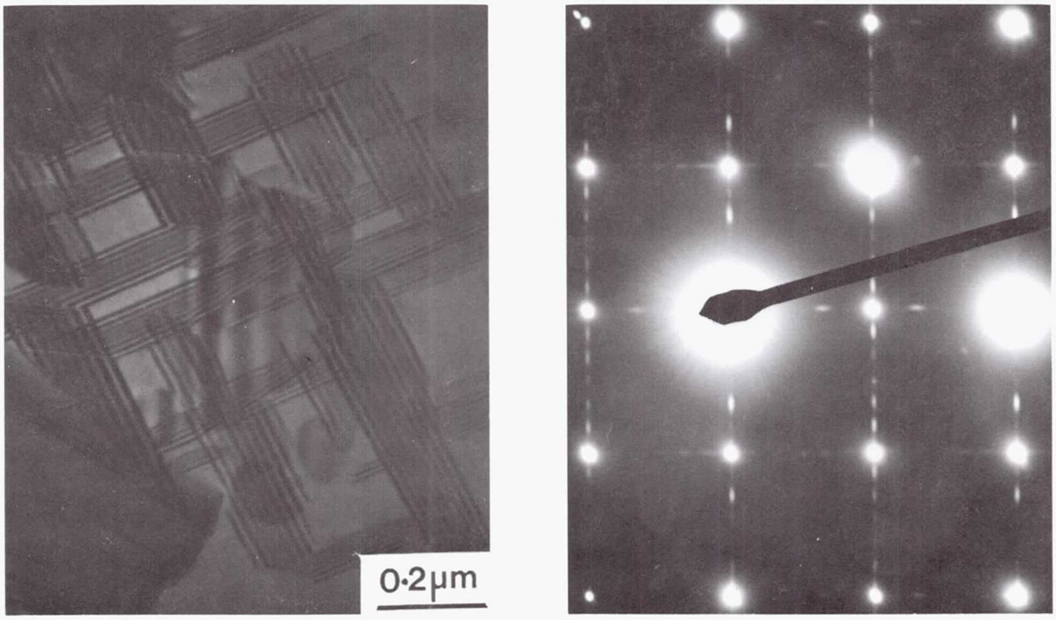

a **b**

Figure 18. Micrographs of $Al_{66}Ti_{25}Mn_9$ + 20 vol.% TiB_2 deformed at 1000K at a strain rate of ~2 x $10^{-7}s^{-1}$: (a) second phase with a lath morphology and (b) $[001]_m$ zone axis diffraction pattern confirming the presence of a second phase.

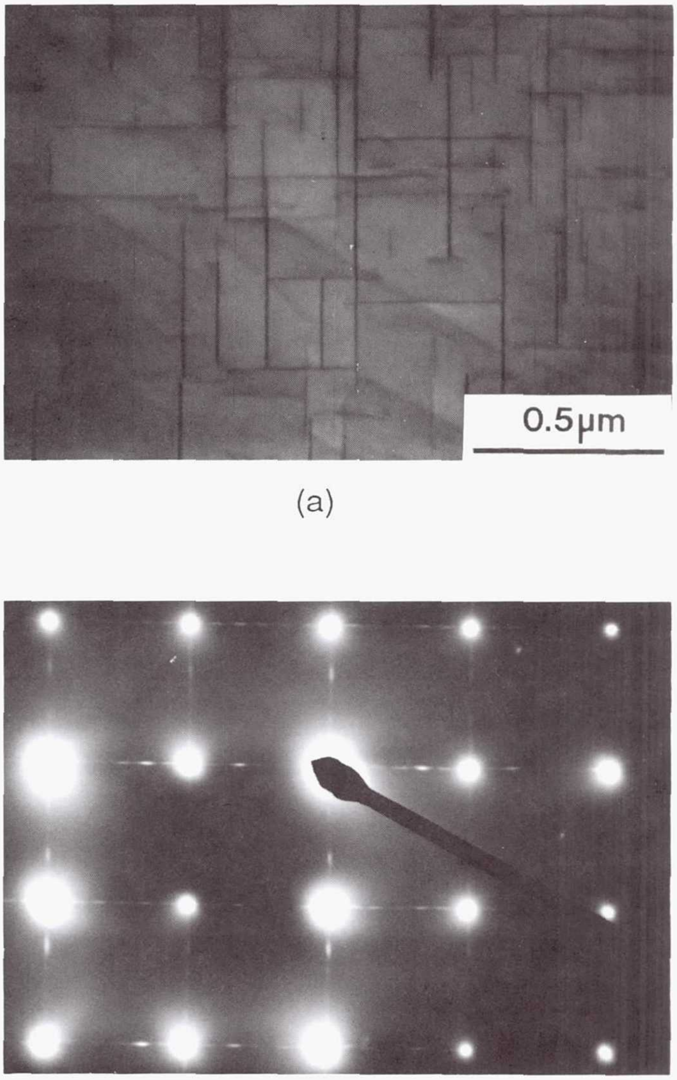

(a)

(b)

Figure 19. TEM micrographs of the $Al_{66}Ti_{25}Mn_9$ + 20 vol.% TiB_2 specimen heat treated at 973K for a day (a) showing the presence of a second phase precipitation and (b) $[001]_m$ zone axis diffraction pattern confirming its similarity to that observed in the deformed specimen in the previous figure.

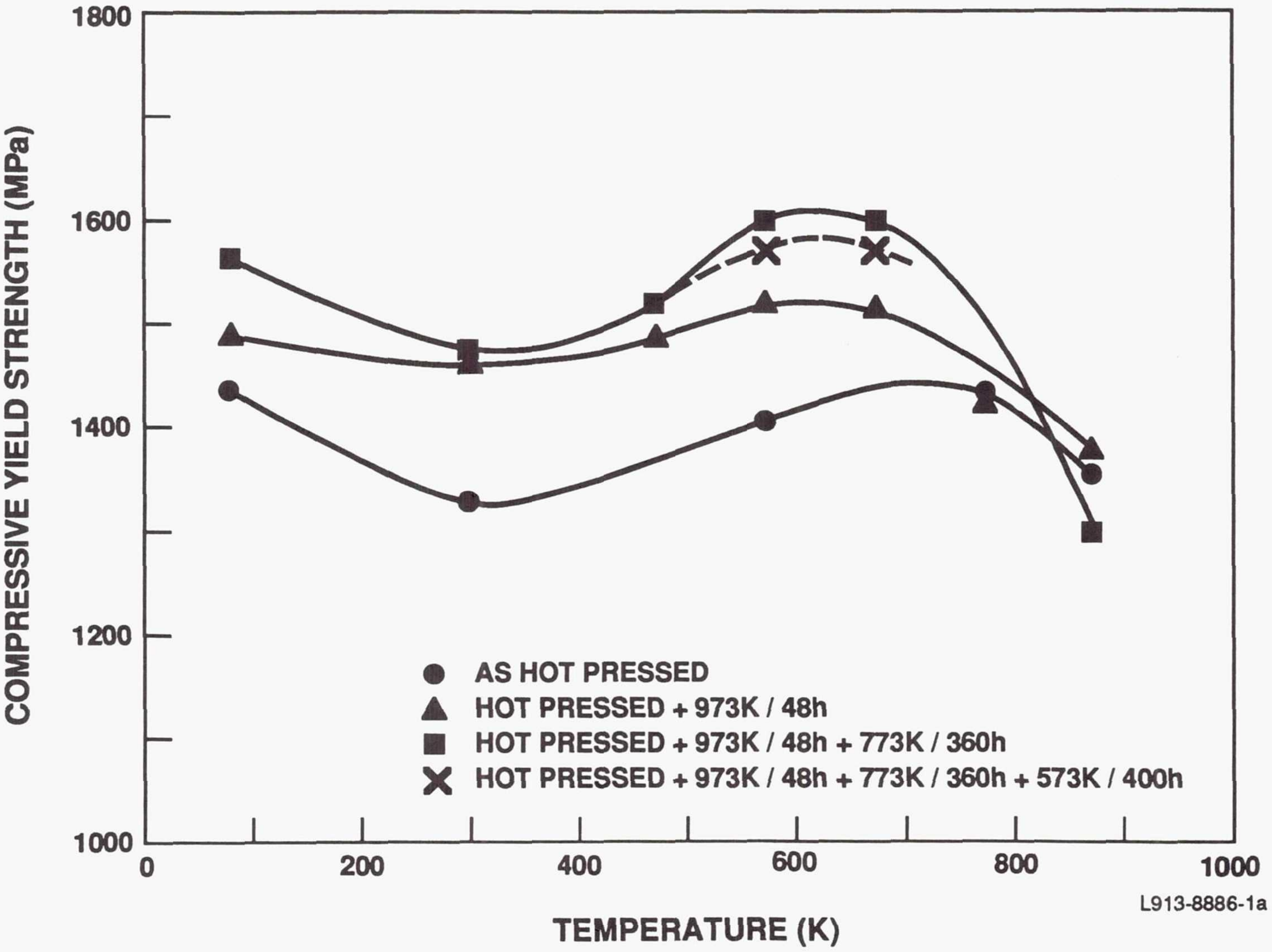

Figure 20. A comparison of the compressive yield strength-temperature profile in the temperature regime 77K - 873K of as hot pressed $Al_{66}Ti_{25}Mn_9$ + 20 vol.% TiB_2 with those that were heat treated according to the various schedules prior to testing.

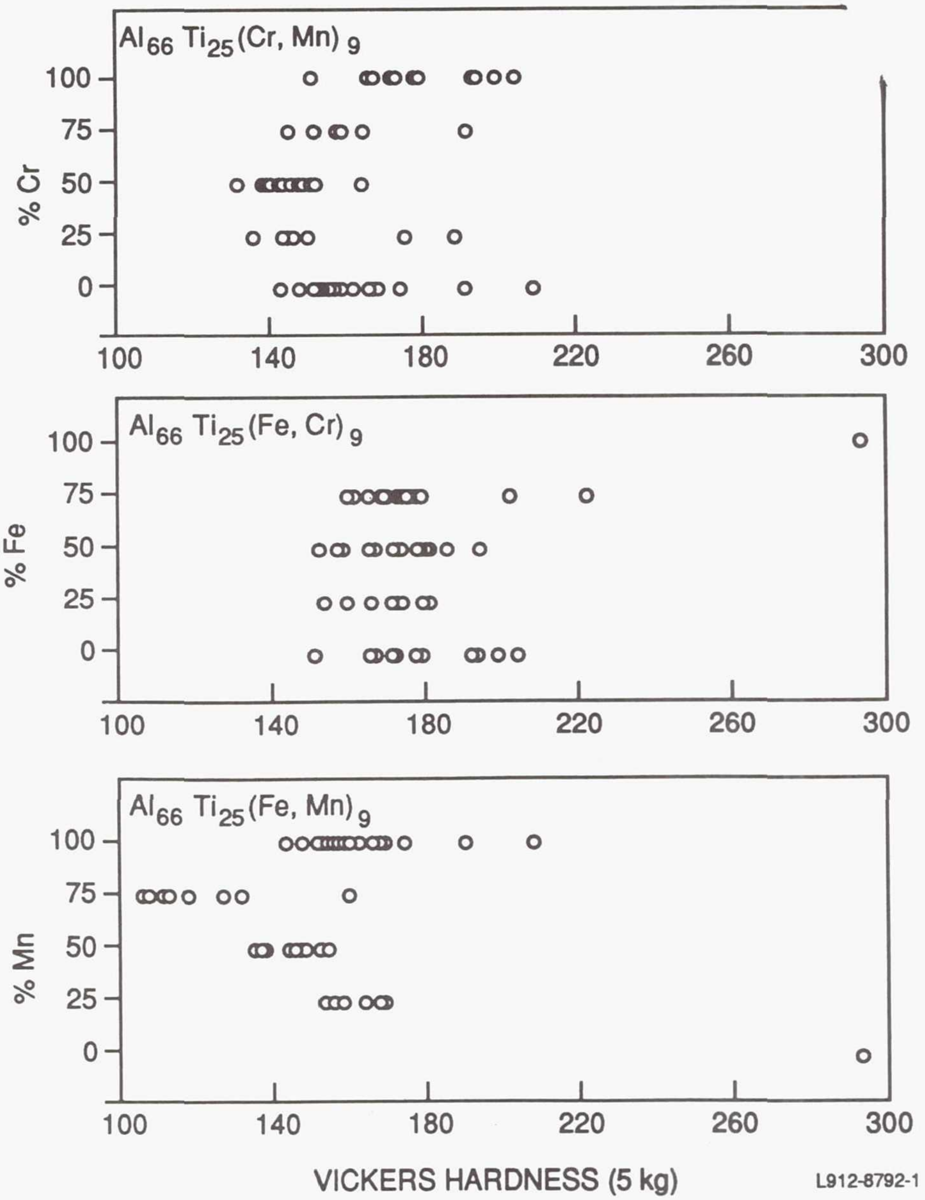

Figure 21 Variation in hardness with composition of the quaternary trialuminides in the cast and homogenized condition.

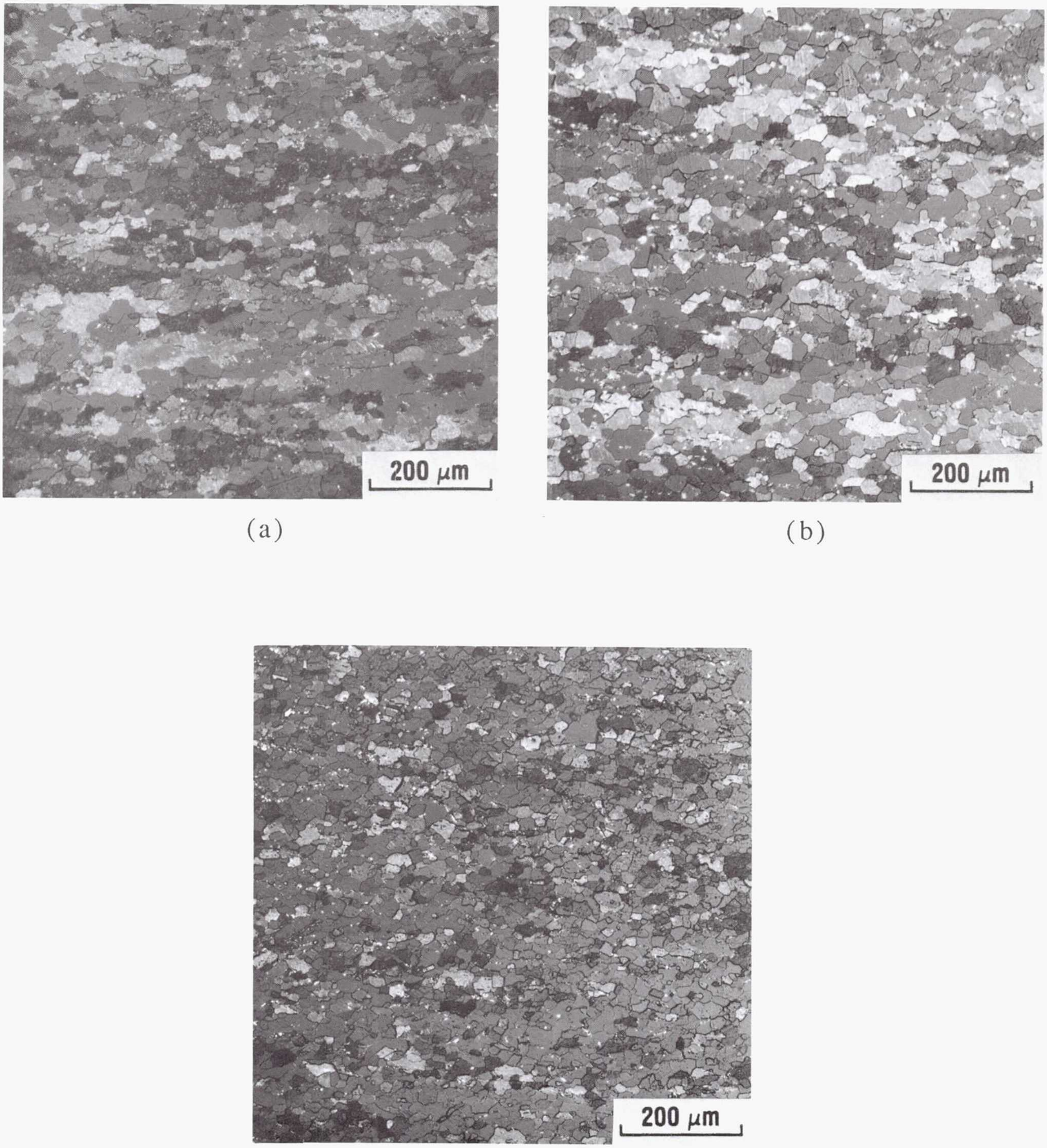

(a) (b)

(c)

Figure 22. Polished and etched cross-sections of the quaternary and quinary forgings: (a) $Al_{66}Ti_{25}Cr_{4.5}Mn_{4.5}$, (b) $Al_{66}Ti_{25}Mn_{6.75}Fe_{2.25}$ and (c) $Al_{66}Ti_{25}Mn_{4.5}Cr_{3.0}Fe_{1.5}$.

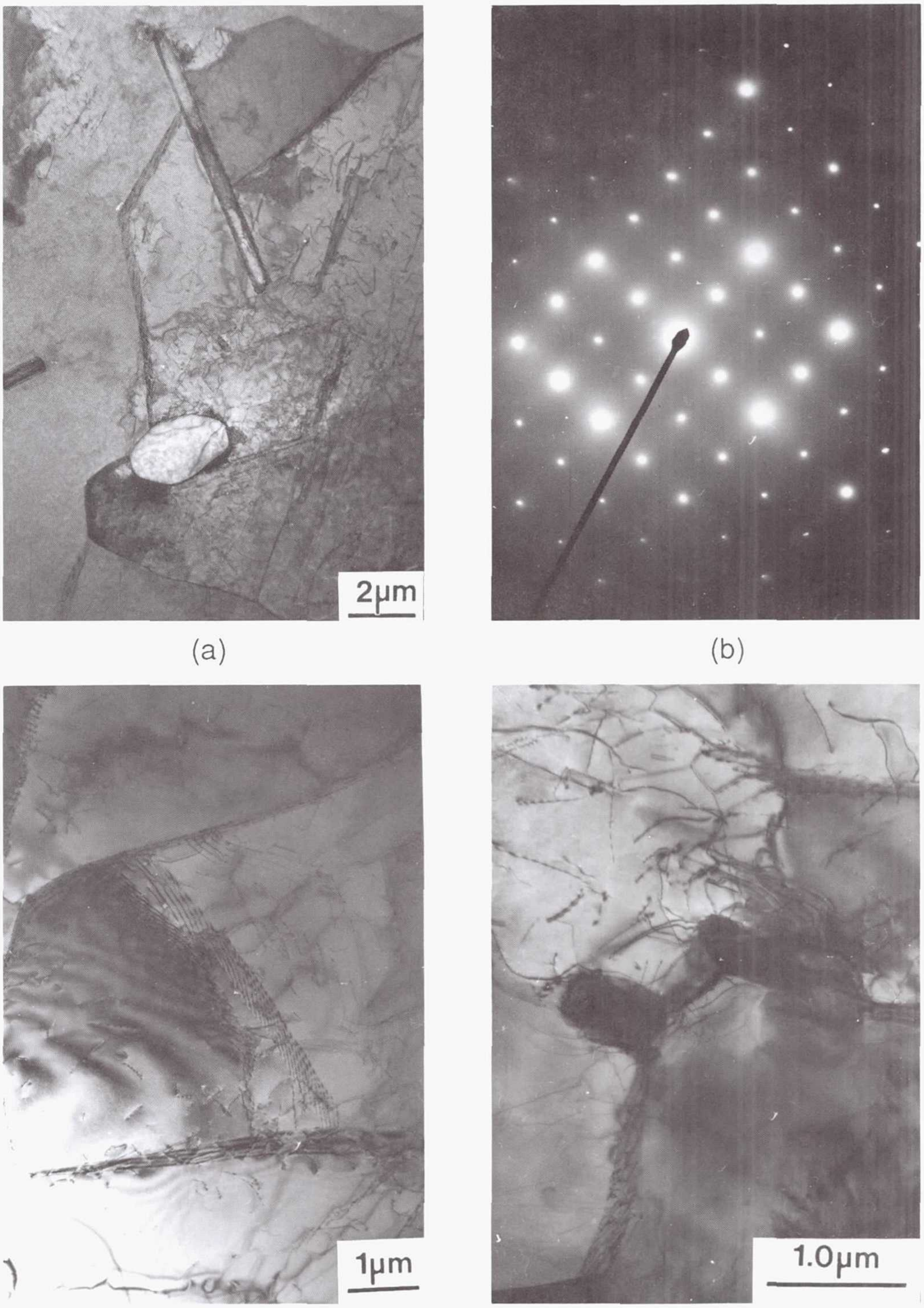

(a) (b)

(c) (d)

Figure 23. Transmission electron micrographs of $Al_{66}Ti_{25}Mn_{4.5}Fe_{4.5}$ showing (a) presence of precipitates at grain boundaries and subgrain boundaries, (b) [100]m diffraction pattern showing the absence of fine second phase precipitates within the grains and of the quinary composition showing (c) subgrains and (d) grain and subgrain boundary second phase.

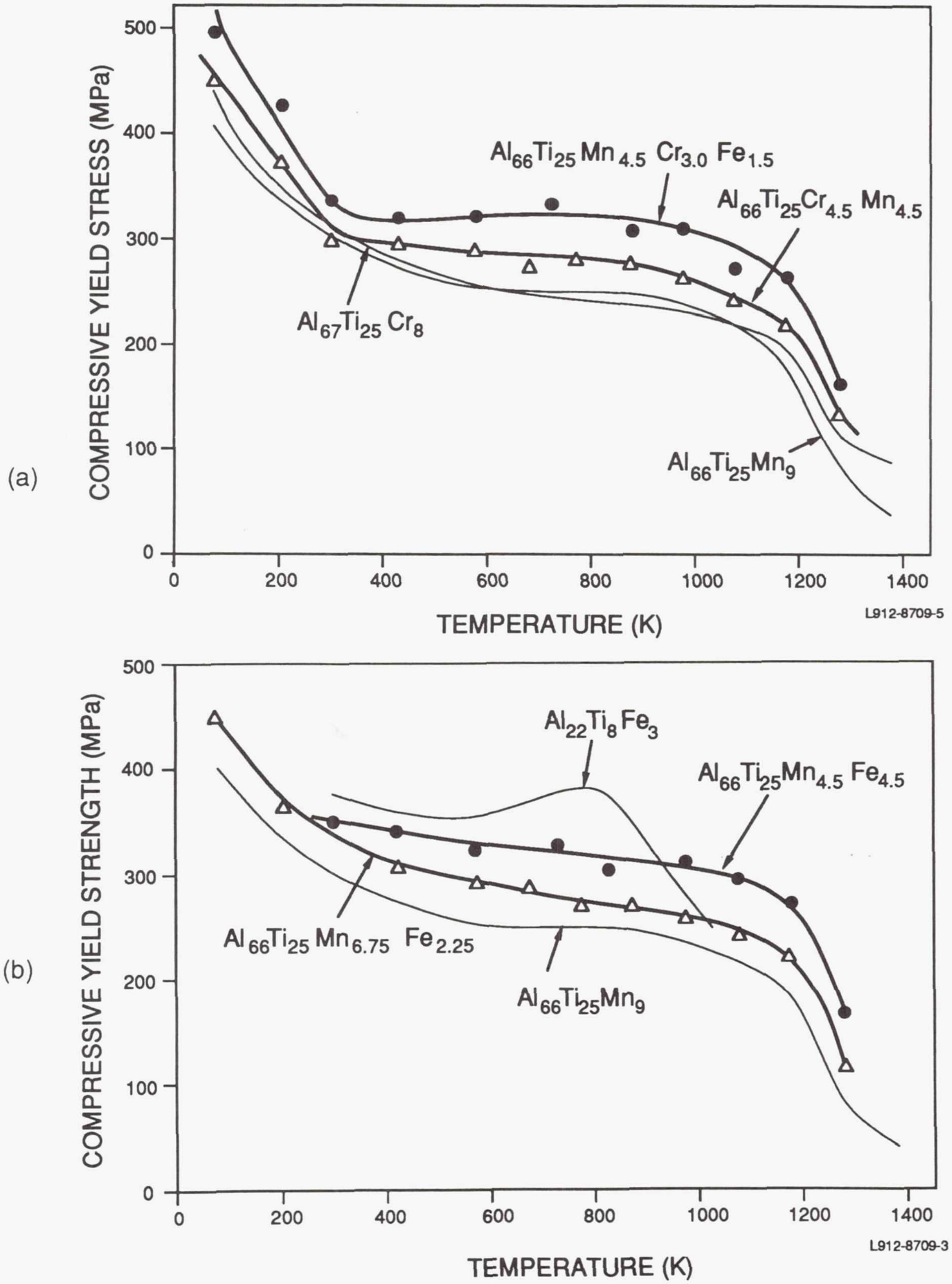

Figure 24. Compressive yield strength profiles for (a) $Al_{66}Ti_{25}Cr_{4.5}Mn_{4.5}$ and $Al_{66}Ti_{25}Mn_{4.5}Cr_{3.0}Fe_{1.5}$ as compared to the ternaries, and (b) the effect of increasing Fe content in the Mn-based system.

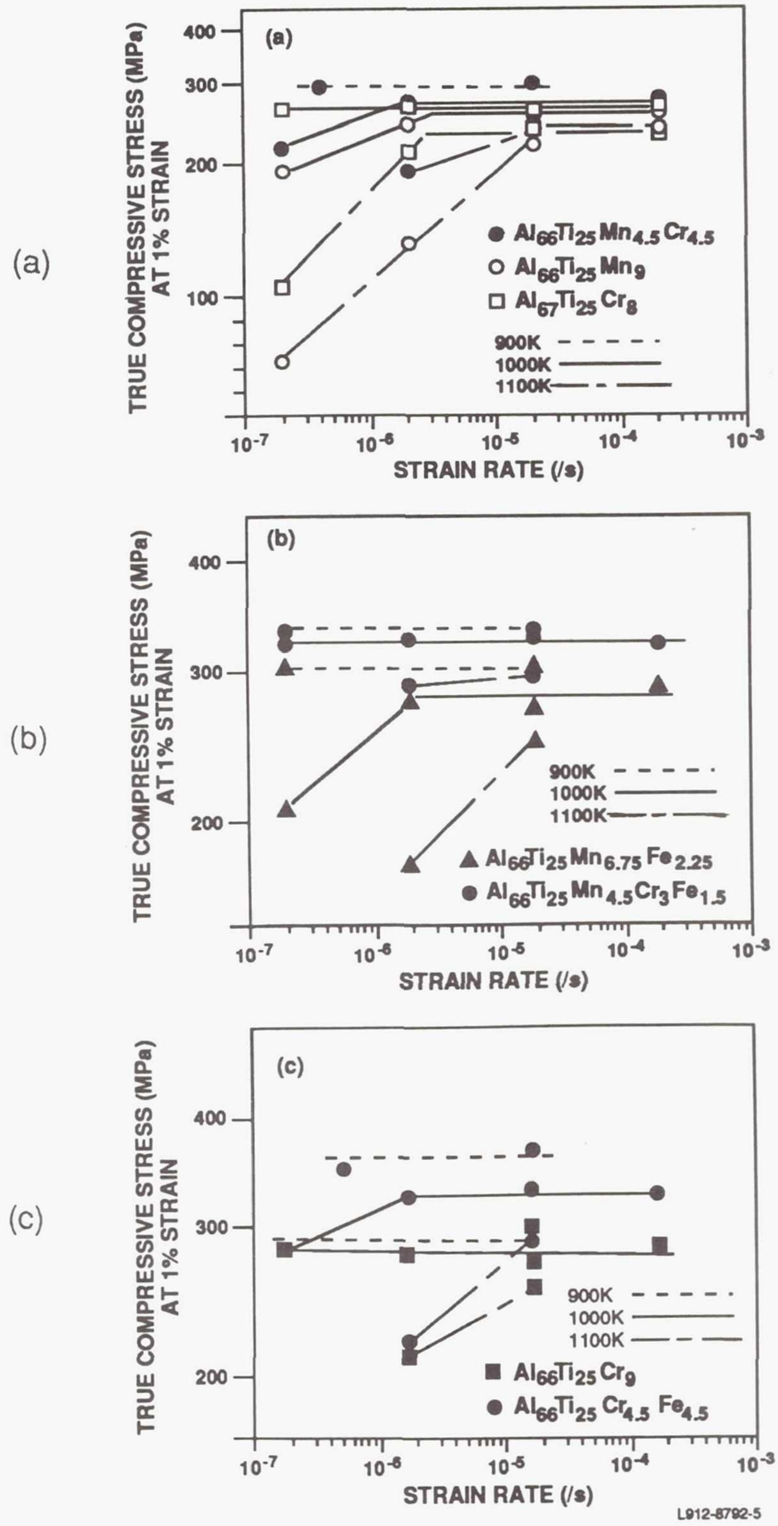

Figure 25. Compressive flow stress at 1% strain versus strain rate in the temperature range 900K-1100K for (a) $Al_{66}Ti_{25}Mn_{4.5}Cr_{4.5}$ as compared to $Al_{66}Ti_{25}Mn_9$ and $Al_{67}Ti_{25}Cr_8$, (b) $Al_{66}Ti_{25}Mn_{6.75}Fe_{2.25}$ and $Al_{66}Ti_{25}Mn_{4.5}Cr_{3.0}Fe_{1.5}$, and (c) $Al_{66}Ti_{25}Cr_9$ and $Al_{66}Ti_{25}Cr_{4.5}Fe_{4.5}$.

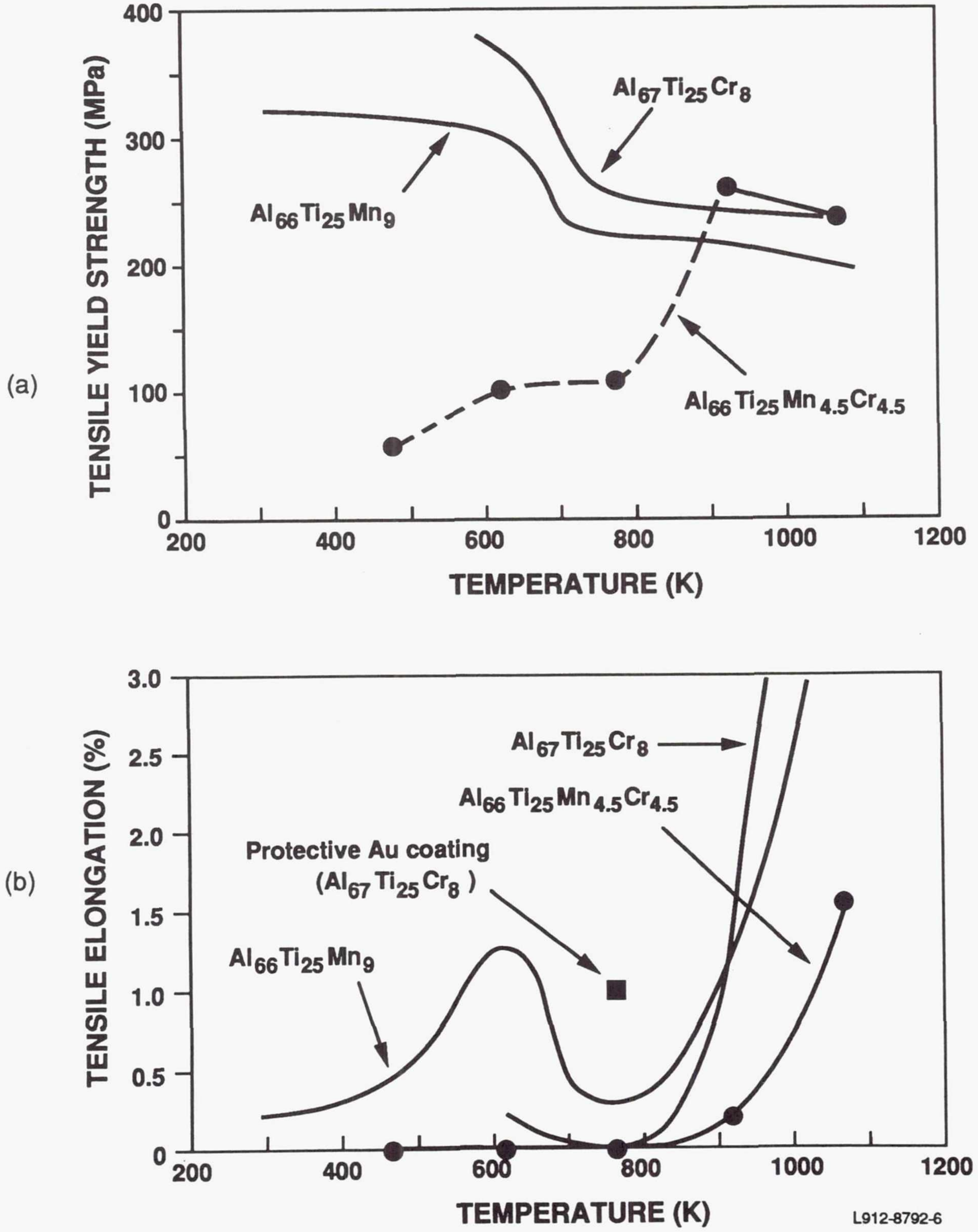

Figure 26. A comparison of the tensile behavior of $Al_{66}Ti_{25}Mn_{4.5}Cr_{4.5}$ with $Al_{67}Ti_{25}Cr_8$ and $Al_{66}Ti_{25}Mn_9$: (a) yield strength versus temperature, and (b) ductility versus temperature.

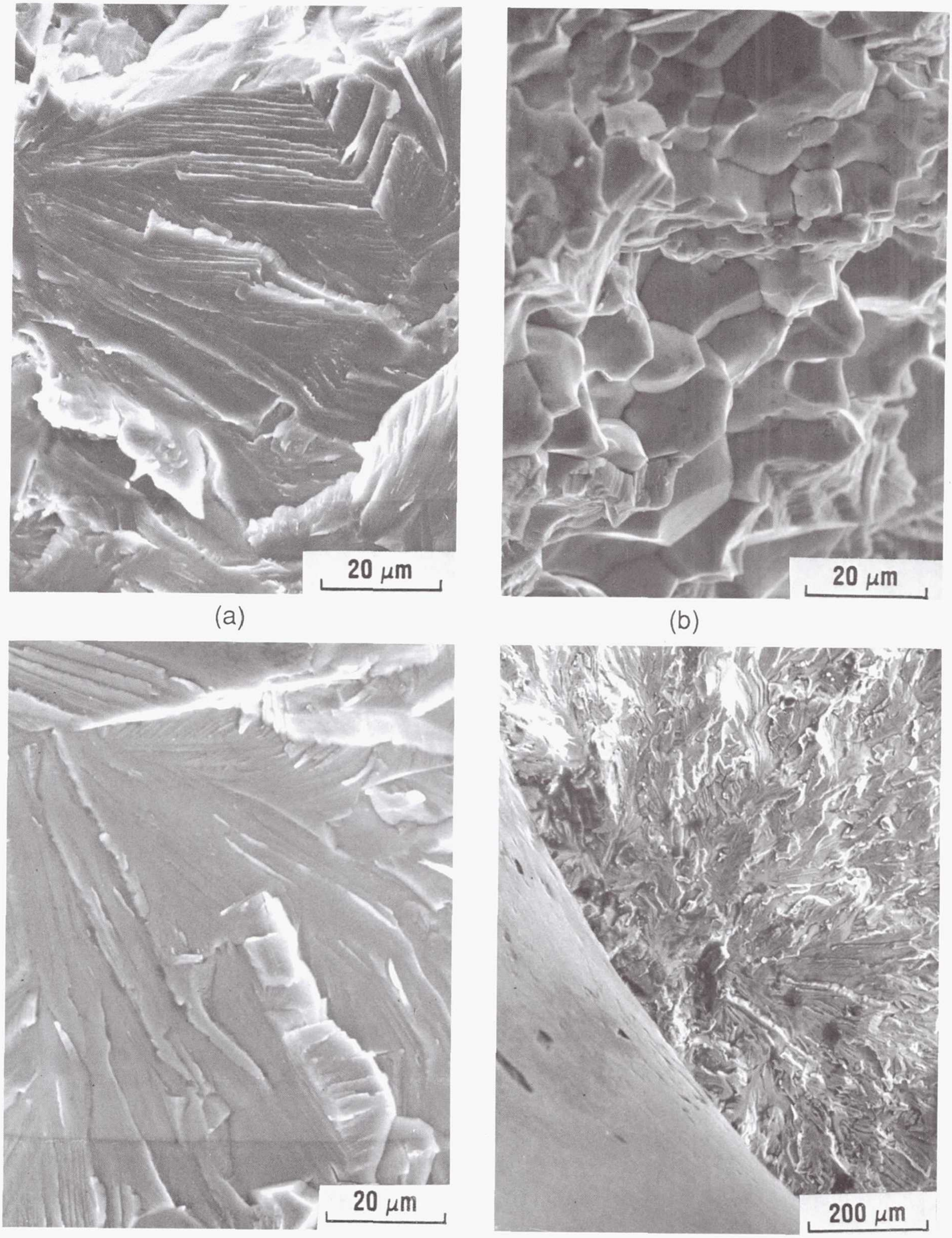

(a) (b)

(c) (d)

Figure 27. Tensile fracture surfaces of $Al_{66}Ti_{25}Mn_{4.5}Cr_{4.5}$: (a) transgranular cleavage at 473K, (b,c) intergranular failure mixed with transgranular cleavage at 773K, and (d) single fracture initiation site at 623K.

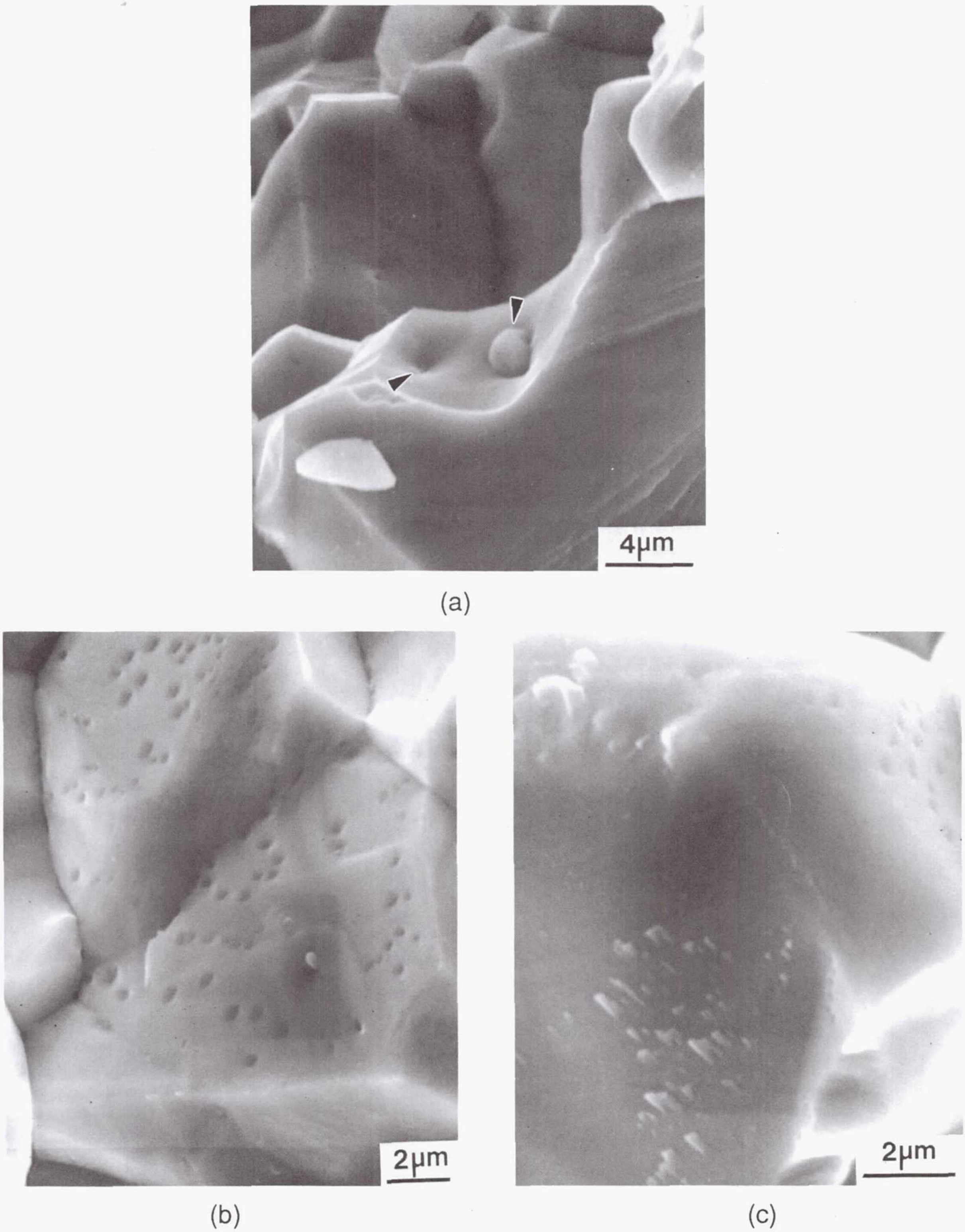

Figure 28. The fracture surface of the 1073K tensile specimen of the quinary alloy, $Al_{66}Ti_{25}Mn_{4.5}Cr_{3.0}Fe_{1.5}$ reveals (a) intergranular failure. Some of the grain boundaries exhibit (b) dimples while others (c) contain fine precipitates.

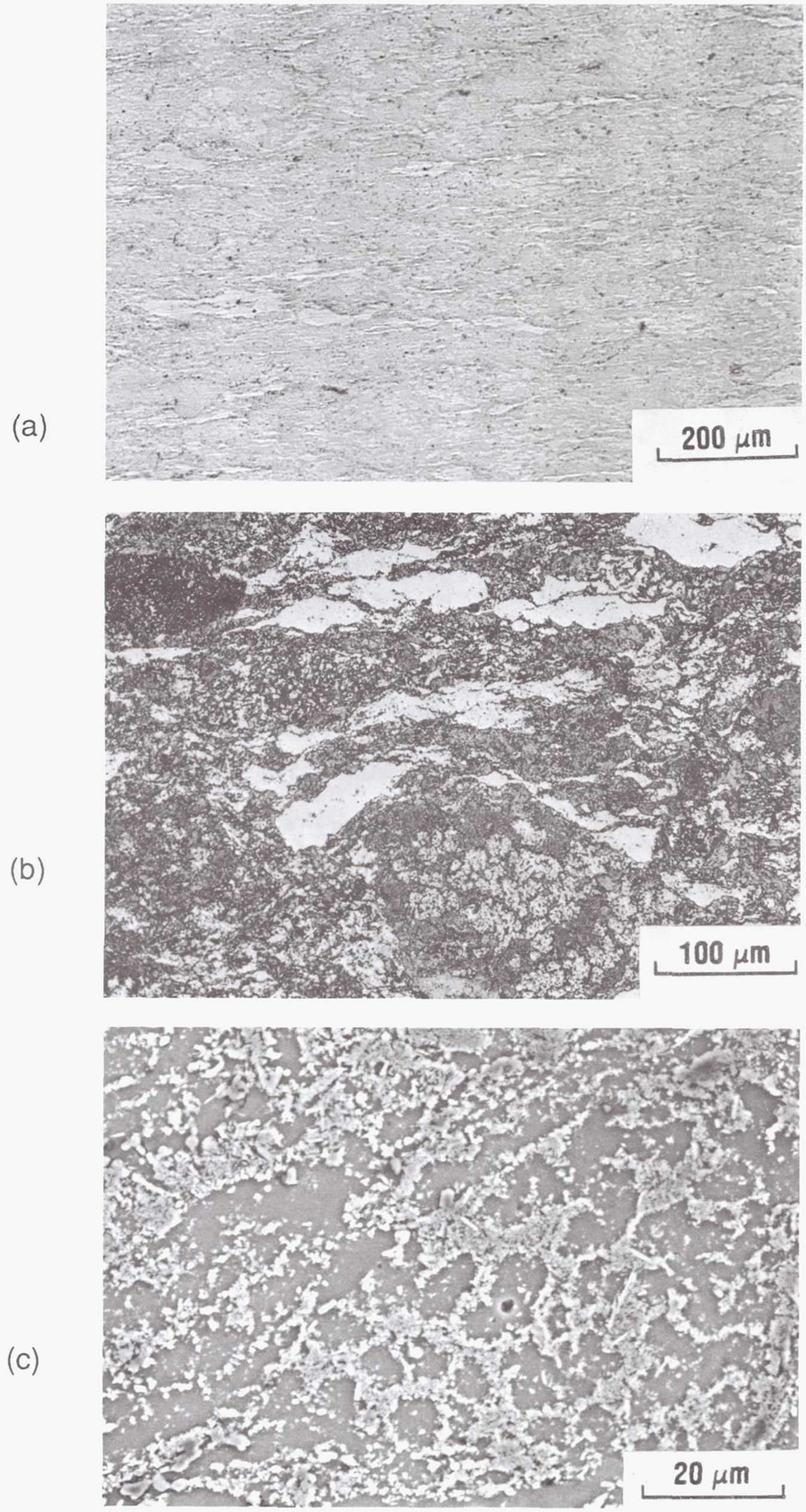

Figure 29. Micrographs of $Al_{67}Ti_{25}Cr_9$ + 20 vol.% TiB_2 forged composite (67% height reduction): (a) unetched - layered structure, (b) etched - TiB_2-free regions and (c) SEM image showing TiB_2 distribution.

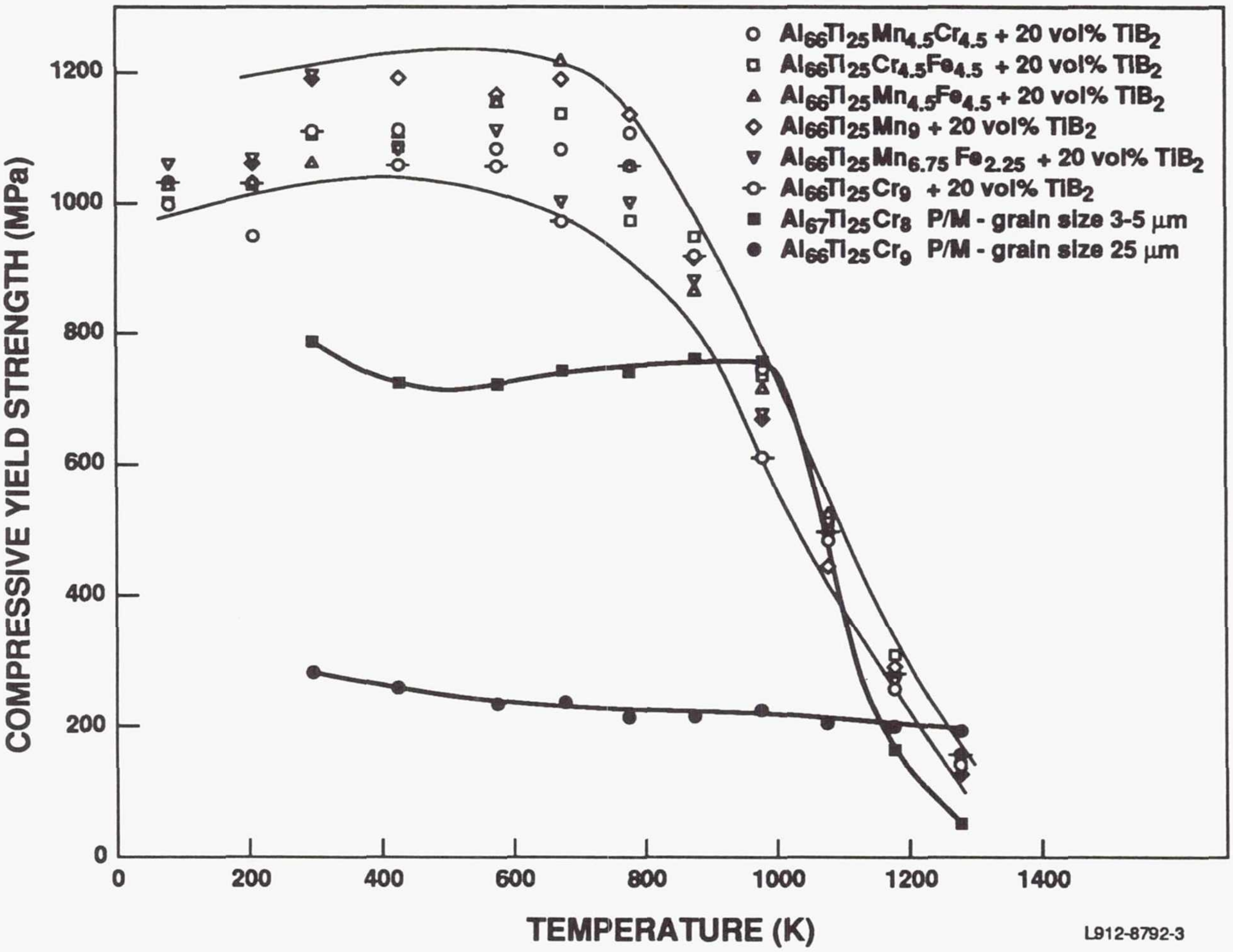

Figure 30. Compressive yield strength-temperature profiles for the P/M-processed monolithic and particulate-reinforced composite materials.

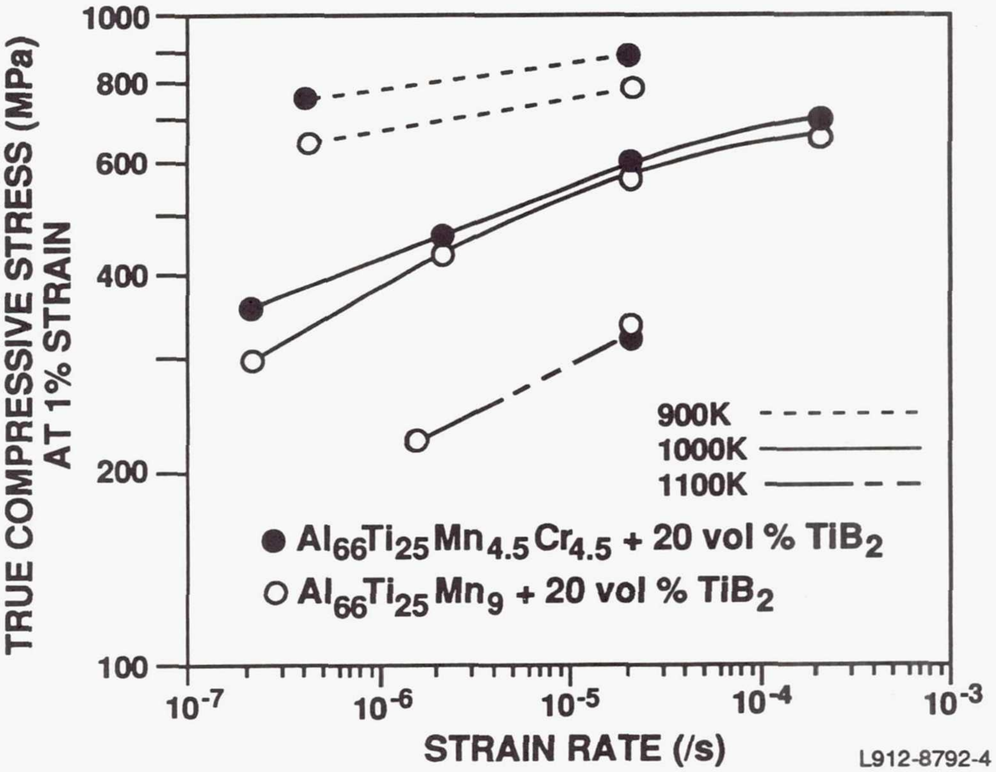

Figure 31. Compressive flow stress at 1% strain versus strain rate in the temperature range 900K-1100K for 20 vol.% TiB_2-reinforced $Al_{66}Ti_{25}Mn_9$ and $Al_{66}Ti_{25}Mn_{4.5}Cr_{4.5}$.

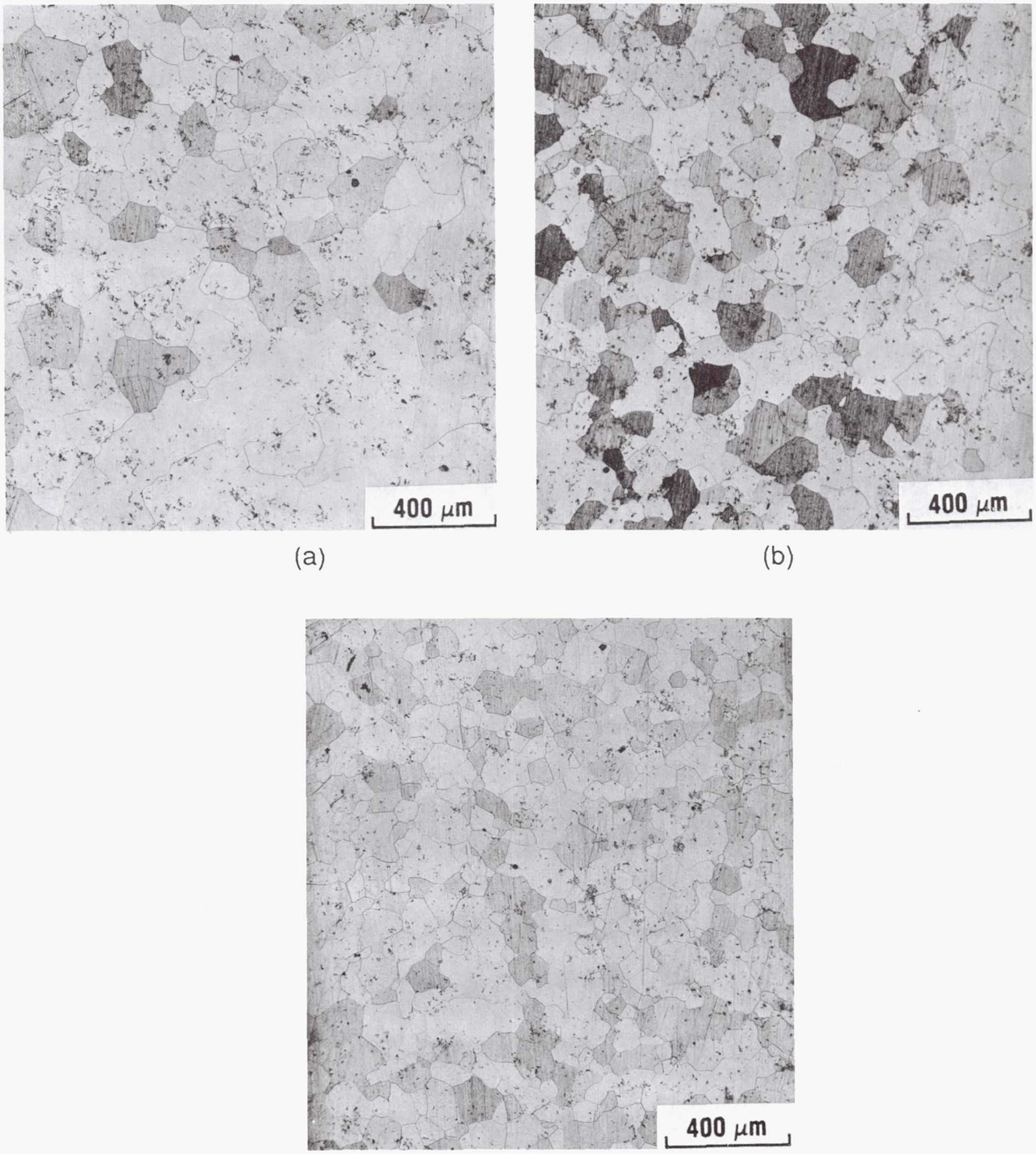

(a)

(b)

(c)

Figure 32. The effect of thermal exposure (1473K, 45h) on grain size of (a) $Al_{66}Ti_{25}Mn_{6.75}Fe_{2.25}$, (b) $Al_{66}Ti_{25}Mn_{4.5}Cr_{4.5}$, and (c) $Al_{66}Ti_{25}Mn_{4.5}Cr_{3.0}Fe_{1.5}$.

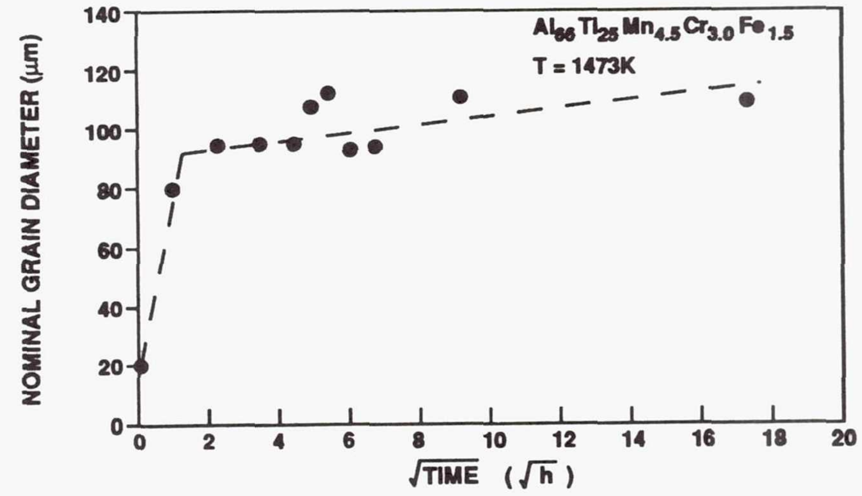

Figure 33. Grain growth characteristics of the quinary alloy at 1473K.

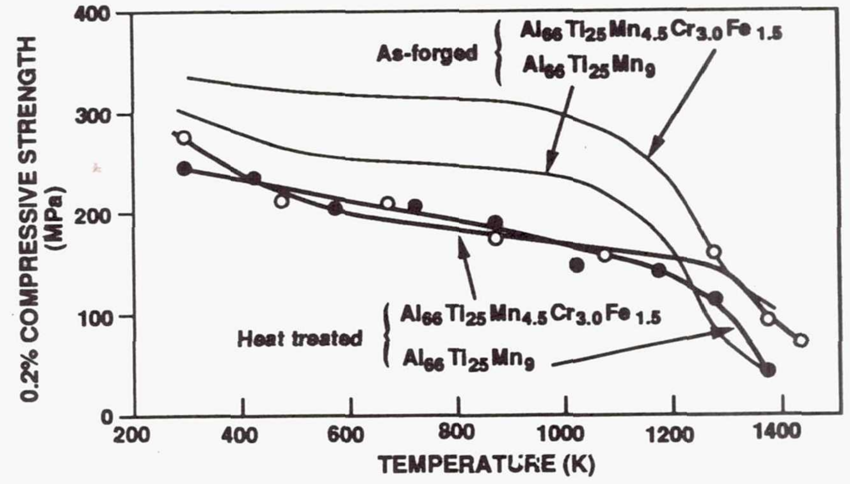

Figure 34. Effect of heat-treatment on the compressive yield strength-temperature profiles of ternary $Al_{66}Ti_{25}Mn_9$ and quinary $Al_{66}Ti_{25}Mn_{4.5}Cr_{3.0}Fe_{1.5}$.

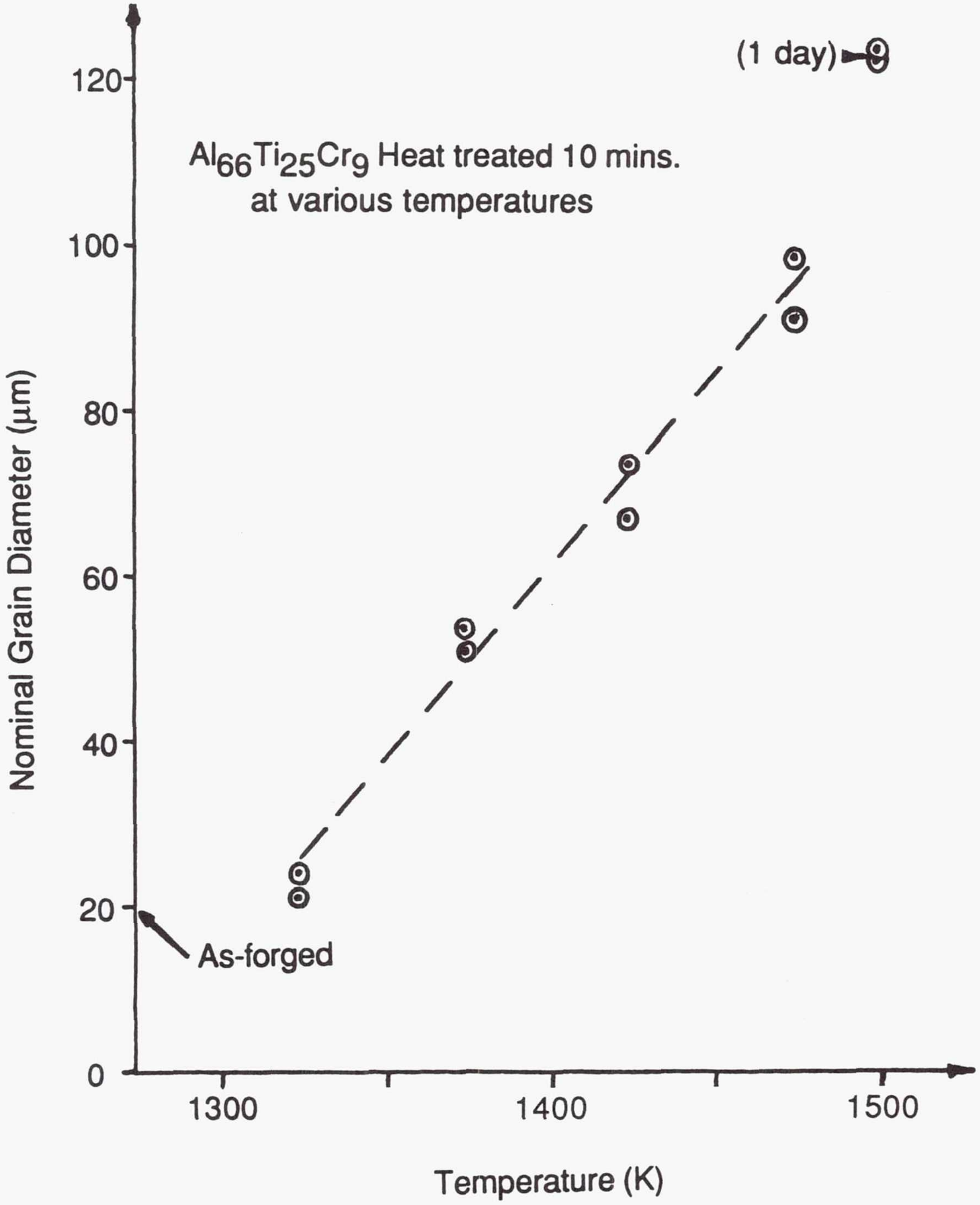

Figure 35. Variation in grain size with exposure temperature for $Al_{66}Ti_{25}Cr_9$.

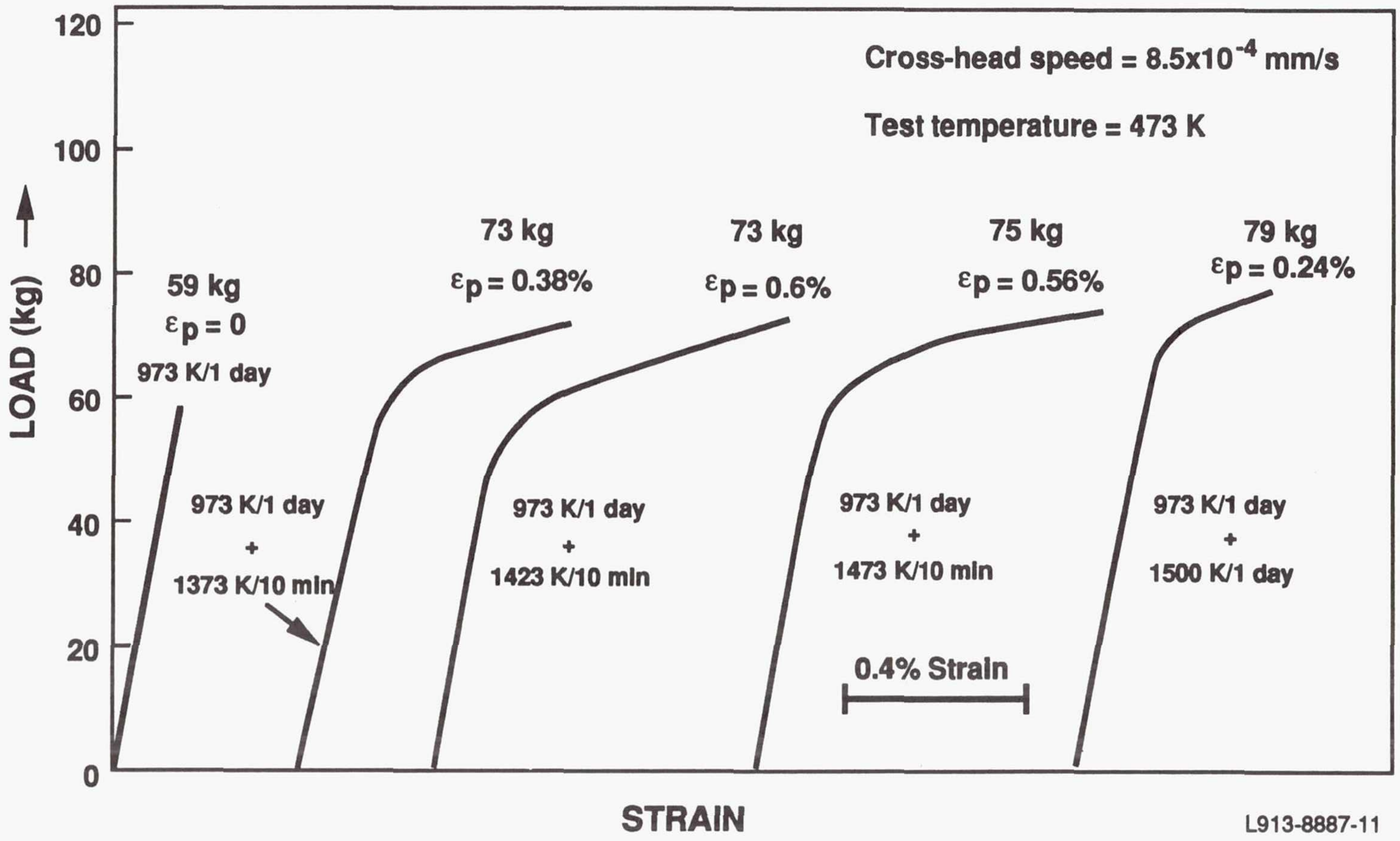

Figure 36. Load-strain curves from three point bend tests for $Al_{66}Ti_{25}Cr_9$ after the specimens were subjected to various heat treatments. Tests were performed at 473K at a cross head speed of 8.5 x 10^{-4} mm/s.

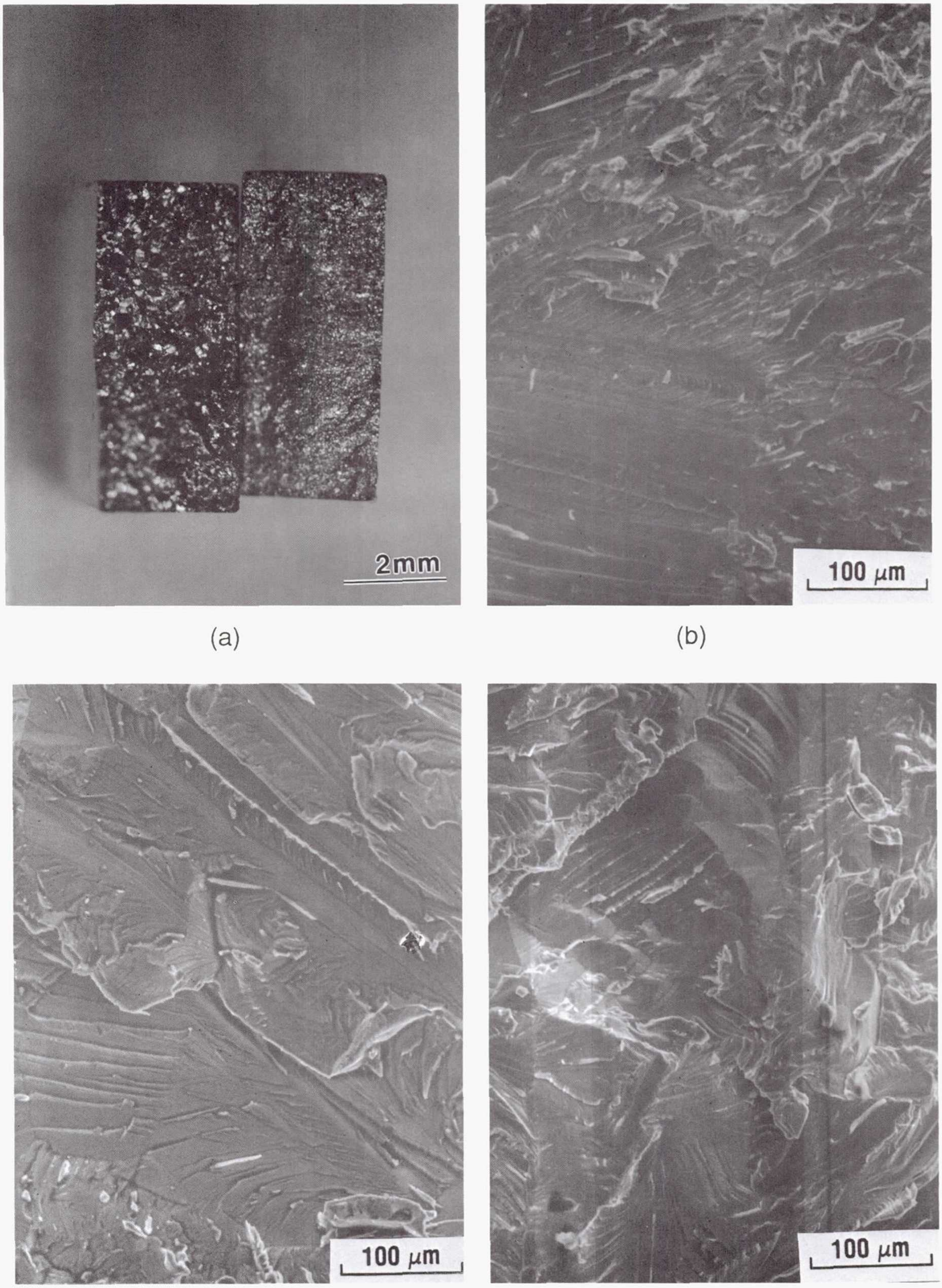

(a) (b)

(c) (d)

Figure 37. Fracture surfaces of the bend tested specimens: (a) low magnification photograph of specimen heat treated at 973K/1 day (right) and at 973K/1 day + 1500K/1 day (left); SEM micrographs of fracture surfaces of specimens heat treated (b) 973K/1 day, (c) 973K/1 day + 1423K/10 min, and (d) 973K/1 day + 1500K/1 day.

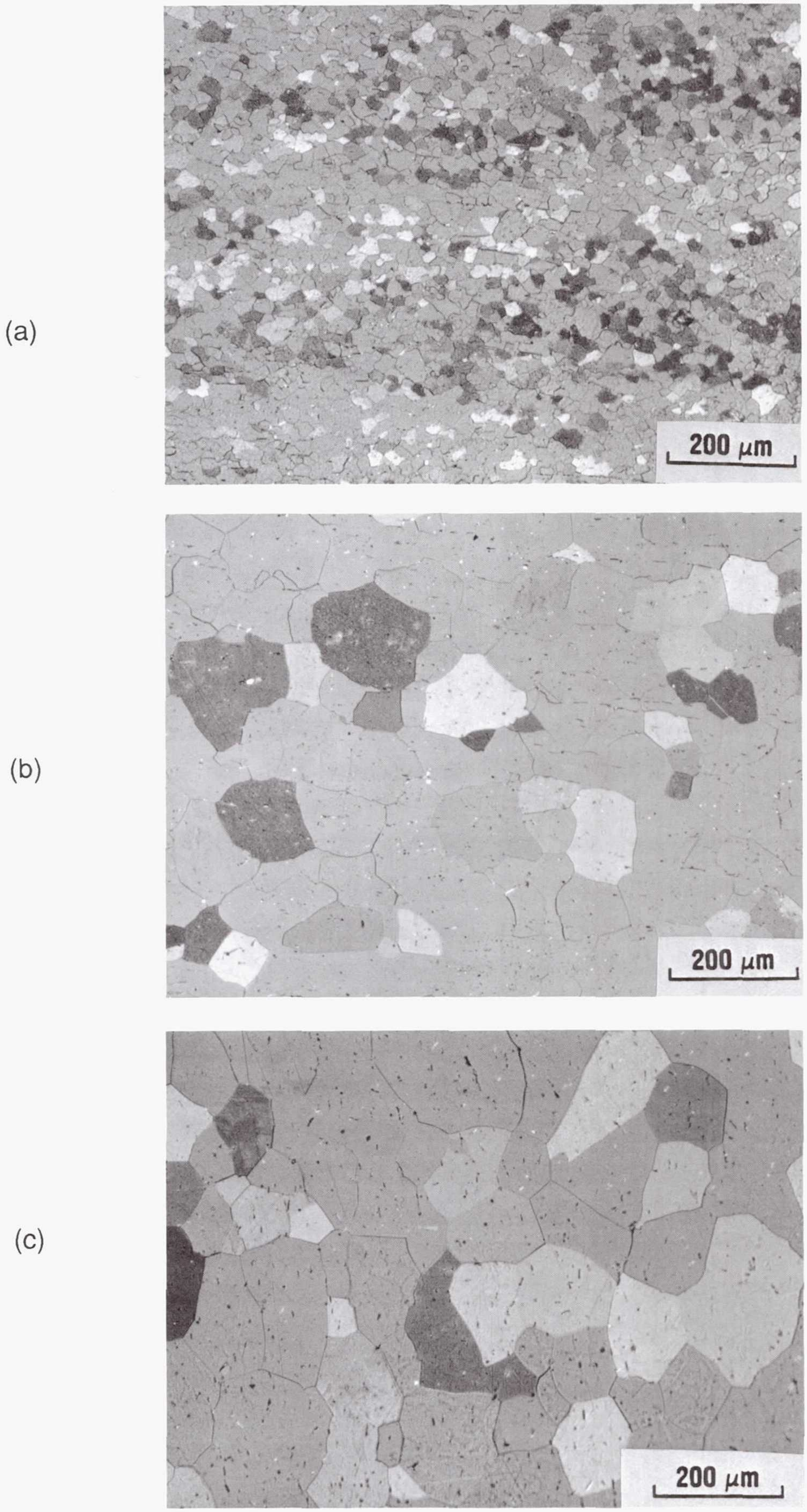

Figure 38. Variation in grain size as a function of heat treatment: (a) forged + 973K/1 day, (b) forged + 973K/1 day + 1423K/10 min. and (c) forged + 973K/1 day + 1500K/1 day.

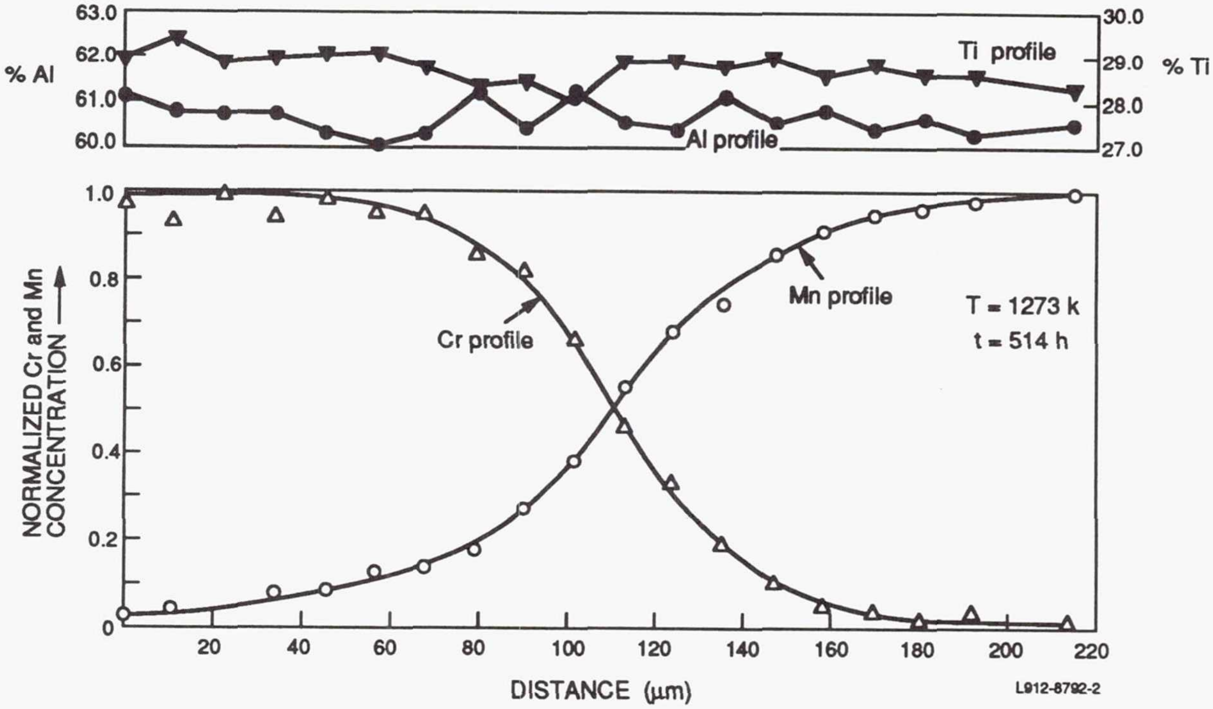

Figure 39. Concentration-distance profiles for Al, Ti, Cr and Mn from an $Al_{66}Ti_{25}Mn_9$/ $Al_{67}Ti_{25}Cr_8$ diffusion couple annealed 514h at 1273K.

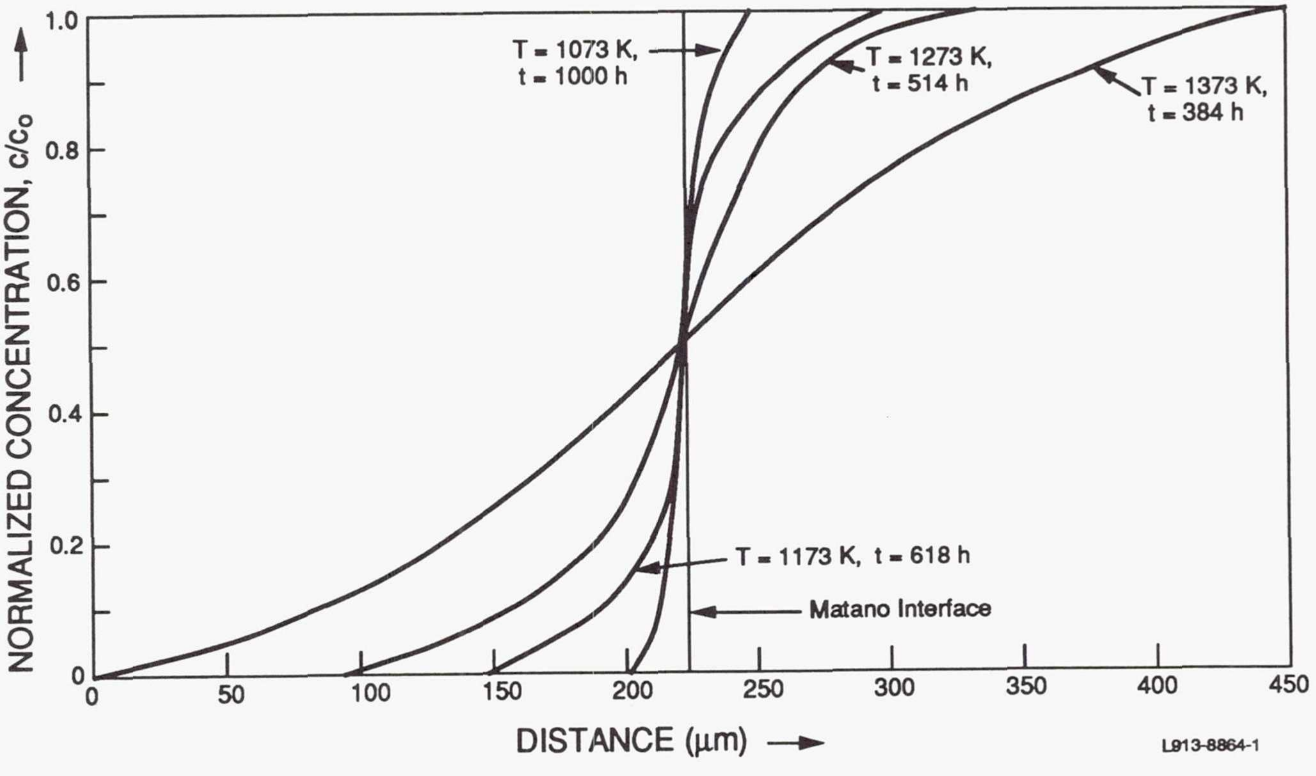

Figure 40. Normalized Mn concentration-distance profiles from $Al_{66}Ti_{25}Mn_9$/ $Al_{67}Ti_{25}Cr_8$ diffusion couples annealed between 1373K and 1073K.

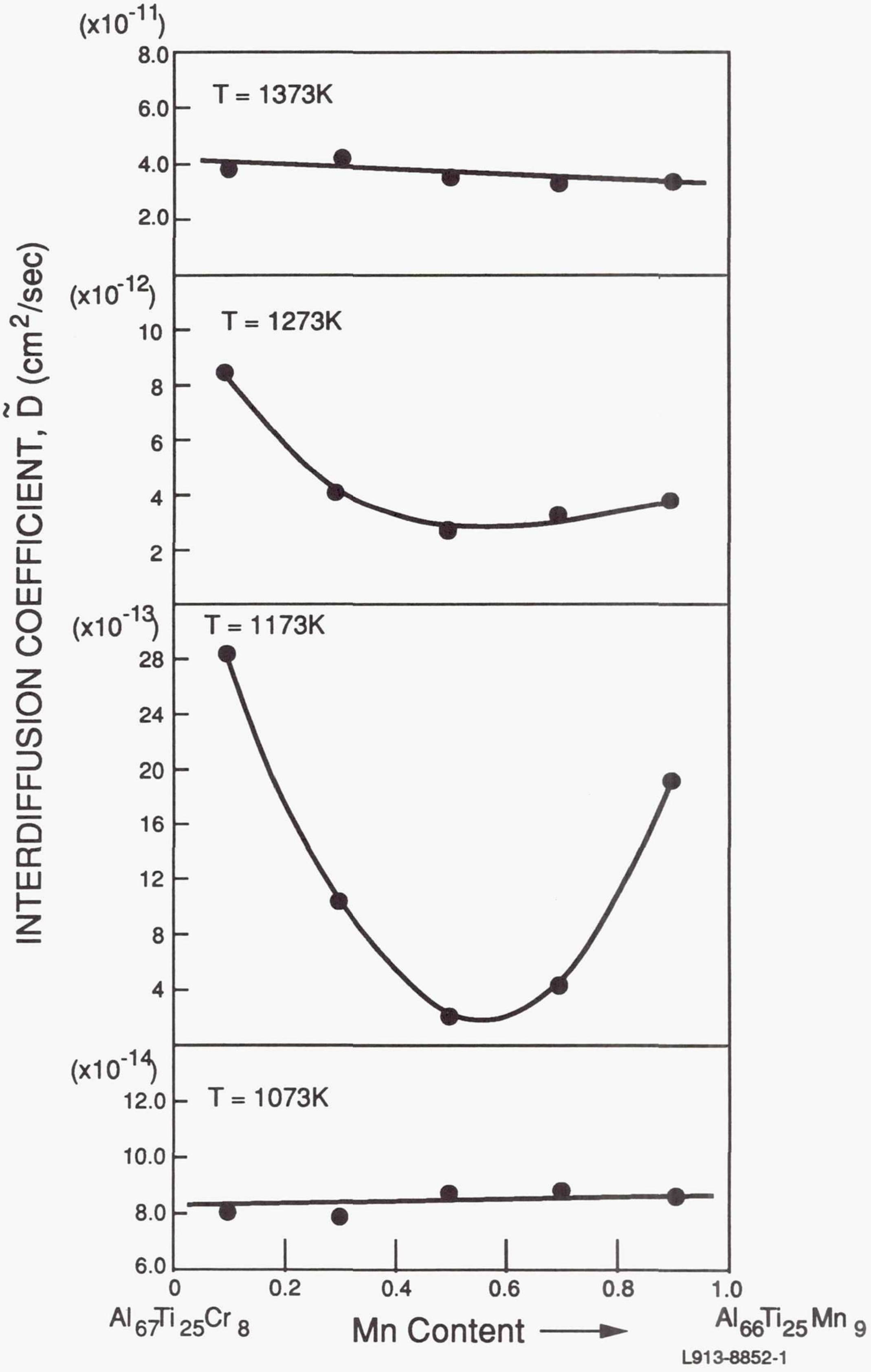

Figure 41. Variation in the interdiffusion coefficient, D, for the $Al_{66}Ti_{25}Mn_9$/ $Al_{67}Ti_{25}Cr_8$ system as a function of normalized Mn concentration for various temperatures.

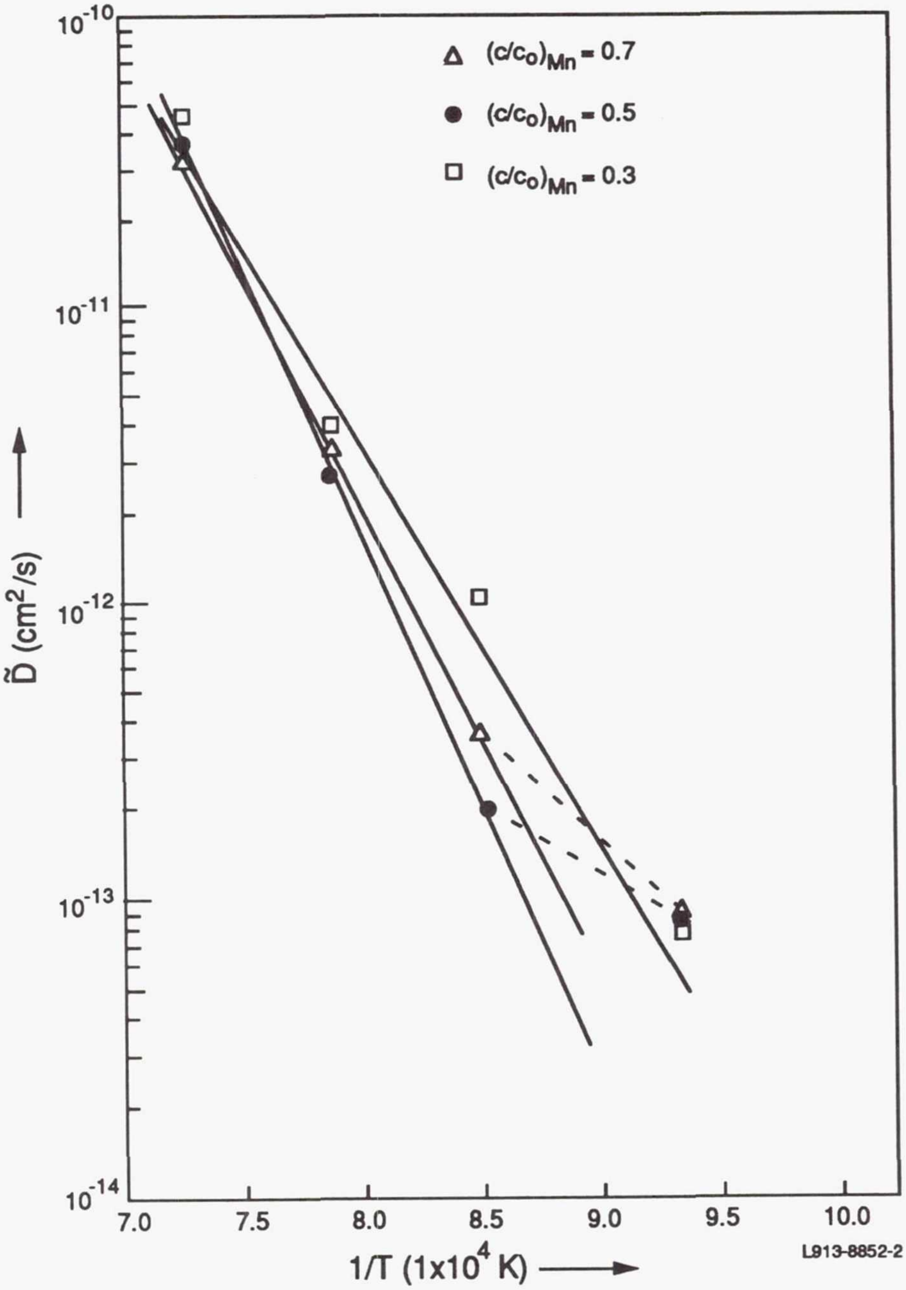

Figure 42. Variation in the interdiffusion coefficient for the $Al_{66}Ti_{25}Mn_9$/ $Al_{67}Ti_{25}Cr_8$ system as a function of temperature for various normalized Mn concentrations.

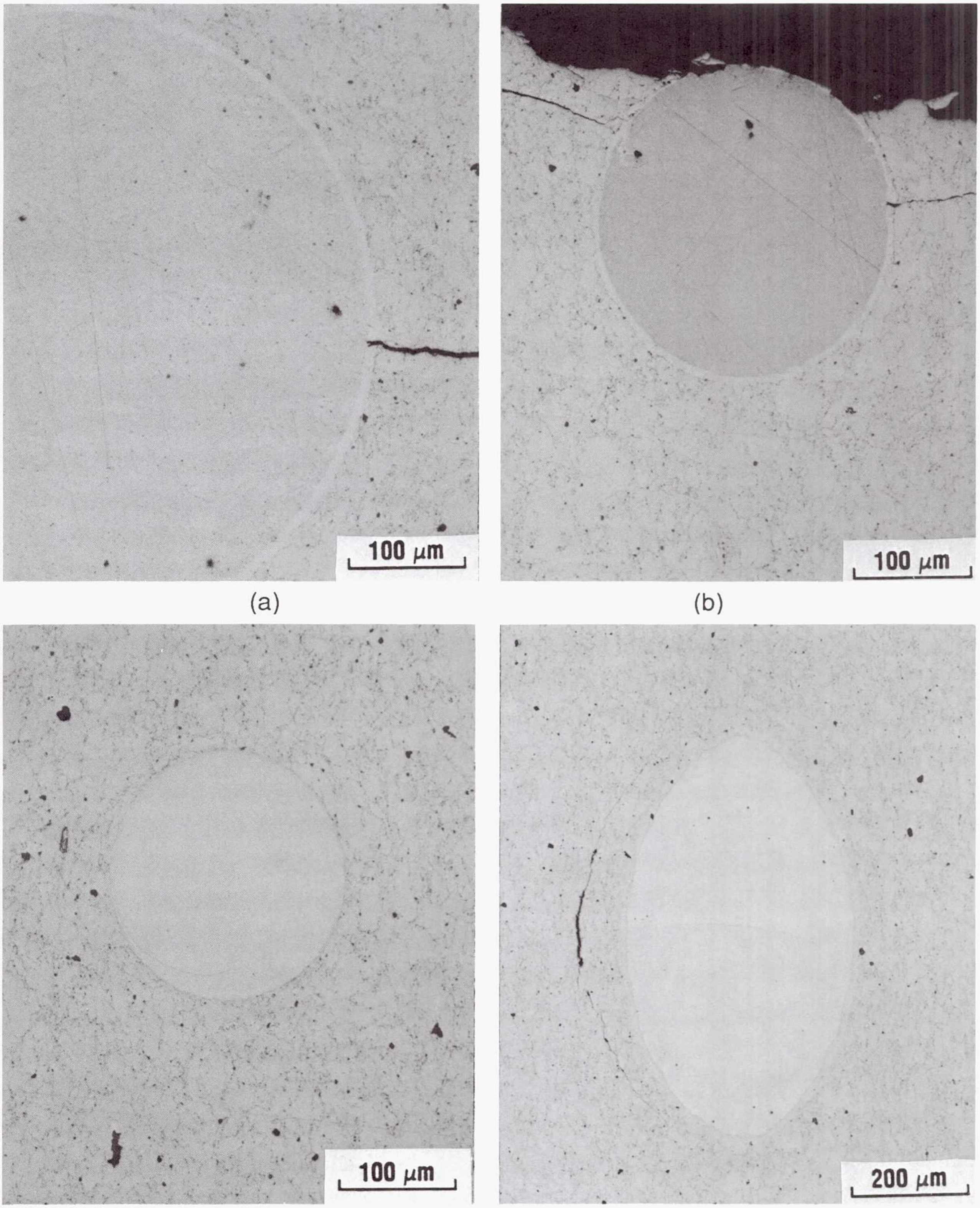

(a) (b) (c) (d)

Figure 43. Hot pressed $Al_{67}Ti_{25}Cr_8$ containing (a) Nb, (b) Ta, (c) W and (d) stainless steel wires revealing CTE mismatch and chemical compatibility effects.

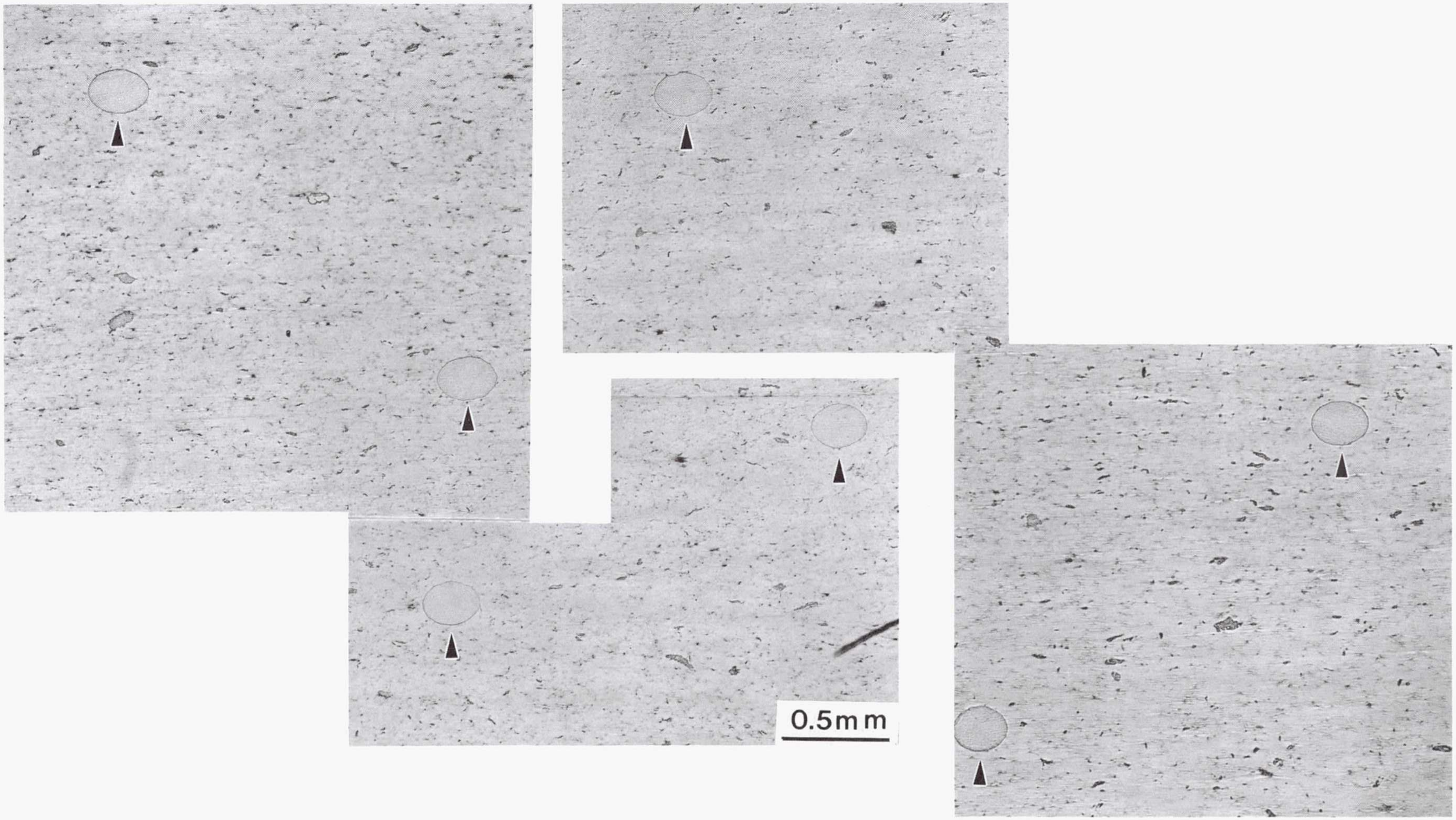

Figure 44. An assembly of W wires in $Al_{66}Ti_{25}Cr_9$ after hot pressing.

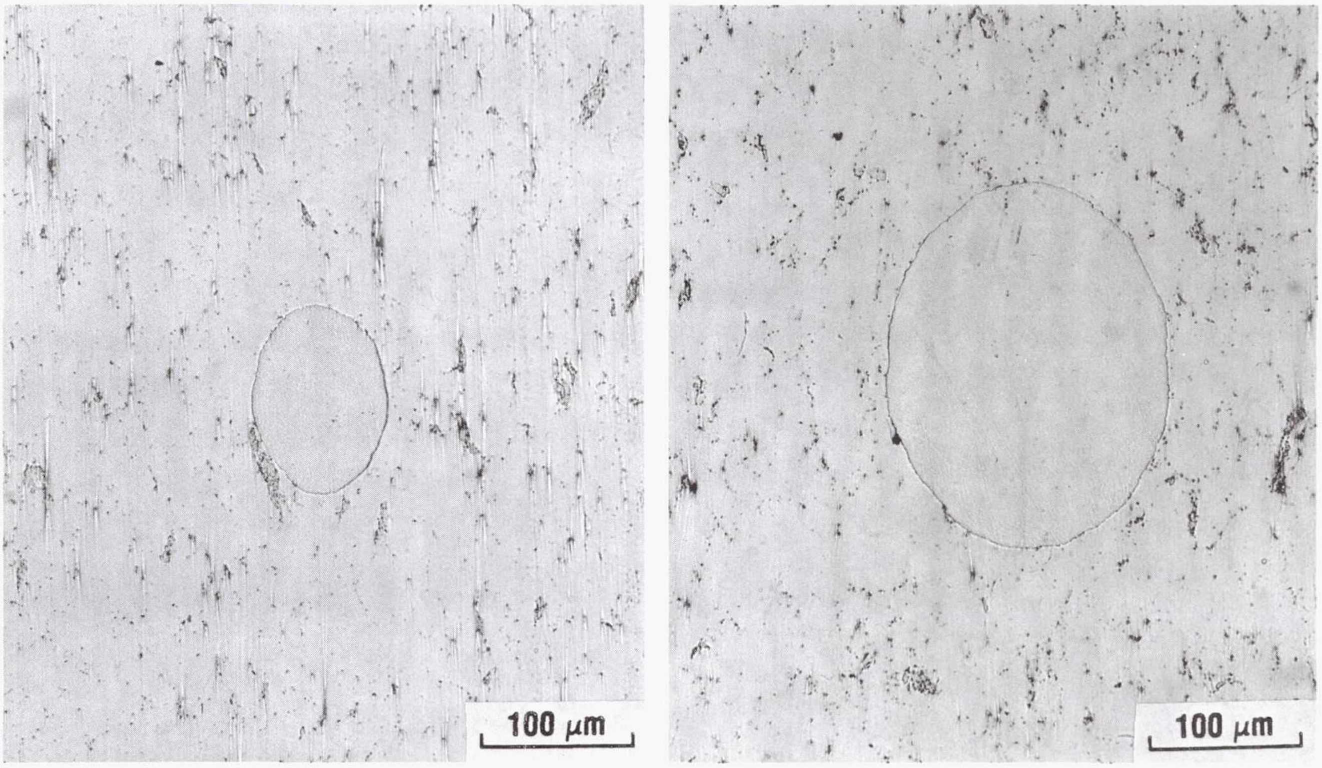

(a) (b)

Figure 45. Two different diameters of W fibers in $Al_{66}Ti_{25}Cr_9$ after hot pressing.

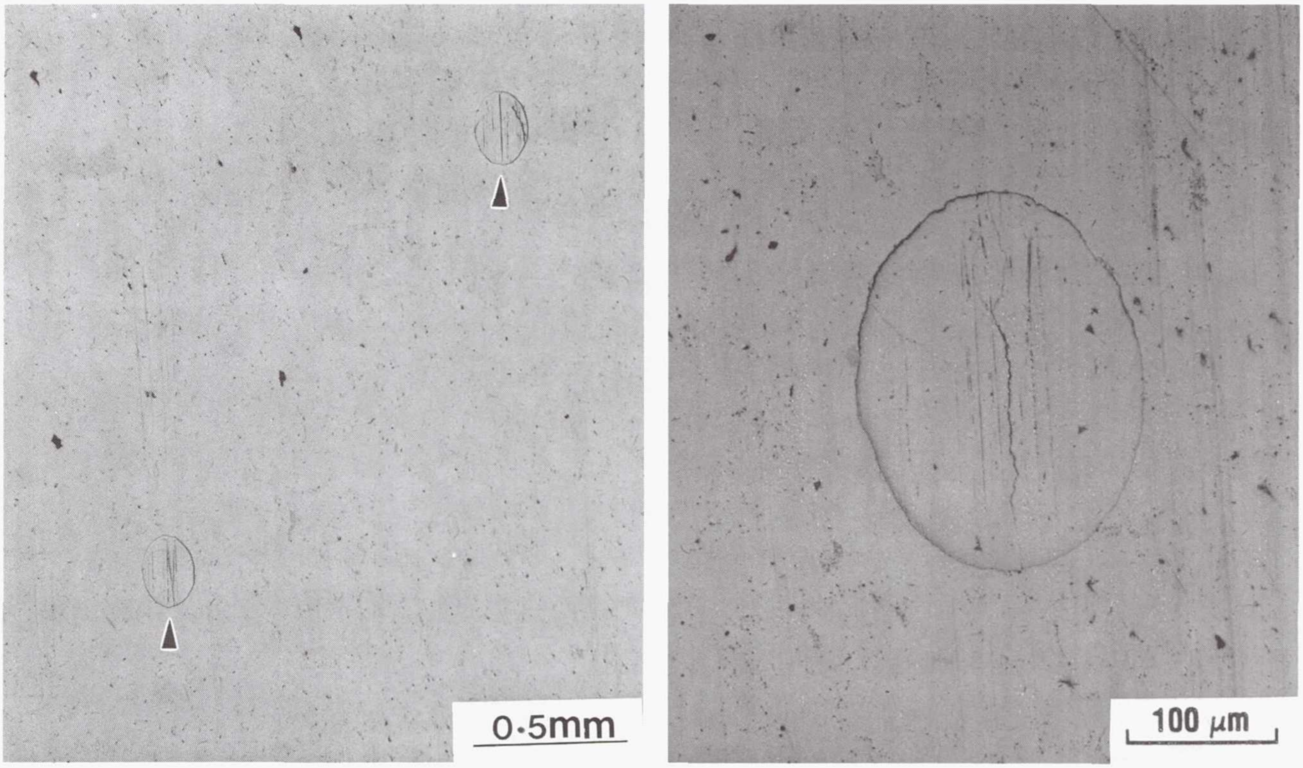

Figure 46. Tungsten fibers in hot pressed $Al_{66}Ti_{25}Cr_9$ after 10 cycles between 1023K and 300K.

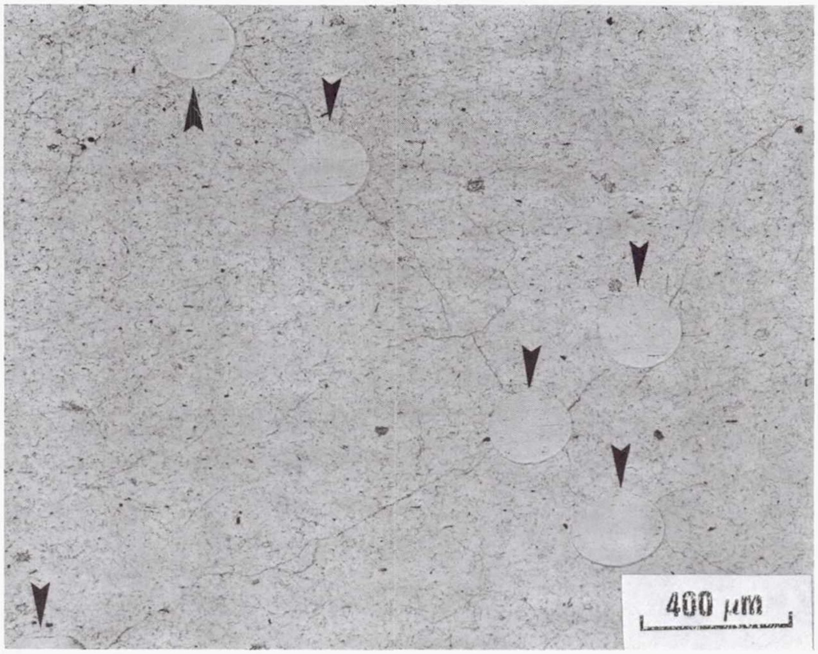

Figure 47. Fine cracks in the $Al_{66}Ti_{25}Cr_9$ matrix, connecting closely space W fibers (representative of ~7-8 vol.%) in the as-hot pressed condition.

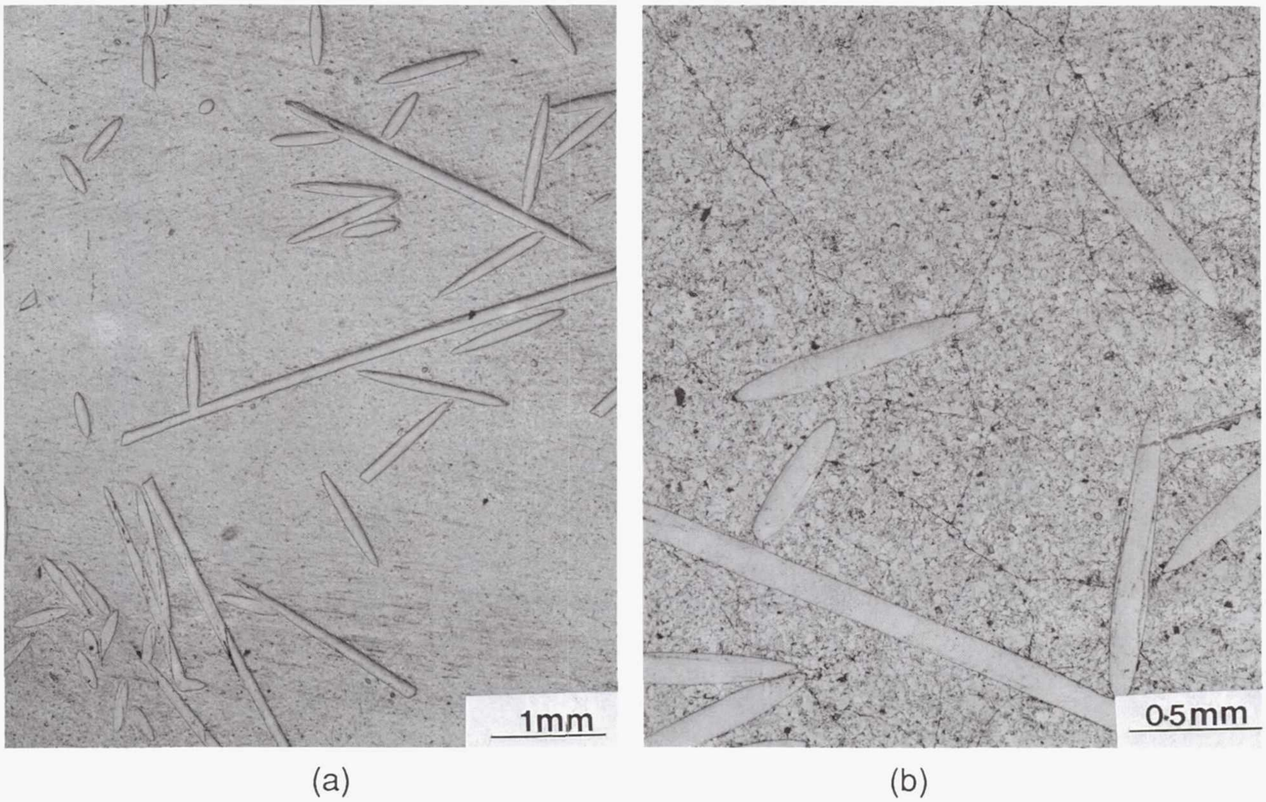

(a) (b)

Figure 48. Optical micrographs of the chopped fiber composite, $Al_{67}Ti_{25}Cr_8$ + 5 vol.% W, in the hot-pressed condition: (a) no obvious interfacial reactions and (b) significant cracking in the matrix from CTE mismatch.

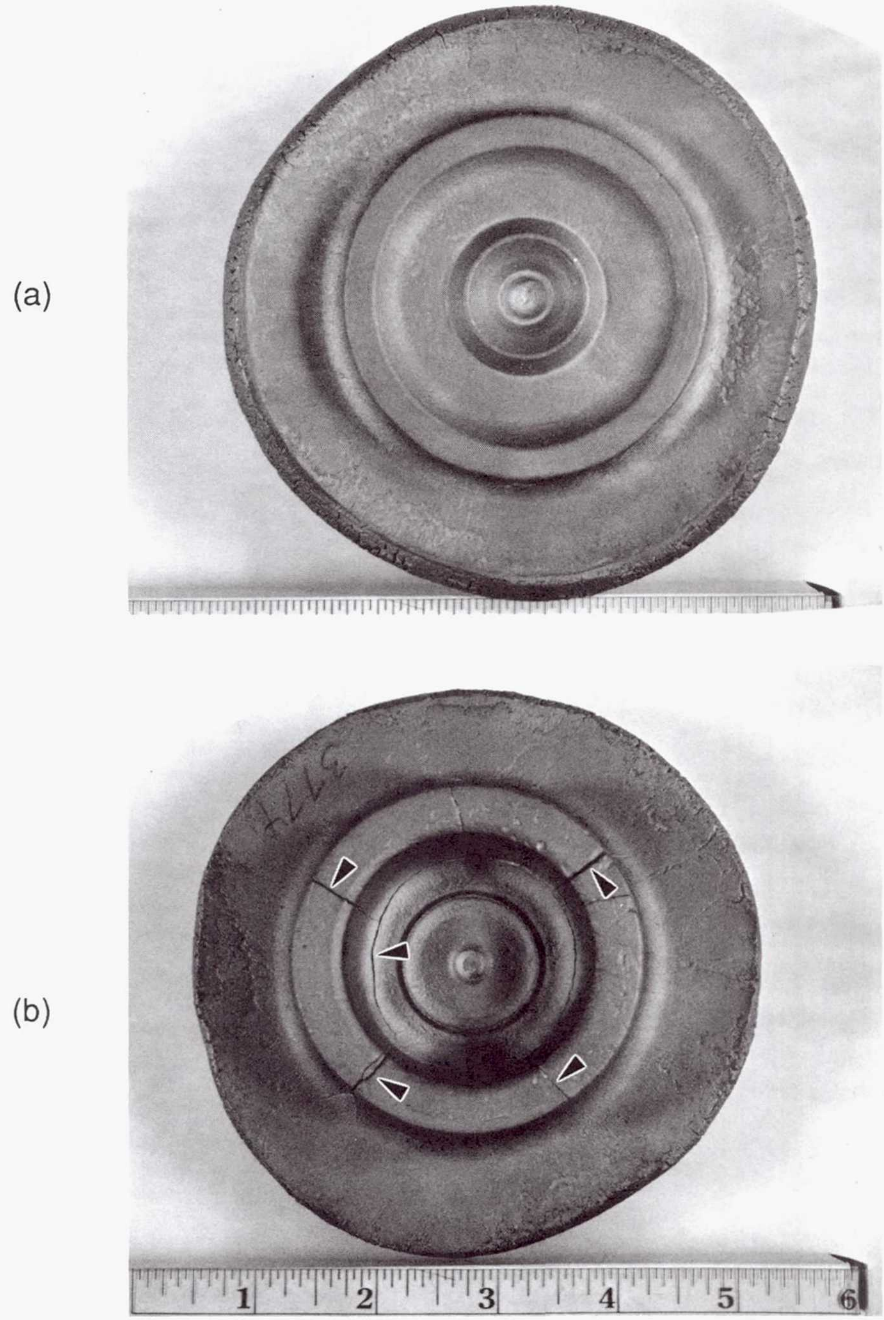

Figure 49. A shape forging of $Al_{66}Ti_{25}Mn_9$: (a) top, and (b) bottom view. (Arrows in (b) indicate cracking due to CTE mismatch between the Mo punch and the part during cooling, resulting from the inability to separate the part from the punch immediately after forging).

13. ABSTRACT (Continued)

program to enhance the low temperature damage tolerance of these materials (and possibly improve creep resistance simultaneously) was to incorporate long refractory metal wires (e.g. W, Nb, Ta, TZM, Ti, Fe and stainless steel) in the matrix. The matrix in this instance could be the monolithic material or its particulate-reinforced counterpart. Critical requirements include chemical compatibility and minimal thermal expansion coefficient (CTE) mismatch. Feasibility studies (single wire in a matrix) undertaken to identify a successful matrix-refractory wire combination indicated that only W wires survived after hot consolidation with no interfacial reactions and/or matrix cracking. Subsequent studies however indicated that upon increasing the number of wires to incorporate the influence of constraint stresses from adjacent wires, the matrix exhibited cracking as would be expected from the large CTE mismatch between W and these trialuminides. Up to 20 vol.% TiB_2 particles do not significantly reduce the CTE of the matrix. Thus, to date, a successful matrix-refractory metal wire combination has not been identified. In summary, it appears that of the various matrix compositions examined, ternary $Al_{66}Ti_{25}Mn_9$ exhibits the best balance in strength, ductility and oxidation resistance, The addition of TiB_2 particulates provides limited benefits, if any. They dramatically improve strength at low temperatures, although there is no clear benefit in strength at the projected use temperatures. The addition of these particulates causes a significant loss in ductility and may even cause a deterioration in oxidation resistance. The loss in ductility may arise due to a very fine grain size, boron in solid solution and the particles themselves acting as fracture initiation sites. The refinement in grain size is also likely responsible for the observed loss in high temperature strength. Although the idea of refractory metal wire reinforcement is an attractive one, a successful combination remains to be identified and possible approaches include the incorporation of a reaction barrier coating and compliant layers for accommodating CTE mismatch stresses.

REPORT DOCUMENTATION PAGE

Form Approved
OMB No. 0704-0188

1. AGENCY USE ONLY *(Leave blank)*	**2. REPORT DATE** April 1992	**3. REPORT TYPE AND DATES COVERED** Technical Memorandum

4. TITLE AND SUBTITLE

Composites of Low-Density Trialuminides: Particulate and Long Fiber Reinforcements

5. FUNDING NUMBERS

WU-510-01-50

6. AUTHOR(S)

K.S. Kumar, M.S. DiPietro, S.A. Brown, and J.D. Whittenberger

7. PERFORMING ORGANIZATION NAME(S) AND ADDRESS(ES)

National Aeronautics and Space Administration
Lewis Research Center
Cleveland, Ohio 44135-3191

8. PERFORMING ORGANIZATION REPORT NUMBER

E-6970

9. SPONSORING/MONITORING AGENCY NAMES(S) AND ADDRESS(ES)

National Aeronautics and Space Administration
Washington, D.C. 20546-0001

10. SPONSORING/MONITORING AGENCY REPORT NUMBER

NASA TM-105628

11. SUPPLEMENTARY NOTES

K.S. Kumar, M.S. DiPietro, and S.A. Brown, Martin Marietta Laboratories, Baltimore, Maryland 21227 (work funded under Contract NAS3-26069); J.D. Whittenberger, NASA Lewis Research Center. Responsible person, J.D. Whittenberger, (216) 433-3196.

12a. DISTRIBUTION/AVAILABILITY STATEMENT

Unclassified - Unlimited
Subject Category 24

12b. DISTRIBUTION CODE

13. ABSTRACT ***(Maximum 200 words)***

An examination of the ternary $L1_2$ trialuminides, $Al_{66}Ti_{25}Mn_9$, $Al_{67}Ti_{25}Cr_8$ and $Al_{22}Ti_8Fe_3$ in compression, bending and tension revealed that none of these compounds exhibited a desirable balance of strength, ductility and oxidation resistance. Thus, quaternary and quinary solid solutions of these ternary compounds may provide an optimal combination of these properties. Preliminary studies indicated that these three ternary compounds were mutually soluble in each other and further, a hardness minimum was observed in the as-cast quaternary alloy $Al_{66}Ti_{25}Mn_{6.75}Fe_{2.25}$. Diffusion couples were also examined in the system $Al_{66}Ti_{25}Mn_9$ - $Al_{67}Ti_{25}Cr_8$ in the temperature range 1073K - 1373K and these confirmed the presence of a continuous solid solution in this system. Interdiffusion coefficient, D and activation energy, Q were obtained for various intermediate compositions. Subsequently, specific quanternary and quinary compositions were cast, homogenized and isothermally forged. Particulate-reinforced (20 vol.% TiB_2) composites using these compositions as matrices were also produced via the XD™ process, pulverized to predetermined size distribution of powders, hot-pressed and isothermally forged to full density. Both, the monolithic material and its particulate-reinforced counterparts were examined in compression as a function of temperature and at high temperatures, as a function of strain rate. Three-point bend tests were conducted on the powder-metallurgy (P/M) processed composites to determine the ductile-to-brittle transition temperature. Likewise, bend tests were also conducted on the forged, ingot-metallurgy (I/M) processed monolithic material at 300K - 873K. *Some tensile tests were undertaken; however the results were generally disappointing, and frequently measurable ductility was* observed only above 773K. The microstructure of the as-forged material was characterized by optical and transmission electron microscopy techniques, and the bends and tensile fracture surfaces were examined in a scanning electron microscope (SEM). Heat-treatment studies were undertaken on the Al-Ti-Cr-Mn quaternary composition and an Al-Ti-Fe-Cr-Mn quinary composition to obtain an appreciation for grain-growth behavior. Such heat-treated materials were examined in compression as a function of temperature and, in three-point bending at 300K and 473K and compared against their as-forged counterparts. Likewise, bend tests were conducted at 473K on the ternary $Al_{66}Ti_{25}Cr_9$ that was heat-treated to obtain various grain sized to examine the role of grain size on plasticity and fracture stress. An alternate approach that was examined in this

14. SUBJECT TERMS

Intermetallic; Al-based; Mechanical properties

15. NUMBER OF PAGES	98
16. PRICE CODE	A05

17. SECURITY CLASSIFICATION OF REPORT	**18. SECURITY CLASSIFICATION OF THIS PAGE**	**19. SECURITY CLASSIFICATION OF ABSTRACT**	**20. LIMITATION OF ABSTRACT**
Unclassified	Unclassified	Unclassified	

NSN 7540-01-280-5500

Standard Form 298 (Rev. 2-89)
Prescribed by ANSI Std. Z39-18
298-102

National Aeronautics and
Space Administration

Lewis Research Center
Cleveland, Ohio 44135

Official Business
Penalty for Private Use $300